NATIONAL TECHNICAL UNIVERSITY OF ATHENS

SCHOOL OF CIVIL ENGINEERING

DEPARTMENT OF WATER RESOURCES & ENVIRONMENTAL ENGINEERING

REVERSE ANALYSIS AND UNCERTAINTY ASSESSMENT OF MAJOR FLOOD EVENTS UNDER LIMITED DATA AVAILABILITY: THE CASE OF WESTERN ATTICA, NOVEMBER 2017

Diploma Thesis

Charalampos Ntigkakis

Supervisor: Andreas Efstratiadis, Lab Teaching Staff, NTUA

Executive professor: Nikos Mamassis, Associate Professor, NTUA

Athens, November 2018

« Ἡ παιδεία, καθ' ἅπερ εὐδαίμων χώρα, πάντα τ’ ἀγαθά φέρει »

Σωκράτης

Ευχαριστίες (Acknowledgements in Greek)

Με την ολοκλήρωση αυτής της εργασίας, φτάνει στο τέλος του ένα τεράστιο κεφάλαιο της ζωής μου, ένα κεφάλαιο που ξεκίνησε πριν από 6 χρόνια με την είσοδό μου στη Σχολή Πολιτικών Μηχανικών ΕΜΠ. Μία περίοδος της ζωής μου η οποία συνοδεύτηκε από χαρές, λύπες, ενθουσιασμό, άγχος, πολλά ξενύχτια αλλά και απίστευτη διασκέδαση. Μία περίοδος της ζωής μου γεμάτη από εμπειρίες και αναμνήσεις, ο οποίες συνέβαλαν ώστε εκείνο το παιδί που ήρθε στην Αθήνα το 2012, να φτάσει σήμερα στο σημείο να γράφει αυτό το κείμενο. Και φυσικά, δεν θα μπορούσαν να λείπουν από αυτό οι άνθρωποι που στάθηκαν δίπλα μου στην πορεία αυτή, οι άνθρωποι που με πήραν από το χέρι και με βοήθησαν να γίνω ο άνθρωπος που έγινα.

Πρώτα και κύρια θα ήθελα να ευχαριστήσω τον Δρ. Πολιτικό Μηχανικό κ. Ανδρέα Ευστρατιάδη, ΕΔΙΠ ΕΜΠ. Πρόκειται για έναν από τους καλύτερους ανθρώπους που έχω συναντήσει στη ζωή μου, έναν δάσκαλο με τεράστιο ήθος και έναν εξαιρετικό επιστήμονα. Ομολογώ ότι είχα χάσει – ή μάλλον δεν είχα ακόμα αποκτήσει– το ενδιαφέρον μου για τη Σχολή, μέχρι τη στιγμή που παρακολούθησα εκείνη τη διάλεξή του στο μάθημα των Αστικών Υδραυλικών Έργων. Ήταν μία απλή, καθημερινή διάλεξη, το αντικείμενο της οποίας δε θυμάμαι καν. Κι όμως, ήταν μία διάλεξη που με βοήθησε να βρω το «κάλεσμά» μου στην επιστήμη του μηχανικού. Όταν δε τον γνώρισα καλύτερα μέσα στο μάθημα των Υδροηλεκτρικών Έργων, ήταν που τον «επέλεξα» ως τον άνθρωπό με τον οποίο θα ήθελα να συνεργαστώ στη διπλωματική μου εργασία. Και αυτό και έγινε. Ο «κύριος Ευστρατιάδης» είναι το μυαλό πίσω από αυτήν την εργασία, είναι αυτός που είχε την ιδέα και αυτός που βρήκε τα δεδομένα. Είναι αυτός που, με περισσή όρεξη και υπομονή, με καθοδήγησε καθ' όλη τη διάρκεια της εκπόνησής της διπλωματικής μου. Θα ήθελα λοιπόν να τον ευχαριστήσω θερμά, από τα βάθη της ψυχής μου, για όλη τη συμβολή του, για την εμπιστοσύνη που έδειξε στο πρόσωπό μου και κυρίως για την προθυμία του να ανεχτεί όλες τις ιδιοτροπίες μου.

Δεν θα μπορούσα να μην ευχαριστήσω τον καθηγητή της Σχολής, κ. Δημήτρη Κουτσογιάννη. Με την τεράστια εμπειρία του αποτέλεσε μία συνεχή πηγή γνώσης και με τον ιδιαίτερο τρόπο του μου έδωσε το κίνητρο να θέλω να αποκτήσω όση περισσότερη μπορούσα. Πρόκειται για έναν καθηγητή με απίστευτη όρεξη να βοηθήσει τον φοιτητή είτε απαντώντας του σε ερωτήσεις σχετικά με τις σπουδές, είτε ακόμα και δίνοντάς του συμβουλές ζωής. Και πάνω απ' όλα, με διάθεση να αφήσει κάτι καλύτερο πίσω του για την επόμενη γενιά μηχανικών. Νιώθω από τους πιο τυχερούς που υπήρξα φοιτητής της Σχολής κατά την περίοδο που διετέλεσε κοσμήτορας.

Επόμενος στη λίστα είναι ο κ. Μαμάσης Νίκος, αναπληρωτής καθηγητής της Σχολής και υπεύθυνος καθηγητής σε αυτήν την εργασία. Μας δίδαξε την εμπειρική σκοπιά της επιστήμης, το πώς μπορεί ένας μηχανικός να αξιοποιήσει την εμπειρία που έχει μαζέψει στον πεδίο.

Φυσικά, δεν θα μπορούσε να λείπει από αυτό το κείμενο ο Παναγιώτης Δημητριάδης, Δρ. Πολιτικός Μηχανικός. Αποτελεί φωτεινό παράδειγμα νέου επιστήμονα, με όρεξη και μεράκι για αυτό που κάνει και πηγή έμπνευσης για τους φοιτητές. Είχα την τύχη να τον γνωρίσω τον

τελευταίο χρόνο των σπουδών μου και τον ευχαριστώ ιδιαίτερα για την πολύτιμη βοήθεια που μου προσέφερε, εντός και εκτός του αντικειμένου του Πολιτικού Μηχανικού.

Θα ήθελα ακόμα να ευχαριστήσω και τον υποψήφιο διδάκτορα, Διονύση Νικολόπουλο. Μπορεί η συνεργασία μας να μην είχε ιδιαίτερη έκταση, αλλά η βοήθεια που μου προσέφερε στη Matlab και το GIS σίγουρα ήταν πολύτιμη.

Σε πιο προσωπικό επίπεδο, θα ήθελα να ευχαριστήσω τον άνθρωπο που με τον χαρακτήρα του έκανε τη φοιτητική μου ζωή τόσο ξεχωριστή. Πρόκειται για τον φίλο και αδερφό, Γιώργο Πουλιάση. Ποιος θα το πίστευε ότι εκείνο το λαχανιασμένο παιδί που μπήκε καθυστερημένο στο αμφιθέατρο την πρώτη μέρα μαθημάτων και έκατσε δίπλα μου, θα ήταν ο άνθρωπος με τον οποίο θα ταίριαζα περισσότερο. Ίσως να φταίει το ότι κανένας από τους δυο μας δεν έχει χιούμορ, δεν ξέρω. Σίγουρα όμως ξέρω ότι, μετά από την κοινή μας πορεία όλα αυτά τα χρόνια, η φιλία που δημιουργήσαμε είναι από τις πιο δυνατές.

Σίγουρα αξίζει ιδιαίτερη αναφορά στην πολύ καλή μου φίλη, Μαρία Νέζη. Με την Μαρία απλά έτυχε να αλλάξουμε κατεύθυνση στη Σχολή την ίδια περίοδο, οπότε όντας και οι δύο «μεγαλύτεροι» ξεκινήσαμε να κάνουμε παρέα. Περνούσε το ίδιο ακριβώς ζόρι που περνούσα κι εγώ, την ίδια ακριβώς περίοδο που το περνούσα κι εγώ, οπότε υπήρξε αποδέκτης γκρίνιας, νεύρων και ακόμα περισσότερης γκρίνιας, αλλά και πηγή ατελείωτης στήριξης τα τελευταία δύο χρόνια.

Και φυσικά, την παρέα συμπληρώνουν η Γεωργία Νικολακάκου, ο Γιώργος Πολλάκης και ο Γιάννης Τιπτιρής. Πρόκειται για μία ομάδα ανθρώπων με εντελώς διαφορετικούς χαρακτήρες, που σου χαρίζουν αμέτρητες ώρες γέλιου με τα «κατορθώματά» τους. Είναι ο ορισμός της λέξης «φίλος» και νιώθω απίστευτα τυχερός που οι δρόμοι μας διασταυρώθηκαν.

Κλείνοντας τον κύκλο των φίλων, θα ήθελα να αναφερθώ στον Γιώργο Χαϊνάκη, τον Γιάννη Σπανό και τον Δημήτρη Βαρδάκη. Είναι η παρέα του Ηρακλείου, ένα παράδειγμα πραγματικής φιλίας.

Και τώρα ήρθε η σειρά για τα αδέρφια μου, Δημήτρη και Κατερίνα. Μπορεί στην αρχή να με είδαν σαν παιχνίδι, αλλά πίσω από τις στολές και τα καπέλα που μου φορούσαν όταν ήμουν μωρό, κρύβεται ο ορισμός της αδερφικής αγάπης. Ήταν και είναι πάντα εκεί για να μη μου λείψει τίποτα, για να με διδάξουν με τις εμπειρίες τους. Και ο «Χάρης» ξέρει πως κάθε φορά που βρίσκει τα σκούρα, τα αδέρφια του θα είναι εκεί να του δείξουν το δρόμο.

Βέβαια, αξίζει να σημειωθεί ότι πλέον δεν είμαι «ο μικρός», ο τίτλος αυτός ανήκει στον Μιχάλη. Γιατί όταν είσαι γιος της Κατερίνας, παίρνεις όλα τα ωραία! Ο «Μιχαλάκης» μπορεί να μην ξέρει ακόμα να διαβάζει, αλλά είναι ο λόγος που το Ηράκλειο μου λείπει τόσο πολύ.

Τέλος, το μεγαλύτερο «ευχαριστώ» πάει στους γονείς μου, Γεωργία και Νίκο. Αυτοί είναι οι πραγματικοί ήρωες αυτής της ιστορίας, αυτοί είναι οι άνθρωποι που έθεσαν τα θεμέλια ώστε να γίνω ο άνθρωπος που είμαι σήμερα. Εδώ και 24 χρόνια αποτελούν τους άγρυπνους φρουρούς πάνω από τον ώμο μου, που με τις ατελείωτες θυσίες τους εγώ έφτασα ως εδώ. Ήταν δίπλα μου

καθ' όλη την πορεία και με αυταπάρνηση μου προσέφεραν τις καλύτερες δυνατές συνθήκες για να ακολουθήσω τον δρόμο που επέλεξα και να κυνηγήσω τα όνειρά μου. Μαμά, Μπαμπά, ευτυχώς που σας έχω!

Χαράλαμπος Ντιγκάκης
Αθήνα, 2018

Abstract

From November 14th until November 15th, 2017, a storm event of substantial, yet unknown, local intensity, has caused a flash flood in Western Attica, Greece. The flood was responsible for significant economic losses, mainly focused in the city of Mandra, as well as for 24 fatalities. Right after the incident, a debate arose about whether the devastating results were due to the extreme nature of the storm, or due to the poor flood protection works. In this research, we analyzed all available information sources in an attempt to reproduce the actual storm event and provide estimations about its magnitude, temporal evolution and return period.

The primary data source was the observed point rainfall at three meteorological stations in the wider area around the city of Mandra. However, one could easily conclude that these local rainfall events were not significant enough to cause such a severe flooding. This realization was further supported by the indicative rainfall estimations provided by an X-band meteorological radar, which recorded an unusual storm pattern of very high intensity over a very limited area, that strongly affected a relatively small spatial extent upstream of Mandra. Nevertheless, neither the point observations not the highly uncertain radar data were sufficient for providing quantitative estimations about the extreme rainfall event.

The most valuable information was found in the neighboring catchment of Sarantapotamos, which is equipped with automatic stage recorder that controls a drainage area of 144.6 km^2 (hydrometric station at Gyra Stefanis). The available data sources were: (a) point rainfall data at a remote (upstream) meteorological station (Vilia); (b) 15-min stage data that allowed reproducing part of the rising limb of the flood hydrograph at Gyra Stefanis, just before the flood destroyed the instruments assembly; and (c) audiovisual material at the station area, providing valuable information about the temporal evolution of the flood.

The aforementioned information, quantitative and qualitative, was used in an attempt to estimate the rainfall over the basin of Sarantapotamos through a reverse rainfall-runoff modelling approach. In this respect, we tested several parsimonious versions of lumped event-based schemes, and calibrated their input against the observed flows at Gyra Stefanis. As input we considered the areal rainfall over Sarantapotamos, embedding the observed hyetograph at Vilia and an unknown hyetograph at a hypothetical station. The proposed modeling schemes used the SCS-CN method to estimate the effective rainfall and two alternative approaches, i.e. a lag-and-route method and a parametric synthetic unit hydrograph to propagate the runoff to the basin outlet. All model versions contained one free parameter, i.e. the initial abstraction ratio, and an unknown initial condition, expressed in terms of a dimensionless coefficient describing the antecedent moisture conditions of the SCS-CN method in continuous mode.

Initially, we made scenario-based investigations, which revealed the major uncertainty induced by the lack of information and the sensitivity of results against the arbitrary assignment of hypothetical values to the two model parameters. In order to better assess this uncertainty, we

next employed Monte Carlo simulations by generating 1000 random sets of the model parameters from suitable distributions and next solving the calibration problem. Within the selection of distributions, for parameter sampling, as well as within calibrations, we took advantage of all available information about the hydrological regime of the basin, the soil conditions the days before the event, and the temporal evolution of the flood after the destruction of the stage recorder.

Based on the outcomes of Monte Carlo simulations, we provided probabilistic estimations of the quantities of interest, i.e. the total rainfall over the study area, its temporal evolution, and the peak flow of Sarantapotamos at Gyra Stefanis. We also employed risk evaluations, by estimating the maximum intensities and associated return periods of the storm event across several time scales. These results were then compared to additional sources of information, in an attempt to justify the plausibility of the aforementioned analysis.

Εκτενής περίληψη (Extended abstract in Greek)

Την 14η και 15η Νοεμβρίου 2017, μία βροχόπτωση με σημαντική ένταση εκδηλώθηκε στη Δυτική Αττική, με αποτέλεσμα την εμφάνιση αιφνίδιας πλημμύρας στην περιοχή, τις πρωινές ώρες της 15ης Νοεμβρίου. Ο απολογισμός της πλημμύρας ήταν σημαντικές υλικές ζημιές, κυρίως στους αστικούς ιστούς της Μάνδρας, της Νέας Περάμου, της Μαγούλας και της Ελευσίνας. Πέραν αυτών, το πλημμυρικό αυτό συμβάν προκάλεσε το θάνατο 24 ανθρώπων, με αποτέλεσμα να χαρακτηριστεί ως η τρίτη φονικότερη πλημμύρα στην Δυτική Αττική. Αμέσως μετά την πλημμύρα, ξεκίνησε μία αντιπαράθεση ως προς το κατά πόσο τα καταστροφικά αποτελέσματα οφείλονταν στην ακραία φύση της καταιγίδας ή στην ελλιπή αντιπλημμυρική προστασία. Στην παρούσα εργασία, αναλύθηκαν όλες οι διαθέσιμες πληροφορίες από διάφορες πηγές, σε μια προσπάθεια να αναπαραχθεί το επεισόδιο της καταιγίδας και να εκτιμηθούν το μέγεθός του, η χρονική του εξέλιξη, καθώς και η περίοδος επαναφοράς του.

Οι βροχοπτώσεις ξεκίνησαν τις βραδινές ώρες της 14ης Νοεμβρίου και είχαν ως αποτέλεσμα την ταχύτατη μείωση της διηθητικής ικανότητας του εδάφους, την έναρξη της εδαφικής διάβρωσης και κατ' επέκταση τη συσσώρευση φερτών υλών στα υδάτινα σώματα. Μία απότομη αλλαγή στην ένταση της βροχόπτωσης τις πρωινές ώρες της 15ης Νοεμβρίου συνέβαλλε στην σημαντική αύξηση της εδαφικής διάβρωσης, οδηγώντας έτσι στην σημαντική ένταση του φαινομένου της στερεοαπορροής. Άμεση απόρροια των παραπάνω, ήταν η εμφάνιση του πλημμυρικού κύματος στην πόλη της Μάνδρας περίπου στις 7:00 π.μ. την 15η Νοεμβρίου, την υπερχείλιση των έργων διόδευσης στο ύψος του αυτοκινητοδρόμου Ε94 (Αττική Οδός) και τη διόδευση που πλημμυρικού όγκου μέσω του δρόμου Μάνδρας-Ελευσίνας.

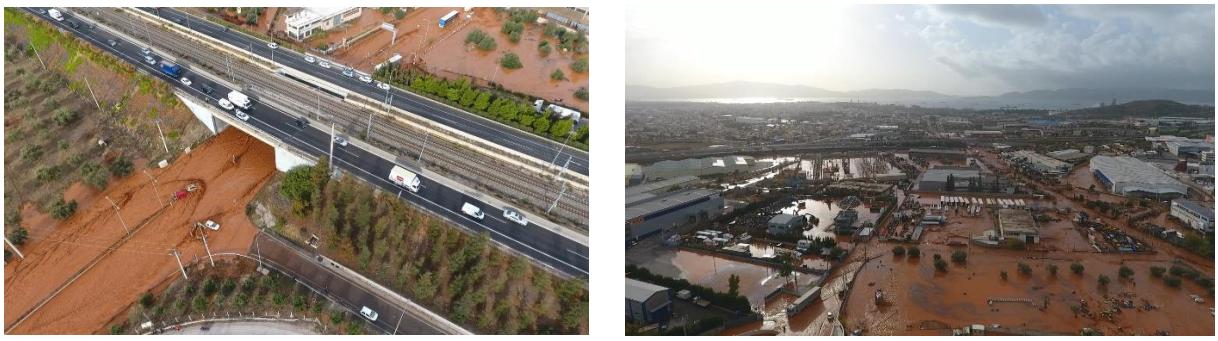

Εικόνα 1. Οδός Μάνδρας-Ελευσίνας (αριστερά) και ΒΙ.ΠΕ. Μάνδρας (δεξιά) την 15/11/2017

Η κύρια πηγή πληροφοριών ήταν οι σημειακές μετρήσεις βροχόπτωσης στους μετεωρολογικούς σταθμούς των Βιλίων, της Μάνδρας και της Ελευσίνας. Το πρώτο συμπέρασμα που εξήχθη από τις καταγραφές αυτές, ήταν πως το παρατηρημένο ύψος βροχόπτωσης δεν μπορούσε να δικαιολογήσει την έκταση της πλημμύρας. Η παρατήρηση αυτή ενισχύθηκε περισσότερο από τις ενδεικτικές εκτιμήσεις βροχόπτωσης ενός μετεωρολογικού ραντάρ, οι οποίες δείχνουν ένα ασυνήθιστο σχήμα καταιγίδας, με πολύ ισχυρό και τοπικό πυρήνα, το οποίο πέρασε ανάμενα από την περιοχή που καλύπτεται από τους σταθμούς. Παρ' όλα αυτά, ούτε οι σημειακές

μετρήσεις, ούτε οι εξαιρετικά αβέβαιες πληροφορίες του ραντάρ μπόρεσαν να παρέχουν επαρκείς εκτιμήσεις για το επεισόδιο βροχόπτωσης.

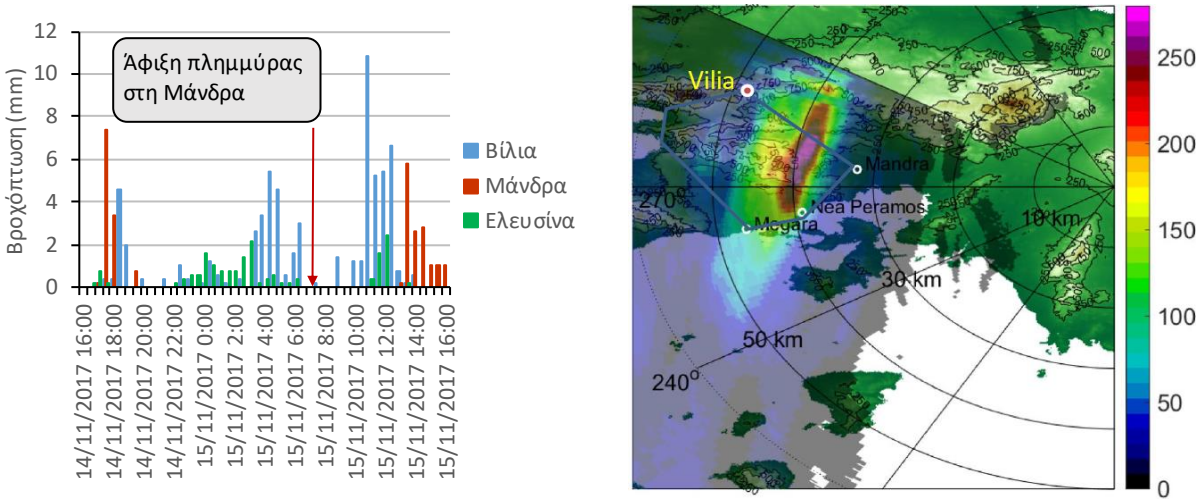

Σχήμα 1. Παρατηρήσεις βροχόπτωσης (αριστερά) και εκτιμήσεις μετεωρολογικού ραντάρ (δεξιά)

Η λύση στο πρόβλημα αυτό προήλθε από την γειτονική λεκάνη απορροής του Σαρανταπόταμου, καθώς στη λεκάνη αυτή λειτουργεί ένας αυτόματος μετρητής στάθμης του υδατορέματος. Ο μετρητής αυτός βρίσκεται στη θέση Γύρα Στεφάνης και η έκταση της λεκάνης ανάντη του μετρητή ανέρχεται στα 144.6 km^2. Οι μετρήσεις που μας παρείχε ήταν σε δεκαπεντάλεπτο βήμα και κάλυπταν μέρος του ανοδικού κλάδου του υδρογραφήματος στη Γύρα Στεφάνης, αμέσως πριν το όργανο καταστραφεί από το πλημμυρικό κύμα. Εντός της λεκάνης βρίσκεται ακόμα ο μετεωρολογικός σταθμός των Βιλίων, ο οποίος παρείχε σημειακές καταγραφές βροχόπτωσης. Σημαντικό ρόλο στην ανάλυση έπαιξε και η εμπειρία που συλλέχτηκε για την υδρολογική συμπεριφορά της λεκάνης, κατά τη διετία 2012-2014, όταν στα πλαίσια του ερευνητικού προγράμματος «Δευκαλίων» πραγματοποιήθηκαν μελέτες στην περιοχή. Τέλος, αξιοποιήθηκε και το οπτικοακουστικό υλικό που συλλέχτηκε από την περιοχή του σταθμού κατά τη διάρκεια της πλημμύρας.

Οι παραπάνω πληροφορίες, ποιοτικές και ποσοτικές, χρησιμοποιήθηκαν σε μία προσπάθεια να εκτιμηθεί η βροχόπτωση στη λεκάνη του Σαρανταπόταμου μέσω μιας διαδικασίας αντίστροφης ανάλυσης βροχής-απορροής. Για τον λόγο αυτό, αναπτύχθηκαν διάφορες εκδοχές μοντέλων ανάλυσης του γεγονότος, οι είσοδοι των οποίων βαθμονομήθηκαν σύμφωνα με τις παρατηρημένες παροχές στη θέση Γύρα Στεφάνης. Ως είσοδος, εισάγεται η επιφανειακή βροχόπτωση στη λεκάνη, συμπεριλαμβάνοντας τις καταγραφές βροχής στα Βίλια και ένα άγνωστο υετογράφημα σε έναν υποθετικό σταθμό. Τα προτεινόμενα μοντέλα χρησιμοποιούν τη μέθοδο SCS-CN για την εκτίμηση της ενεργού βροχόπτωσης καθώς και δύο διαφορετικές προσεγγίσεις για την διόδευση της πλημμύρας. Αυτές είναι η θεώρηση πως η λεκάνη συμπεριφέρεται ως γραμμικός ταμιευτήρας, καθώς και η διόδευση με τη χρήση του παραμετρικού συνθετικού μοναδιαίου υδρογραφήματος. Όλα τα μοντέλα περιέχουν μία ελεύθερη παράμετρο, δηλαδή το ποσοστό αρχικών απωλειών, καθώς και μία άγνωστη αρχική

συνθήκη, εκφρασμένη μέσω ενός αδιάστατου συντελεστή που εκφράζει τις συνθήκες υγρασίας της μεθόδου SCS-CN με συνεχή αντί για διακριτή κατηγοριοποίηση.

Αρχικά, εξετάστηκαν διάφορα υδρολογικά σενάρια, επιλέγοντας αυθαίρετες αρχικές παραμέτρους, τα οποία αποκάλυψαν την τεράστια αβεβαιότητα που οφείλεται στα ελλιπή δεδομένα, καθώς και την ευαισθησία των αποτελεσμάτων στην αυθαίρετη ανάθεση των αρχικών τιμών. Στη συνέχεια, με χρήση της μεθόδου των όμβριων καμπυλών επιχειρείται μία εκτίμηση του ρίσκου, μέσω της εκτίμησης των μέγιστων εντάσεων βροχόπτωσης και των αντίστοιχων περιόδων επαναφοράς, για διάφορες χρονικές κλίμακες. Η εκτίμηση όμως του ρίσκου ακολουθεί την ίδια αβέβαιη συμπεριφορά.

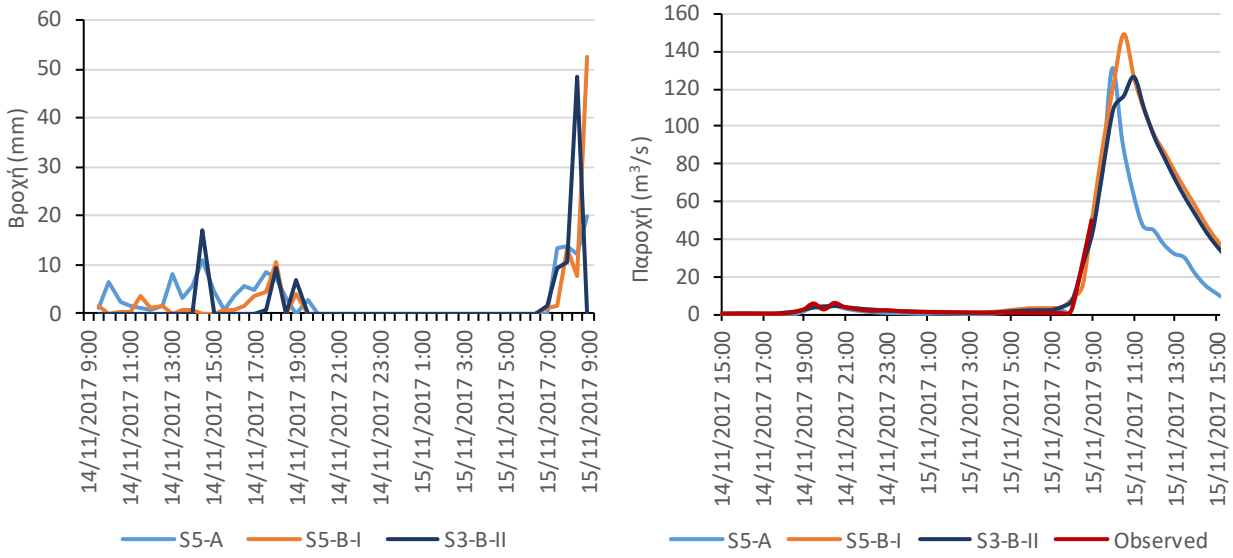

Σχήμα 2. Εκτιμήσεις παροχής (αριστερά) και βροχόπτωσης (δεξιά) από υδρολογικά σενάρια

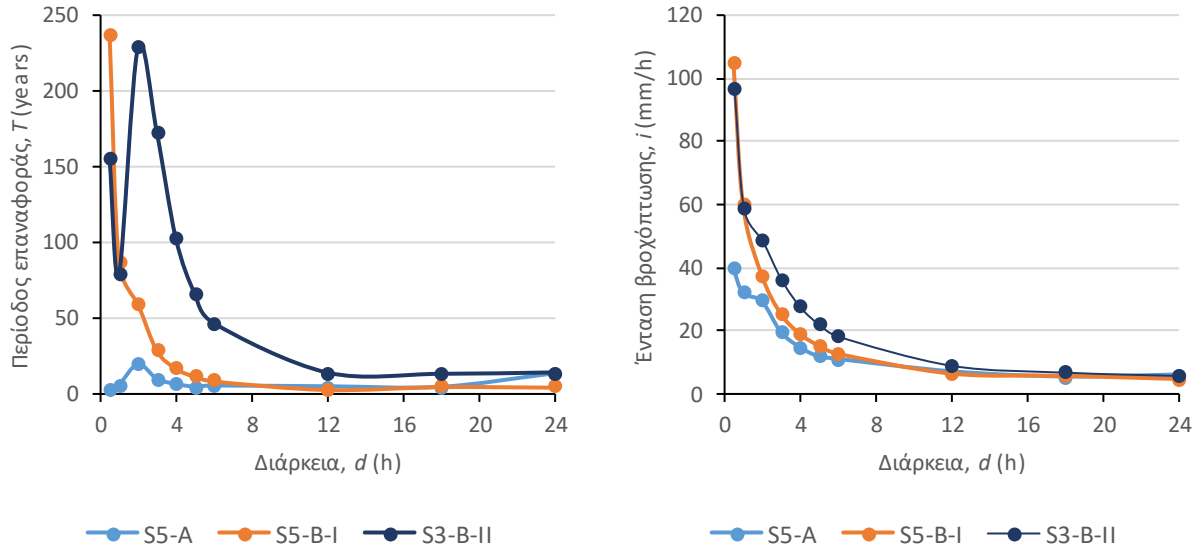

Σχήμα 3. Εκτιμήσεις περιόδου επαναφοράς (αριστερά) και μέγιστης έντασης βροχόπτωσης (δεξιά) σε διάφορες χρονικές κλίμακες από υδρολογικά σενάρια

Προκειμένου να εκτιμηθεί καλύτερα η αβεβαιότητα αυτή, εφαρμόζεται η στοχαστική προσέγγιση των αναλύσεων Monte Carlo. Πραγματοποιούνται διαφορετικές αναλύσεις, κάθε μία εκ των οποίων περιέχει διαφορετική πληροφορία, σε μία προσπάθεια να ποσοτικοποιηθεί η αβεβαιότητα και να ληφθεί υπόψη η αναμενόμενη στατιστική συμπεριφορά των μοντέλων. Οι αναλύσεις αυτές έγιναν για 1000 ζεύγη τιμών των αρχικών παραμέτρων, πραγματοποιώντας τη δειγματοληψία από κατάλληλες κατανομές και λύνοντας το πρόβλημα της βαθμονόμησης. Για την επιλογή των κατάλληλων κατανομών αυτών, καθώς επίσης και για τη βαθμονόμηση, χρησιμοποιήθηκαν όλες οι διαθέσιμες πληροφορίες για το υδρολογικό καθεστώς της λεκάνης, τις συνθήκες του εδάφους τις προηγούμενες μέρες, καθώς και την χρονική εξέλιξη της πλημμύρας μετά την καταστροφή του οργάνου.

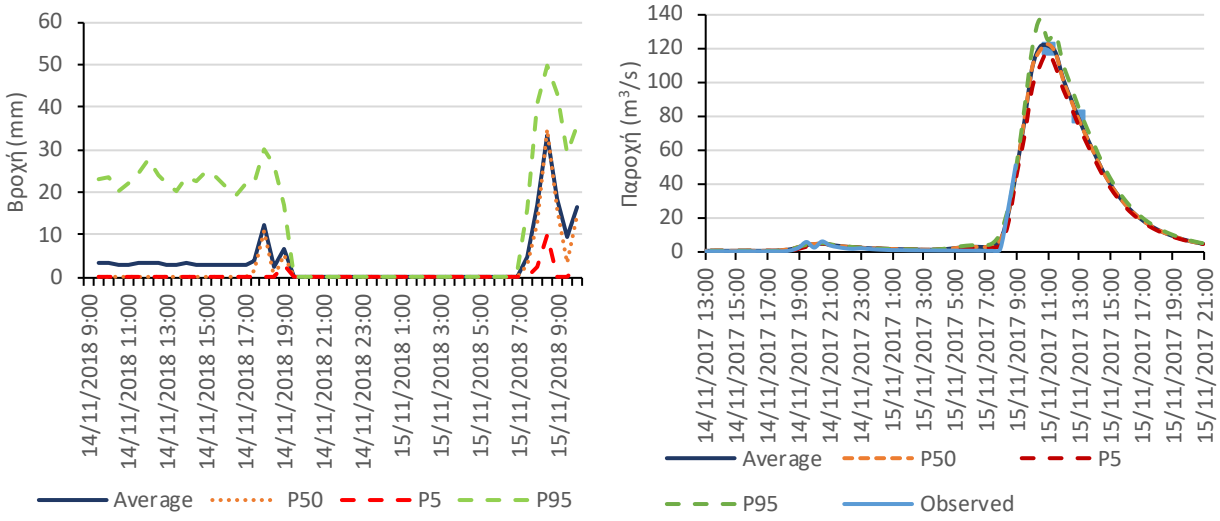

Σχήμα 4. Εκτιμήσεις βροχόπτωσης (αριστερά) και παροχής (δεξιά) με τα αντίστοιχα διαστήματα εμπιστοσύνης για ανάλυση Monte Carlo

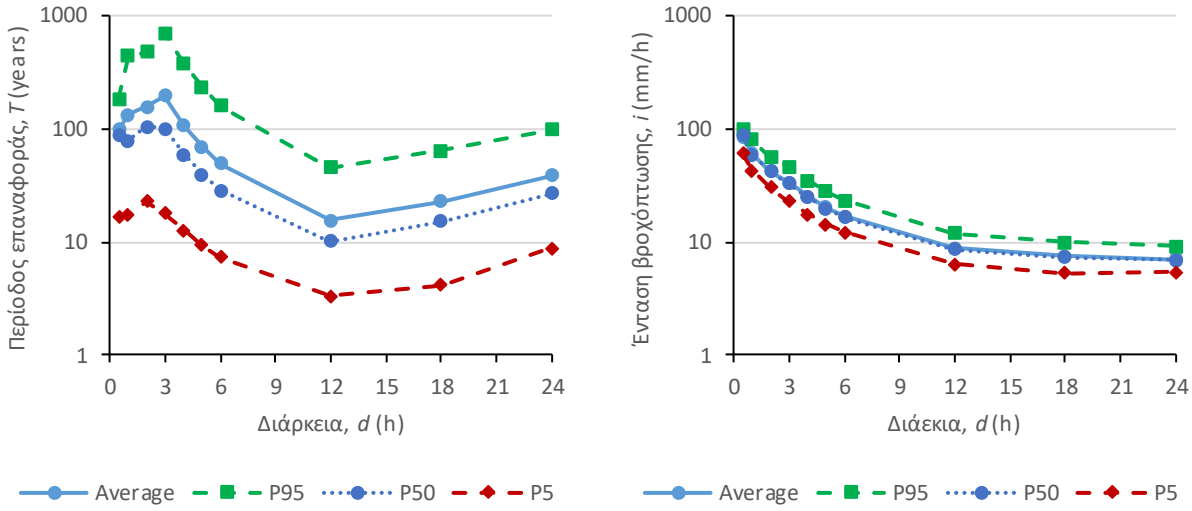

Σχήμα 5. Εκτιμήσεις περιόδου επαναφοράς (αριστερά) και μέγιστων εντάσεων βροχόπτωσης (δεξιά) με τα αντίστοιχα διαστήματα εμπιστοσύνης σε διάφορες χρονικές κλίμακες από ανάλυση Monte Carlo

Βασιζόμενοι στα αποτελέσματα των αναλύσεων Monte Carlo, παρέχουμε πιθανοτικές εκτιμήσεις της συνολικής βροχόπτωσης στην περιοχή μελέτης, της χρονικής της εξέλιξης, καθώς επίσης και της παροχής αιχμής του Σαρανταπόταμου στη θέση του υδρομετρικού σταθμού. Επίσης γίνεται και μία εκτίμηση των μέγιστων εντάσεων βροχόπτωσης και των αντίστοιχων περιόδων επαναφοράς, για διάφορες χρονικές κλίμακες. Τα αποτελέσματα αυτά τέλος συγκρίνονται και με άλλες πηγές πληροφοριών, σε μία προσπάθεια να εκτιμηθεί κατά πόσο τα αποτελέσματα της ανάλυσης αυτής κρίνονται αξιόπιστα.

Table of Contents

1. Introduction 19
   1.1 Study objective 19
   1.2 Study structure 19
2. The flood event of November 15th, 2017 21
   2.1 Brief information about the area 21
   2.2 The flood evolution 22
   2.3 Rainfall observations 23
3. Problem statement 25
4. Study area 27
   4.1 The basin of Sarantapotamos 27
   4.2 Available Data 28
      4.2.1 Hydrometric data 28
      4.2.2 Point rainfall data 29
5. Hydrological modeling tools 31
   5.1 Intensity – Duration – Frequency (IDF) Curves 31
   5.2 Flood Event Analysis 31
   5.3 The SCS – CN Method 32
      5.3.1 General procedure 32
      5.3.2 Maximum potential retention 33
      5.3.3 Standard estimation of curve number parameter 34
      5.3.4 Revised curve number assessment 36
      5.3.5 Adjustment to any AMC 39
   5.4 Unit Hydrograph 40
      5.4.1 Introduction 40
      5.4.2 The Parametric Synthetic Unit Hydrograph 40
   5.5 Lag-and-route method 41
6. Reverse rainfall – runoff procedure 43
   6.1 Model description 43
   6.2 Total rainfall 43
   6.3 Effective rainfall 43

6.4 Simulated Streamflow 43
6.4.1 Model A 43
6.4.2 Models B-I and B-II 44
6.5 Model calibration 44
6.5.1 Model A 44
6.5.2 Model B-I 45
6.5.3 Model B-II 46
6.6 Probabilistic analysis 46
7. Scenario-based approach 48
7.1 Model A 48
7.2 Model B-I 52
7.3 Model B-II 57
7.4 Discussion 62
8. Monte Carlo simulation 66
8.1 General information 66
8.2 Initial parameters 66
8.3 Model B-I 67
8.3.1 Simulation MC1-B-I 67
8.3.2 Simulation MC2-B-I 71
8.4 Model B-II 74
8.4.1 Simulation MC3-B-II 74
8.4.2 Simulation MC4-B-II 78
8.5 Discussion 81
9. Justification based on other sources of information 84
9.1 X-Band weather radar 84
9.2 Past flood events 86
10. Summary, conclusions and suggestions for future research 87
10.1 Summary 87
10.2 Conclusions 87
10.3 Suggestions for future research 90
11. Literature 91

11.1 Web Pages 94
Appendix A: Matlab code 95
Appendix A1: Model B-I 95
Appendix A2: Model B-II 100
Appendix A3: Probabilistic analysis 105

Table of Figures

Figure 2.1. Observed 30-min rainfall in the wider area 24
Figure 4.1. Observed streamflow at Gyra Stefanis 29
Figure 4.2. Observed 30-min rainfall in Vilia 30
Figure 5.1. CN II values vs CN I and CN III 36
Figure 5.2. Permeability classes (top left), vegetation classes (top right), drainage capacity classes (bottom left), CN classes (bottom right) for the basin of Sarantapotamos (Efstratiadis *et al.*, 2014) 39
Figure 5.3. Parametric synthetic unit hydrograph (Efstratiadis *et al.*, 2014) 41
Figure 6.1. Sarantapotamos parametric synthetic unit hydrograph for d = 0.5 h 44
Figure 7.1. Simulated X-Station 30-min rainfall (left) and streamflow at Gyra Stefanis (right) for scenario S1-A 49
Figure 7.2. Simulated X-Station 30-min rainfall (left) and streamflow at Gyra Stefanis (right) for scenario S2-A 50
Figure 7.3. Simulated X-Station 30-min rainfall (left) and streamflow at Gyra Stefanis (right) for scenario S3-A 50
Figure 7.4. Simulated X-Station 30-min rainfall (left) and streamflow at Gyra Stefanis (right) for scenario S4-A 51
Figure 7.5. Simulated X-Station 30-min rainfall (left) and streamflow at Gyra Stefanis (right) for scenario S5-A 51
Figure 7.6. Estimated return period vs time scale (duration) for the five hydrological scenarios using Model A 52
Figure 7.7. X-station simulated rainfall intensity vs time scale (duration) for the five hydrological scenarios using Model A 52
Figure 7.8. Simulated X-Station 30-min rainfall (left) and streamflow at Gyra Stefanis (right) for scenario S1-B-I 54
Figure 7.9. Simulated X-Station 30-min rainfall (left) and streamflow at Gyra Stefanis (right) for scenario S2-B-I 55
Figure 7.10. Simulated X-Station 30-min rainfall (left) and streamflow at Gyra Stefanis (right) for scenario S3-B-I 55
Figure 7.11. Simulated X-Station 30-min rainfall (left) and streamflow at Gyra Stefanis (right) for scenario S4-B-I 56
Figure 7.12. Simulated X-Station 30-min rainfall (left) and streamflow at Gyra Stefanis (right) for scenario S5-B-I 56
Figure 7.13. Estimated return period vs time scale (duration) for the five hydrological scenarios using Model B-I 57
Figure 7.14. X-station simulated rainfall intensity vs time scale (duration) for the five hydrological scenarios using Model B-I 57
Figure 7.15. Simulated X-Station 30-min rainfall (left) and streamflow at Gyra Stefanis (right) for scenario S1-B-II 59

Figure 7.16. Simulated X-Station 30-min rainfall (left) and streamflow at Gyra Stefanis (right) for scenario S2-B-II 60
Figure 7.17. Simulated X-Station 30-min rainfall (left) and streamflow at Gyra Stefanis (right) for scenario S3-B-II 60
Figure 7.18. Simulated X-Station 30-min rainfall (left) and streamflow at Gyra Stefanis (right) for scenario S4-B-II 61
Figure 7.19. Simulated X-Station 30-min rainfall (left) and streamflow at Gyra Stefanis (right) for scenario S5-B-II 61
Figure 7.20. Estimated return period vs time scale (duration) for the five hydrological scenarios using model B-II 62
Figure 7.21. X-station simulated rainfall intensity vs time scale (duration) for the five hydrological scenarios using model B-II 62
Figure 8.1. Average simulated rainfall at X-station and confidence intervals for 95%, 50% and 5% non-exceedance probability for simulation MC1-B-I..... 68
Figure 8.2. Average simulated streamflow at Gyra Stefanis and confidence intervals for 95%, 50% and 5% non-exceedance probability for simulation MC1-B-I..... 69
Figure 8.3. Total simulated rainfall at X-station vs antecedent moisture conditions coefficient for simulation MC1-B-I 69
Figure 8.4. Total simulated rainfall at X-station vs initial abstraction for simulation MC1-B-I 70
Figure 8.5. Total simulated rainfall at X-station vs maximum potential retention for simulation MC1-B-I 70
Figure 8.6. Estimated return period and confidence intervals for 95%, 50% and 5% non-exceedance probability vs time scale (duration) for simulation MC1-B-I 70
Figure 8.7. X-station simulated rainfall intensity and confidence intervals for 95%, 50% and 5% non-exceedance probability vs time scale (duration) for simulation MC1-B-I..... 71
Figure 8.8. Average simulated rainfall at X-station and confidence intervals for 95%, 50% and 5% non-exceedance probability for simulation MC2-B-I..... 71
Figure 8.9. Average simulated streamflow at Gyra Stefanis and confidence intervals for 95%, 50% and 5% non-exceedance probability for simulation MC2-B-I..... 72
Figure 8.10. Total simulated rainfall at X-station vs antecedent moisture conditions coefficient for simulation MC2-B-I 72
Figure 8.11. Total simulated rainfall at X-station vs initial abstraction for simulation MC2-B-I .. 73
Figure 8.12. Total simulated rainfall at X-station vs maximum potential retention for simulation MC2-B-I 73
Figure 8.13. Estimated return period and confidence intervals for 95%, 50% and 5% non-exceedance probability vs time scale (duration) for simulation MC2-B-I 73
Figure 8.14. X-station simulated rainfall intensity and confidence intervals for 95%, 50% and 5% non-exceedance probability vs time scale (duration) for simulation MC2-B-I..... 74
Figure 8.15. Average simulated rainfall at X-station and confidence intervals for 95%, 50% and 5% non-exceedance probability for simulation MC3-B-II 75

Figure 8.16. Average simulated streamflow at Gyra Stefanis and confidence intervals for 95%, 50% and 5% non-exceedance probability for simulation MC3-B-II 76
Figure 8.17. Total simulated rainfall at X-station vs antecedent moisture conditions coefficient for simulation MC3-B-II 76
Figure 8.18. Total simulated rainfall at X-station vs initial abstraction for simulation MC3-B-I .. 77
Figure 8.19. Total simulated rainfall at X-station vs maximum potential retention for simulation MC3-B-I 77
Figure 8.20. Estimated return period and confidence intervals for 95%, 50% and 5% non-exceedance probability vs time scale (duration) for simulation MC3-B-II 77
Figure 8.21. X-station simulated rainfall intensity and confidence intervals for 95%, 50% and 5% non-exceedance probability vs time scale (duration) for simulation MC3-B-II..... 78
Figure 8.22. Average simulated rainfall at X-station and confidence intervals for 95%, 50% and 5% non-exceedance probability for simulation MC4-B-II 79
Figure 8.23. Average simulated streamflow at Gyra Stefanis and confidence intervals for 95%, 50% and 5% non-exceedance probability for simulation MC4-B-II 79
Figure 8.24. Total simulated rainfall at X-station vs antecedent moisture conditions coefficient for simulation MC4-B-II 80
Figure 8.25. Total simulated rainfall at X-station vs initial abstraction for simulation MC4-B-II . 80
Figure 8.26. Total simulated rainfall at X-station vs maximum potential retention for simulation MC4-B-II 80
Figure 8.27. Estimated return period and confidence intervals for 95%, 50% and 5% non-exceedance probability vs time scale (duration) for simulation MC4-B-II 81
Figure 8.28. X-station simulated rainfall intensity and confidence intervals for 95%, 50% and 5% non-exceedance probability vs time scale (duration) for simulation MC4-B-II..... 81
Figure 9.1. Simulated hydrograph using the average rainfall estimated by the X-POL radar (Model B-I) 84
Figure 9.2. Average areal rainfall estimated by the X-POL radar vs average simulated areal rainfall for simulation MC1-B-I (left) and MC2-B-I (right) 85
Figure 9.3. Average areal rainfall estimated by the X-POL radar vs average simulated areal rainfall for simulation MC3-B-II (left) and MC4-B-II (right) 85
Figure 9.4. Peak flow at Gyra Stefanis vs average rainfall intensity for past flood events and Monte Carlo simulations 86

Table of Pictures

Picture 2.1. Map of the area (Google Earth) 21
Picture 2.2. Mandra industrial area on 15/11/2017 (Lekkas *et al.*, 2017) 22
Picture 2.3. Mandra-Elefsina road on 15/11/2017 (Lekkas *et al*., 2017) 23
Picture 2.4. XPOL accumulated rainfall (mm), from 14-Nov-2017 13:49 to 15-Nov-2017 12:00 (UTC) (*Kalogiros et al.*, 2017) 24
Picture 4.1. Hydrographic network of Sarantapotamos (Michailidi, 2013) 27
Picture 4.2. Soil permeability (left) and slope (right) of the catchment of Sarantapotamos (Koukouvinos, 2012) 28
Picture 4.3. Culvert cross-section (left) and stage-gauging sensor (right) (Koussis *et al.*, 2012) . 28
Picture 4.4. Meteorological station in Vilia (Source: Koussis *et al.*, 2012) 29
Picture 5.1. The linear reservoir approach 42
Picture 6.1. CCTV footage of the culvert during the flood 46

Table of Tables

Table 5.1. Curve Number values for selected agricultural, suburban and urban land use for antecedent moisture conditions Type II and initial abstraction ratio 20% (Chow *et al.*, 1988)... 35
Table 5.2. Water permeability classes based on soil and geological characteristics (Savvidou *et al.*, 2018) 37
Table 5.3. Vegetation classes based on land use/cover characteristics (Savvidou *et al.*, 2018).. 38
Table 5.4. Drainage capacity classes based on the average slope and related ground features (Savvidou *et al.*, 2018) 38
Table 5.5. Coding of the physiographic characteristics for the estimation of the reference Curve Number value (CN_{II}) (Savvidou *et al.*, 2018) 38
Table 6.1. Temporal scales for probabilistic analysis 47
Table 7.1. Hydrological scenarios and parameter sets for Model A..... 48
Table 7.2. Initial abstraction, curve number and maximum potential retention for each scenario using Model A 48
Table 7.3. Hydrological scenarios and parameter sets for Model B-I 53
Table 7.4. Initial abstraction, curve number and maximum potential retention for each scenario using Model B-II 53
Table 7.5. Hydrological scenarios and parameter sets for Model B-II 58
Table 7.6. Initial abstraction, curve number and maximum potential retention for each scenario using Model B-II 58
Table 7.7. Total and maximum simulated rainfall at X-station and simulated peak flow at Gyra Stefanis for each hydrological scenario 63
Table 7.8. Estimated return period vs time scale (duration) for each hydrological scenario 63
Table 7.9. Simulated rainfall intensity at X-station vs time scale (duration) for each hydrological scenario..... 64
Table 8.1. Initial abstraction ratio of past storm events (Efstratiadis *et al.*, 2014) 67
Table 8.2. Daily accumulated rainfall observed at the stations in Madra and Vilia 67
Table 8.3. Statistical characteristics of total and maximum simulated rainfall at X-station and peak flow at Gyra Stefanis for each simulation..... 82
Table 8.4. Statistical characteristics of estimated return period vs time scale (duration) for each Monte Carlo simulation 82
Table 8.5. Statistical characteristics of simulated rainfall intensity at X-station vs time scale (duration) for each Monte Carlo simulation..... 83
Table 10.1. Peak flow estimations with confidence intervals for each Monte Carlo simulation. 88
Table 10.2. Estimated return period and simulated rainfall intensity at X-station with their confidence intervals vs time scale (duration) for each Monte Carlo simulation 89

1. Introduction

1.1 Study objective

From November 14th until November 15th, 2017, a flash flood occurred in Western Attica (west of Athens, Greece) causing 24 fatalities in the city of Mandra. Apart from the loss of human lives, the city and the wider area suffered great economical losses, as well as substantial damages to the infrastructure. The storm causing the flooding was intense, but its spatio-temporal characteristics are yet unknown. After the event, a debate ensued on whether the devastating results were due to the extreme nature of the storm or due to poor flood protection works.

This study aims at resolving the question, by presenting information from various sources, including hydrometric data from the neighboring catchment of Sarantapotamos stream, point rainfall data from the wider area of interest, estimates of areal rainfall based on a meteorological radar and audiovisual material. It also attempts to unravel the flood event by reverse rainfall-runoff modeling and analyzes the available data, in an attempt to approximately estimate the return period of the storm.

Due to the limited data availability, by means of in situ observations, the analysis performed in this study is founded on uncertainty grounds. An assessment of this uncertainty is attempted though the employment of Monte Carlo simulations. Within our estimations, we also account for multiple sources providing qualitative information and assess whether such information reduces uncertainty.

1.2 Study structure

Chapter 1 contains the introduction.

Chapter 2 presents all information about the flood event of November 2017, the impact it had in the city of Mandra, as well as the collected rainfall observations.

Chapter 3 presents the problem statement and describes the reason why the hydrological investigation is focused on the catchment of Sarantapotamos.

Chapter 4 describes the study area, i.e. the sub-catchment of Sarantapotamos stream upstream of Gyra Stefanis, and its data.

Chapter 5 describes the hydrological modeling tools and methods used in this study.

Chapter 6 describes the reverse rainfall – runoff procedure and the implementation of the aforementioned models.

Chapter 7 presents hydrological scenarios, as they were simulated using the proposed models.

Chapter 8 describes the uncertainty assessment of the reverse procedure, through Monte Carlo simulations.

Chapter 9 compares the results of Monte Carlo analysis against rainfall estimations provided by a meteorological radar, as well as the reported results of studies of past flood events, during the period 2012-2014.

Chapter 10 contains the conclusions of this study, as well as suggestions for future research.

Finally, Appendix A contains the Matlab code for the proposed models.

2. The flood event of November 15th, 2017

2.1 Brief information about the area

On November 15th, 2017, a major flood event occurred in Western Attica. The main residential areas that have been affected were Mandra, Magoula, Nea Peramos and Elefsina, with Mandra being affected the most, by means of fatalities and economical losses. Mandra is a small industrial city located 40 km west of Athens (Picture 2.1), at the western part of Thriasio valley. The city was built in 1816 and people started moving there after the Greek War of Independence. However, the city has since grown significantly over the past years and is now considered to be one of the most extended logistics bases in Attica. According to the official census performed by the Hellenic Ministry of the Interior in 2011, it hosts 12.728 residents.

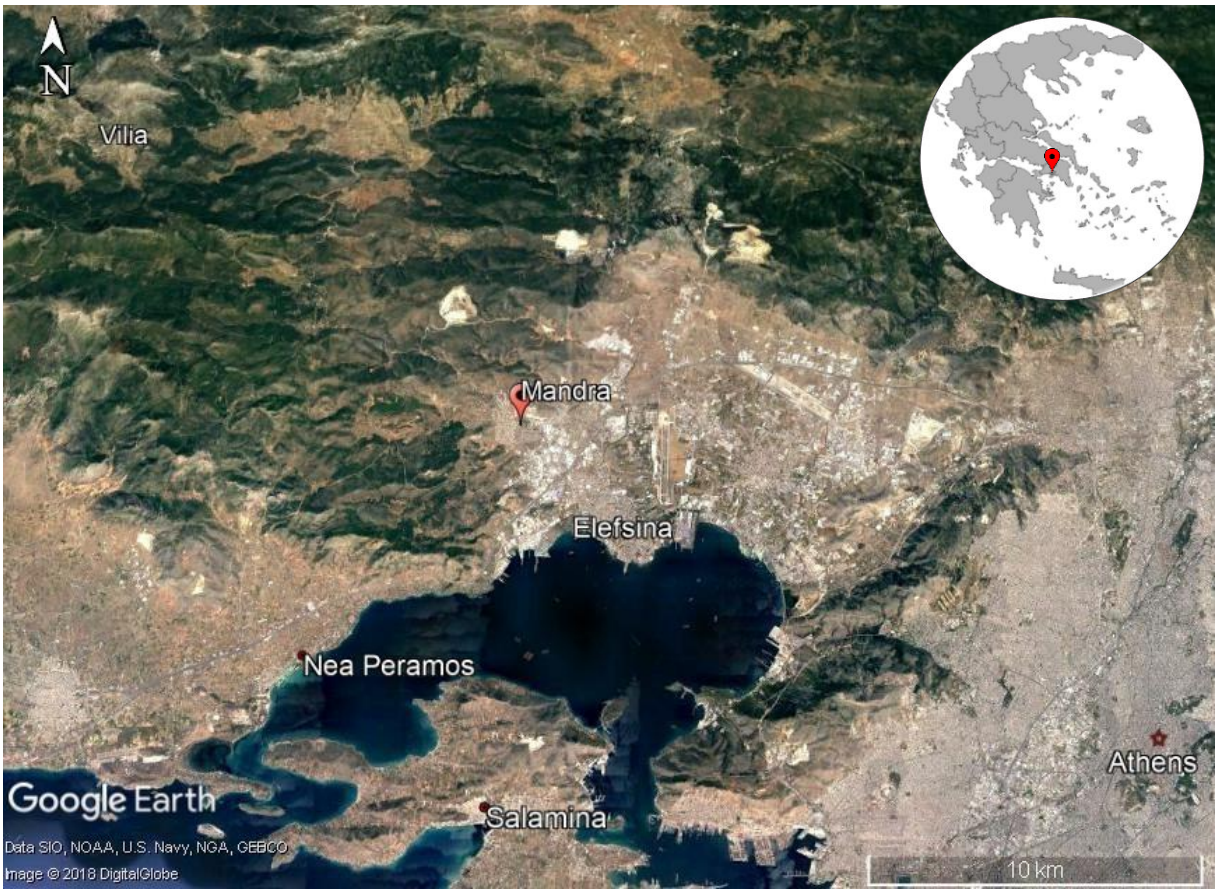

Picture 2.1. Map of the area (Google Earth)

The average altitude of the city of Mandra is 84 m above sea level and the coordinates of its center are 38°4'30.48"N and 23°30'3.22"E (Google Earth). The major geological formation of the area is limestone with high water permeability rates. The city is also crossed by two small ephemeral streams (i.e., Soures, Agia Aikaterini), draining an area of approximately 75 km^2. Both streams outflow in the bay of Elefsina.

In the past century, reports of major flood events in the area of interest are traced back to the decade of 1950. The first recorded flood was in 1953 and was followed by other flood incidents in 1961, 1963, 1977, 1978, 1996, 2003, 2015 and 2017 (https://www.tovima.gr; Lekkas *et al.*, 2017). From those records, the floods in 1961 and 1977 also claimed a large number of human lives, marking the incident of 2017 as the third most severe flood in Western Attica, in terms of fatalities (https://www.newsit.gr).

2.2 The flood evolution

During the afternoon hours of November 14th, around 8:00 pm, a rapid rainfall started over the mountainous area west of Mandra and continued throughout the night. In the morning hours of November 15th, around 7:00 am, a fast moving flood wave arrived at the city of Mandra causing substantial damages in the infrastructure of the city, as well as human fatalities (Apostolidis *et al*., 2017). Such fast moving flood waves caused by major rainfall intensities over short duration define a phenomenon called “flash flood”. It is commonly accepted that flash floods are the most common flood type observed in Greece, due to the climatic regime and the geomorphologic characteristics of the Greek basins (Koutsoyiannis *et al.*, 2012).

The intense storm that started at about 8:00 pm of November 14th initially caused a fast saturation of the soil, and also resulted to significant soil erosion and sediment accumulation in the streams around the area. The sediment transport kept rising as the time pasted and a rapid change in the rainfall during the morning hours of November 15th was responsible for the flash flood that affected the city of Mandra. Due to this flood volume, the soil erosion rose even higher leading finally to a significant volume of sediment materials being transported downstream, towards the urban and industrial areas (Picture 2.2) (Apostolidis *et al*., 2017).

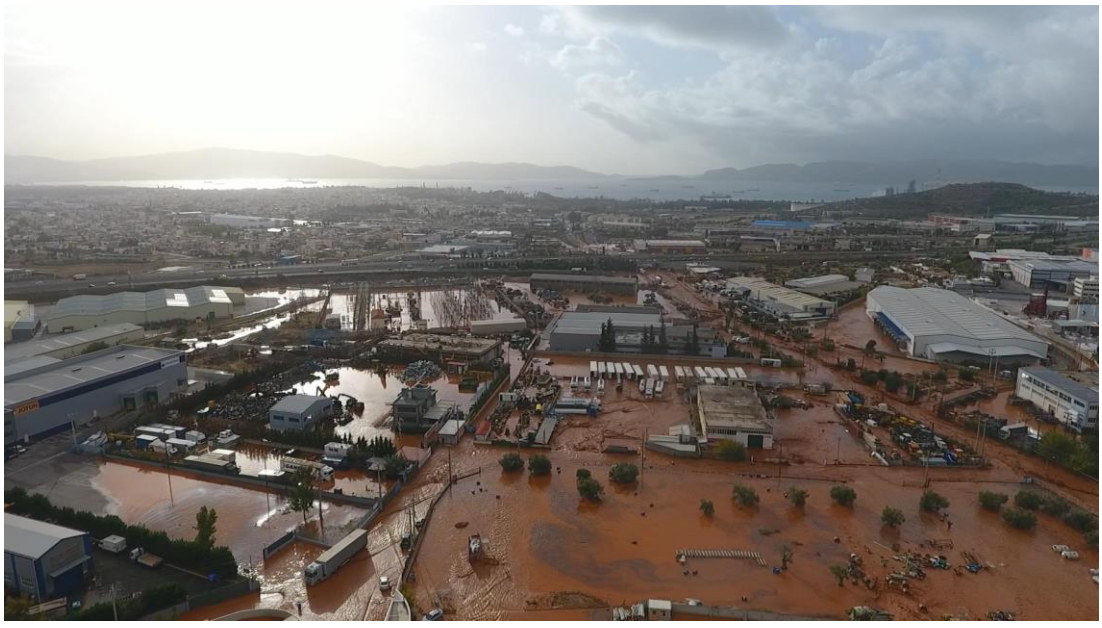

Picture 2.2. Mandra industrial area on 15/11/2017 (Lekkas et al., 2017)

Picture 2.3. Mandra-Elefsina road on 15/11/2017 (Lekkas et al., 2017)

The first flood wave appeared west of Mandra at around 7:00 am on November 15th. At 7:05, it reached the confluence of the two streams (e.g., Soures and Agia Aikaterini). The flood kept rising until about 8:00 am and then the water level started falling for the next two hours. From this confluence point, which is located approximately 100 m from the road connecting the cities of Mandra and Elefsina, the wave moved towards the drainage structures of highway E94 (Attiki Odos). Due to the large water volume, together with the large amounts of sediment materials, the flood protection works were overflowed and the flood moved downstream, mainly through the Mandra-Elefsina road (Picture 2.3) (Apostolidis *et al*., 2017).

2.3 Rainfall observations

There are three meteorological stations in the wider area around the city of Mandra, located in Mandra, Elefsina and Vilia (Picture 2.1). We remark that all stations are located outside the two catchments of interest, Soures and Agia Aikaterini. Nevertheless, these are the sole sources of point rainfall observations during the storm event, which are presented in Figure 2.1. It should be also noted that the largest rainfall depth was observed after the flood arrived at Mandra, while for approximately 10 hours before the flood there was no rainfall observed in the city of Mandra.

Surprisingly, the amount of the observed rainfall in these stations is rather small and cannot explain such a severe flooding. This realization can be further supported by the approximate yet indicative rainfall information recorded by an X-band weather radar. The image provided by the radar system (Picture 2.4) shows an elongated narrow core of the storm, passing outside the area covered by the three stations. The rainfall pattern estimated based on the radar data agrees with reports by residents in the catchments upstream of Mandra. According to these reports, a very

intense local storm event started in the early hours of November 15th and continued during the night.

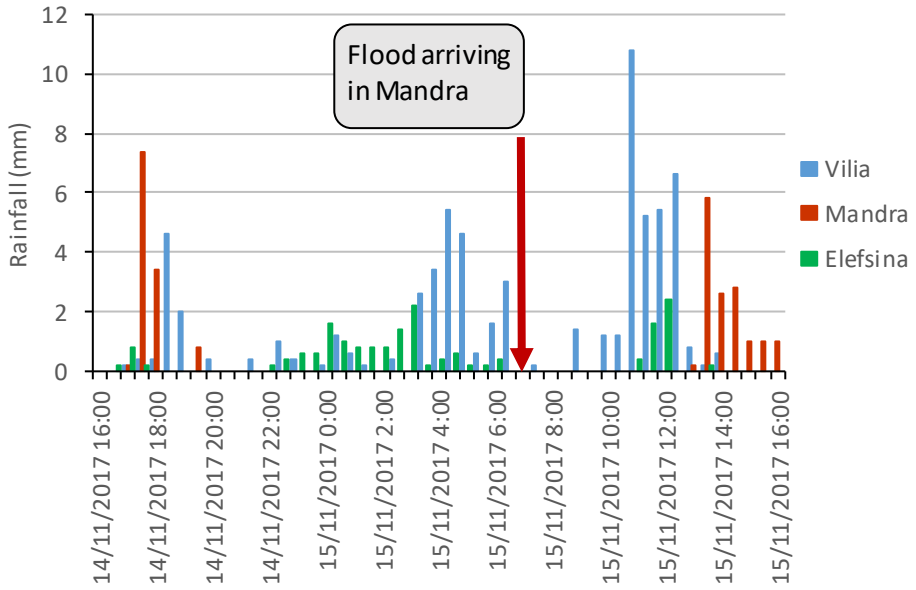

Figure 2.1. Observed 30-min rainfall in the wider area

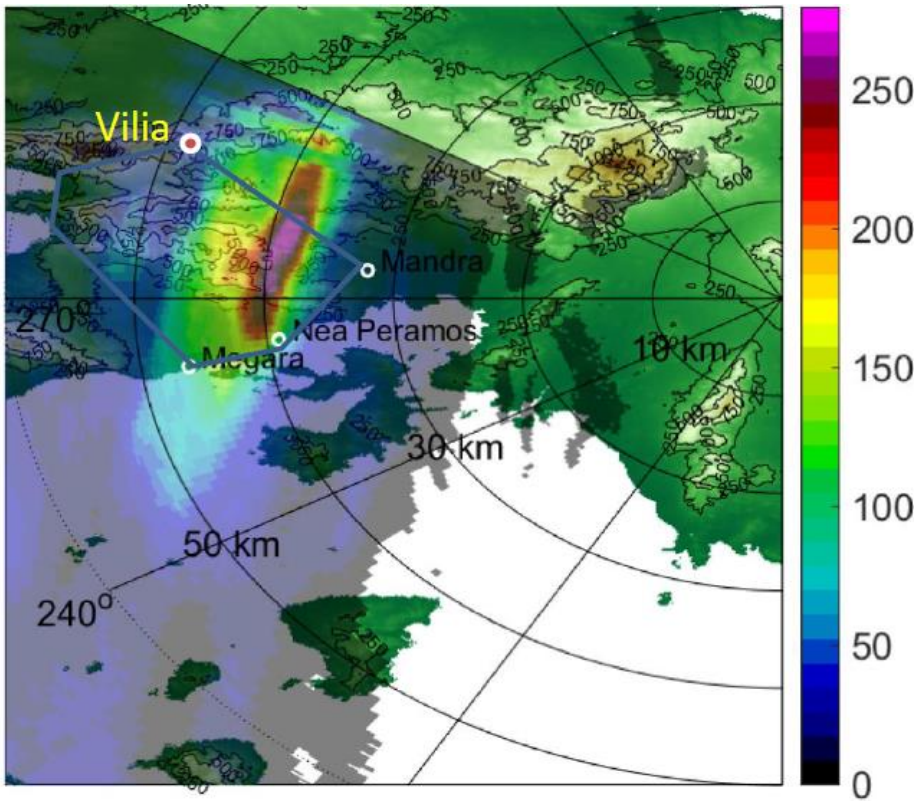

Picture 2.4. XPOL accumulated rainfall (mm), from 14-Nov-2017 13:49 to 15-Nov-2017 12:00 (UTC) (Kalogiros et al., 2017)

3. Problem statement

The European Union, in its Flood Directive 2007/60 (EC, 2007), defines flood as *"the temporary covering by water of land not normally covered by water"*. In a European level, floods are considered as the second most common physical catastrophe, with wildfires being the first. A flood is a physical phenomenon that has major impacts on the economic life and may be responsible for many losses of human lives. In this respect, numerous researchers focus their studies around floods and the generating mechanisms, also looking for ways to efficiently protect the population from them.

The flood in Western Attica had great social impact due to the magnitude of its catastrophic results. It was responsible for great economic loses and the loss of human lives and has been characterized as the third most severe flood in Western Attica in the past half century, in terms of fatalities. It also caused great damages in the infrastructure, mainly in the city of Mandra. This has led to a debate, about whether the catastrophic results were due to its extreme nature, or due to the poor flood protection works.

Many researchers tried to answer this question and this flood has been the case study of numerous scientific works. As an example, Markopoulos-Sarikas *et al.* (2018) presented a preliminary analysis of the urban flood inundation, by creating a 2-D flood model. However, due to the lack of information about the spatial and temporal evolution of the storm, they employed a scenario-based analysis, by running their hydraulic analyses considering steady flow conditions.

A typical flood event analysis, from a hydrological point of view, requires knowledge of three key components, i.e. the precipitation and its spatio-temporal characteristics, the flood volume and its evolution over time, and the physical mechanisms through which the precipitation is transformed into runoff and travels through the hydrographic network of basin. Modeling these components is key issue, in order to represent the flood event and assess the impact a future flood may have on human society.

In terms of precipitation observations, as stated in paragraph 2.3, the rainfall data collected from the meteorological stations around the area could not justify such a severe flooding. This fact made essential the use of approximate radar and satellite data, in an attempt to better describe the storm and its spatio-temporal characteristics. However, in addition to their inherent uncertainties, these systems require land observations to adjust their data.

The second setback in an attempted hydrologic analysis is the lack of hydrometric stations in the catchments upstream of Mandra. This means that no concrete observations of the flood flows are collected. In addition, determining the hydro-morphologic characteristics of the basin, on an event-based analysis is a complicated procedure with great uncertainty, which cannot be performed without the knowledge of the precipitation and runoff evolution over time.

A solution to this lack of information could be given by the neighboring catchment of Sarantapotamos. This catchment was also greatly affected by the storm and has quite similar geomorphological characteristic with the catchments upstream of Mandra. The dominant geological formation is limestone and the catchments have similar sizes, with similar slopes and vegetation.

Moreover, and more importantly, there is a hydrometric station located in the catchment of Sarantapotamos. This station is owned by the National Observatory of Athens and was installed in a concrete culvert near Gyra Stefanis. The station was used for studies conducted in the basin through the period of 2012-2014 and was still operated during the flood of November 2017, thus provided observations of the flows of Sarantapotamos. However, the instrument's assembly was destroyed during the flood, thus the available data do not cover the entire flood hydrograph.

Another valuable source of information is the rainfall observed at the meteorological station in Vilia. This station is located in the catchment of Sarantapotamos provided point rainfall data during the storm. Despite the fact that these observations alone cannot justify such a severe flooding, they could still prove useful in studying the storm.

To summarize, there are useful information sources to allow a representation of the rainfall-runoff event across the basin of Sarantapotamos. In addition, past studies in the area imply that the characteristics of the basin are not completely unknown. Based on all this knowledge, we attempted a hydrological analysis over the catchment of Sarantapotamos, in order to quantify the storm event over the study area. According to the results, and the underlying uncertainty, our outcomes could be expanded to the two small catchments upstream of Mandra.

4. Study area

4.1 The basin of Sarantapotamos

The area of interest is the catchment of Sarantapotamos. It covers an area of 310 km^2 and it is demarcated by the mountains Pateras to the west, Kitheronas to the northwest, Pastra to the north and Parnitha to the east. Sarantapotamos is the largest stream of West Attica, which passes through the Thriasio valley and outflows in the bay of Elefsina. The upstream system consists of two major streams, i.e. Pelkes, which crosses the valley of Oinoi, and St. Georgios, which crosses the valley of St. Georgios. The main branch of Sarantapotamos also joins the streams of St. Vlasios, Ksirorema and Megalo Katerini, while its most significant head is located on the mountain of Kitheronas, near the village of Vilia. The hydrographic network of the basin which is presented in Picture 4.1, mainly consists of streams with intermittent flow. However, the river regime of Sarantapotamos is also reported as ephemeral (Koutsoyiannis & Mamassis, 2001; Michailidi, 2013).

Picture 4.1. Hydrographic network of Sarantapotamos (Michailidi, 2013)

The study area is the sub-basin upstream of the hydrometric station at Gyra Stefanis. This part of the catchment is a narrow basin stretching from east to west and covers an area of 144.6 km^2. It is mostly mountainous, with slopes ranging from 10% to 30%, and in some areas up to 100% or even higher. The basin is also characterized by great water permeability, due to the karst limestone that extends over 84% of the basin. However, there are also parts with medium or low permeability, covering 7% and 9% of the study area, respectively. (Michailidi, 2013).

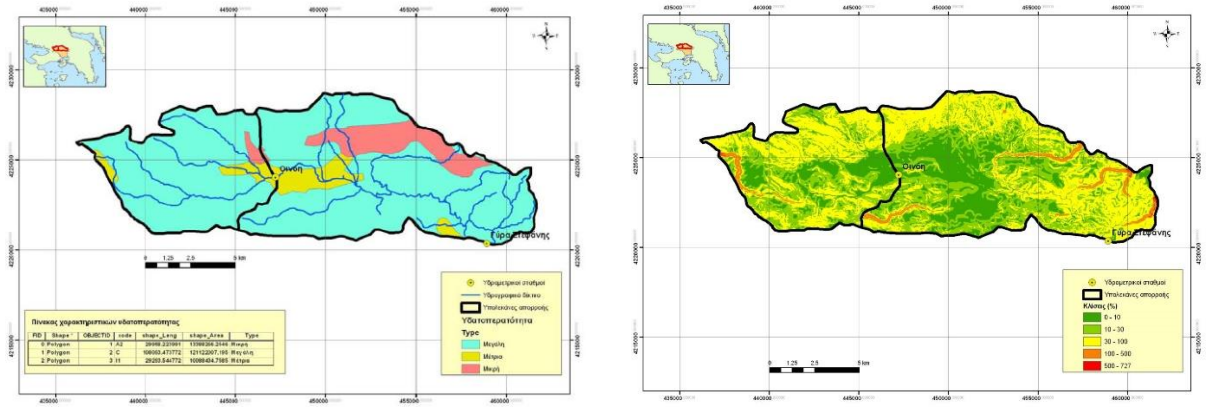

Picture 4.2. Soil permeability (left) and slope (right) of the catchment of Sarantapotamos (Koukouvinos, 2012)

4.2 Available Data

4.2.1 Hydrometric data

The hydrometric station is installed at a concrete culvert near Gyra Stefanis. The cross-section of the culvert is octagonal and it is covered by a small bridge. The sensor is located underneath the bridge and utilizes ultrasound waves to measure the stage of the stream in the middle of the culvert (Picture 4.3). Then, using the known stage-flow equation of the culvert, these measurements can be used to produce the observed streamflow (Koussis *et al.*, 2012).

The station was in operation during the storm event and provided stage data at 15 minute intervals. However, due to the extreme flows, the water rose rapidly to approximately 0.5 m from the stage-gauging sensor (the measuring limit of the sensor), and then overtopped the bridge above the culvert, also destroying the instrument's assembly. Thus, the available flow data, as shown in Figure 4.1, only captures part of the rising limb of the flood hydrograph.

Picture 4.3. Culvert cross-section (left) and stage-gauging sensor (right) (Koussis et al., 2012)

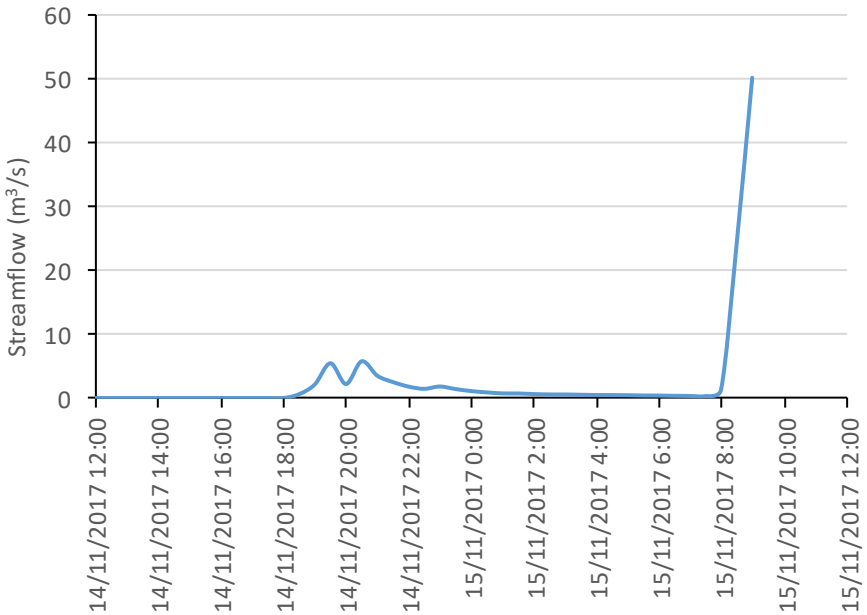

Figure 4.1. Observed streamflow at Gyra Stefanis

4.2.2 Point rainfall data

As mentioned in section 2.3, there are three meteorological stations located in the wider area, which were operational during the storm event. In particular, the station in the village of Vilia, is located inside the catchment of Sarantapotamos and the information gathered could prove useful in the reverse rainfall-runoff model (see chapter 5).

The station is located in the west-southwest edge of the settlement, at Vilia High School. The sensor is positioned approximately 4 m above ground level (Picture 4.4) and the collected data are transmitted via a stable internet connection, in 10-min intervals (Koussis *et al.*, 2012).

The point rainfall data during the storm of November 15th, aggregated to 30-min resolution, is presented in Figure 4.2.

Picture 4.4. Meteorological station in Vilia (Source: Koussis et al., 2012)

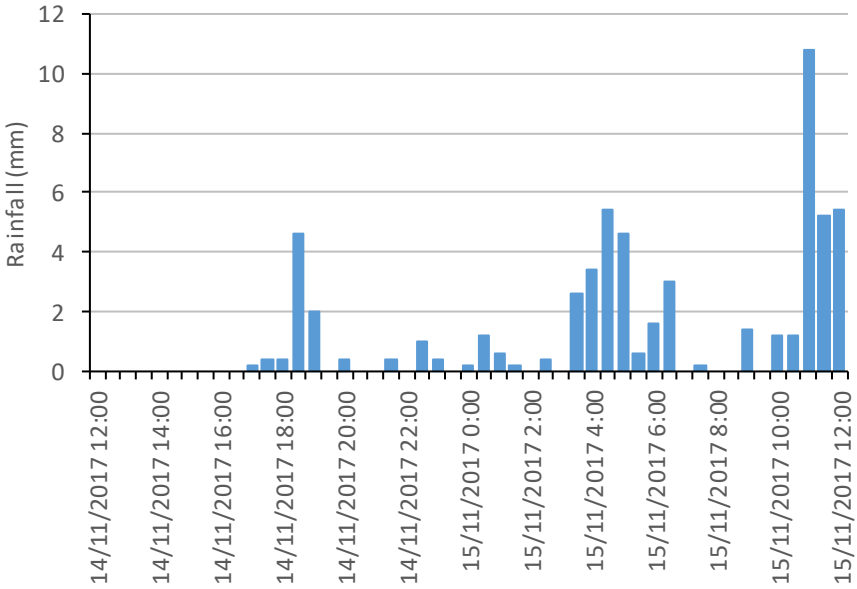

Figure 4.2. Observed 30-min rainfall in Vilia

5. Hydrological modeling tools

5.1 Intensity – Duration – Frequency (IDF) Curves

The idf curves are mathematical expressions that estimate the rainfall intensity, *i*, as function of time scale (duration), *d*, and frequency (return period), *T*. The idf curves are constructed through frequency analysis of maximum rainfall data at a specific site. The accuracy of the idf strongly depends on the availability of historical time series of maximum rainfall intensities for different durations and of significant length.

The commonly used expression of idf curves in Greece is given by (5.1):

$$i = \lambda \frac{T^k - \psi}{(1 + {}^{d}/_{\theta})^n} \tag{5.1}$$

where λ, k, ψ, θ and n are parameters, which can be determined by standard statistical approaches. The above formula and associated parameter estimation framework have been proposed by Koutsoyiannis *et al.* (1998). This methodology was recently applied over all River Basin Districts over Greece, within the implementation of the 2007/60/EU Floods Directive (Papaioannou *et al.*, 2018).

5.2 Flood Event Analysis

The base component of a hydrograph is a low flow that remains even during extended drought periods, which leads to the conclusion that it is not directly associated with to recent precipitation events. On the other hand, during intense rainfall events, the river basin system responds rapidly, as streamflow increases substantially, which is indicative that part of the precipitation follows a quick route across the basin. This behavior makes it apparent that the runoff consists of two components: the base runoff (or slowflow) and the direct runoff (or quickflow).

The quickflow can be further analyzed into a direct flow over the terrain (surface flow) and a subsurface (or hypodermic) flow through the soil. Essentially, the direct runoff is the product of the effective rainfall and is characterized by a time delay, due to the time needed by the runoff to reach the basin outlet. It is also considered that the water volume remains the same, or in other words, the total volume of the base runoff matches the total volume of the effective rainfall. On the other hand, the groundwater flow is generally little associated with the flood volume, with the exception of karst systems that have very rapid response, thus part of the groundwater flow may also contribute to direct runoff.

According to the nature of the base runoff, the flow can be divided in three major categories (Efstratiadis et al., 2012):

- perennial, when there is a steady flow throughout the year

- intermittent, when the flow is only observed during the wet period
- ephemeral, when there is no base runoff and the flow is only observed during severe storm events

A typical flood event analysis first requires separating the direct and the base runoff and thus determining the flood hydrograph. Next step is estimating the hydrological abstractions, namely the part of the rainfall that is initially retained by the soil and vegetation. The knowledge of the temporal evolution of the rainfall event and the total abstraction is critical for estimating the part of rainfall that is converted into runoff, also known as effective rainfall or rainfall excess. By separating the direct and the base runoff, the flood hydrograph can be determined and, consequently, the volume of the effective rainfall. By comparing this with the total rainfall volume one can estimate the total volume retained by the soil and vegetation, but not their temporal evolution, which requires specialized methods. One of these methods is presented below.

5.3 The SCS – CN Method

5.3.1 General procedure

One of the most widely used methods for extracting the effective rainfall from the total rainfall, thus estimating the hydrological abstraction, is that of the runoff Curve Number (CN), developed by the Soil Conservation Service (SCS; now referred to as National Resources Conservation Service, NRCS) of the U.S. Department of Agriculture (SCS, 1972).

In order to describe the temporal evolution of the hydrological abstraction during the rainfall event, the SCS-CN method makes the following assumptions (Koutsoyiannis & Xanthopoulos, 1999):

- For an initial time interval, $t_{\alpha 0}$, the entire rainfall is considered as abstraction and no effective rainfall is produced. Consequently, after this time, the maximum effective rainfall cannot exceed the potential quantity, $h - h_{\alpha 0}$, where h is the total rainfall and $h_{\alpha 0}$ is the initial abstraction.
- Beyond the quantity $h_{\alpha 0}$, the additional abstraction during a large storm event cannot exceed a quantity called maximum potential retention, S.
- At any time interval $t > t_{\alpha 0}$, the ratios of the effective rainfall, h_e, and the total minus the initial abstraction, $h_\alpha - h_{\alpha 0}$, equal the respective potential quantities, $h - h_{\alpha 0}$ and S.

Following these assumptions, the effective rainfall can be extracted as shown in relation (5.2):

$$h_e = \begin{cases} 0 & h \le h_{a0} \\ \dfrac{(h - h_{a0})^2}{h - h_{a0} + S} & h > h_{a0} \end{cases} \tag{5.2}$$

The initial abstraction $h_{\alpha 0}$ is typically calculated as portion of the maximum potential retention, as shown in eq. (5.3):

$$h_{a0} = a\,S \tag{5.3}$$

By doing so, eq. (5.2) can be written as:

$$h_e = \begin{cases} 0 & h \le \alpha\,S \\ \dfrac{(h-\alpha\,S)^2}{h+(1-\alpha)S} & h > \alpha\,S \end{cases} \tag{5.4}$$

where α is the initial abstraction ration and takes values between 0 and 0.4. The recommended value in the literature is 0.20 (Ponce and Hawkins, 1996). However, this value resulted from studies conducted in small agricultural basins with mild slopes and significant recession in the USA. Reported experience from basins around the world has shown that the initial abstraction ratio could be 0.05 or even lower (Soulis *et al.*, 2012; Banasik *et al.*, 2014).

5.3.2 Maximum potential retention

Provided that runoff measurements are available for a specific flood event, the corresponding maximum potential retention, *S*, is calculated using eq. (5.5) (Koutsoyiannis & Xanthopoulos, 1999).

$$S = 5h + 10h_e - 10\sqrt{h_e(h_e + 1.25h)} \tag{5.5}$$

The above formula is based on the assumption that the ratio of the initial abstraction, α, equals to 20%. In the general case, for any other value of α, we use eq. (5.6) (Efstratiadis *et al.*, 2014):

$$S = \frac{2\alpha h + (1-a)h_e - \sqrt{h_e[h_e(1-\alpha)^2 + 4\alpha h]}}{2a^2} \tag{5.6}$$

In ungauged basins, the maximum potential retention can be derived by taking into account the curve number, *CN*, as shown in the empirical relationship (5.7):

$$S = 254\left(\frac{100}{CN} - 1\right) \tag{5.7}$$

The maximum potential retention, *S*, computed by eq. (5.7), uses again the assumption that the initial abstraction ratio, α, is 20% (thus symbolized S_{20}). In order to estimate the potential maximum retention for any value of α, we apply the following steps:

- The total effective rainfall, h_e, is calculated according to *h* and S_{20}, using eq. (5.4)
- Eq. (5.6) is solved for the given *h*, h_e and α to provide the maximum potential retention, S_α
- The initial abstraction is then calculated by (5.3), where *S* is now substituted by S_α

5.3.3 Standard estimation of curve number parameter

The curve number was adapted by the SCS in order to embrace the physiographic characteristics of each basin that are associated with runoff generation into a unique numerical value. It takes values between 0 and 100 and is affected by the soil type, the land cover characteristics and the antecedent soil moisture conditions (AMC) in the basin.

SCS typically identifies four hydrological soil groups, based on their infiltration and transpiration rates. Soils exhibiting high, moderate, low and very low rates of infiltration fall into groups A, B, C and D, respectively. The classification is determined as follows:

- Group A: Soils with low runoff potential and high infiltration rates, even when they are thoroughly wetted (e.g., sand, loamy sand or sandy loam).
- Group B: Soils with moderate infiltration rates even when thoroughly wetted (e.g., slit loam or loam).
- Group C: Soils with low infiltration rates even when thoroughly wetted (e.g., sandy clay loam).
- Group D: Soils with the highest runoff potential and very low infiltration rates even when thoroughly wetted (e.g., clay loam, silty clay loam, sandy clay, silty clay and clay).

SCS also considers three types of antecedent moisture conditions, namely Type I (dry), Type II (medium) and Type III (wet). These are determined by considering the accumulated rainfall of the past 5 days, as follows:

- Type I: Dry conditions, which correspond to accumulated rainfall of the past five days lower than 13 mm (or 35 mm for the growing season).
- Type II: Medium conditions, which correspond to accumulated rainfall of the past five days between 13 and 38 mm (or 35 and 53 mm for the growing season).
- Type III: Wet conditions, which correspond to accumulated rainfall of the past five days larger than 38 mm (or 53 mm for the growing season).

For Type II AMC and initial abstraction ratio 20% (henceforth referred to as reference conditions), the SCS provides tabularized values of CN (henceforth referred to as reference curve number) for every soil type and the respective land use. An example is given in Table 5.1, adapted by Chow *et al.*, 1988 (a summary of which is published by Koutsoyiannis, 2011).

Table 5.1. Curve Number values for selected agricultural, suburban and urban land use for antecedent moisture conditions Type II and initial abstraction ratio 20% (Chow et al., 1988)

Land Use Description		Hydrologic Soil Group			
		A	B	C	D
Cultivated land:	without conservation treatment	72	81	88	91
	with conservation treatment	62	71	78	81
Pasture or range land:	poor condition	68	79	86	89
	good condition	39	61	74	80
Meadow:	good condition	30	58	71	78
Wood or forest land:	thin stand, poor cover, no mulch	45	66	77	83
	good cover	25	55	70	77
Open Spaces, lawns, parks, golf courses, cemeteries, etc.:	good condition: grass cover on 75% or more of the area	39	61	74	80
	fair condition: grass cover on 50% to 75% of the area	49	69	79	84
Commercial and business areas (85% impervious)		89	92	94	95
Industrial districts (72% impervious)		81	88	91	93
Residential:					
Average lot size	Average % impervious				
1/8 acre or less	65	77	85	90	92
1/4 acre	38	61	75	83	87
1/3 acre	30	57	72	81	86
1/2 acre	25	54	70	80	85
1 acre	20	51	68	79	84
Paved parking lots, roofs, driveways, etc.		98	98	98	98
Streets and roads:	paved with curbs and storm sewers	98	98	98	98
	gravel	76	85	89	91
	dirt	72	82	87	89

For the other two antecedent soil moisture conditions (Type I and Type III), the corresponding curve number values are linked to that of Type II through eqs. (5.8) and (5.9).

$$CN_I = \frac{4.2\ CN_{II}}{10 - 0.058\ CN_{II}} \tag{5.8}$$

$$CN_{III} = \frac{23\ CN_{II}}{10 + 0.13\ CN_{II}} \tag{5.9}$$

These relationships, which are plotted in Figure 5.1, are based on the initial field experiments that classified the estimated CN values in classes with exceedance probability of 90% and 10% and used the assumption that the initial abstraction ratio is 20%.

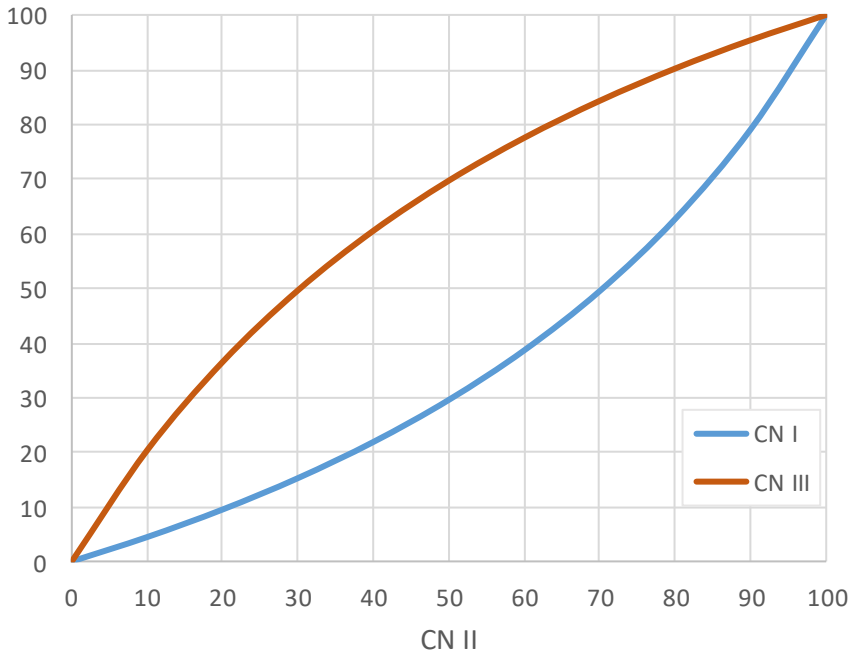

Figure 5.1. CN II values vs CN I and CN III

5.3.4 Revised curve number assessment

The typical CN method does not take into account the effect of slope. Actually, the studies that provided the reference CN values presented in the standard SCS tables (e.g. Table 5.1), were mainly conducted in agricultural basins with mild slopes, considering that the rainfall transformation into runoff is only affected by the soil and land cover characteristics. However, steep slopes cause a reduction of initial abstractions, a decrease in infiltration and a reduction of the recession time of overland flow, which in turn results in increased surface runoff.

Another shortcoming of the standard CN method is that the classification of soil types does not cover adequately the entire range of permeability characteristics of a number of geological formations. For instance, numerous Mediterranean basins lie in highly permeable terrain (e.g., limestone, dolomite, karst), resulting in very low runoff rates. According to the typical classification by SCS, these should be classified into Group A, but experience has shown that the associated CN values were quite overestimated.

Recently, in order to address the aforementioned shortcomings, some modifications have been proposed to the standard CN method, resulting in a semi-automated procedure for estimating the reference CN value using GIS tools. Input geographical data for the production of the associated thematic layers in rural areas may include hydro-lithological or soil maps, land use/cover maps, terrain slope maps and any other relevant information, while in urban or suburban areas, information about building features may also be accommodated as any other relevant urban features. The resulting classification is based on the categorization of three physiographic characteristics, each one comprising five classes, namely soil permeability and

near-surface geologic data, land use/cover and drainage capacity (Efstratiadis *et al.*, 2014; Savvidou *et al.*, 2018).

Permeability classifications in rural areas take into consideration the mechanical properties of the soil and the unsaturated zone that affect infiltration, interflow and percolation mechanisms. The permeability class is selected based on hydro-lithological or soil maps and depending on the predominant soil type, underlying geological formation and structures (for urban or suburban areas). In urban areas on the other hand, the corresponding classification is defined by the density of structures, building features and open space development (Table 5.2).

Table 5.2. Water permeability classes based on soil and geological characteristics (Savvidou et al., 2018)

Permeability Class	Ground Features	Geological or hydrological characteristics	Structure features
Very High	Very light and very well drained soils	Strongly karstified carbonate formations, extensive development e.g. fractured limestones, dolomites, marbles	
High	Sandy and gravelly soils, with a small percentage of slit and clay	Fluvial deposits, inconsistent conglomerates, breccia triadic	Very small settlements
Moderate	Thick sandy soils, silty and silty soils, sandy clay	Granular alluvial deposits, schists, cohesive conglomerates, platy or fine grained limestone alternating with schist formations	Sparsely built areas, significant garden development, urban parks
Low	Fine clay soils, soils from clay, soils poor in organic material	Flysch, metamorphic, plutonic and volcanic rocks, granular non-alluvial deposits (alternating sands, marls, clays, conglomerates, marly limestones, sandstones), granular molasse deposits	Moderately built areas with lawns and small gardens
Very Low	Shallow soils that swell when wetted, plastic clays	Compact rock of negligible permeability (granites)	Shopping centers, densely built areas

Vegetation classifications account for land characteristics related to retention mechanisms, soil roughness and filtration capacity, for example due to root zone growth. Based on a relevant land use map, the vegetation class of the area of interest is selected. As for burned areas, it is recommended to be classified with respect to their original condition (Table 5.3).

The drainage capacity of the examined area depends on geomorphological characteristics (topography, slope), the development of the river network and the existence of runoff regulation systems across the area of interest (e.g., land reclamation works, retention structures, sewer

networks). In the absence of other information, this classification can be performed on the basis of terrain slope (Table 5.4).

According to the above classifications, the dominant classes of permeability, land use/cover and drainage capacity, as well as the corresponding indices i_{PERM}, i_{VEG} and i_{SLOPE}, are assigned for the given area (Table 5.5).

Table 5.3. Vegetation classes based on land use/cover characteristics (Savvidou et al., 2018)

Vegetation Class	Land use/cover characteristics
Dense	Forests (conifers, broadleaf)
Moderate	Transitional forests, orchards, olive groves, riparian vegetation
Low	Pastures, crops, vineyards, grassland, scrub
Sparse	Fallow land, non-irrigated arable land, dunes, wetlands, scattered construction
Negligible	Bare or rocky soil, artificial surfaces (roads, buildings)

Table 5.4. Drainage capacity classes based on the average slope and related ground features (Savvidou et al., 2018)

Drainage capacity class	Average slope	Other features
Negligible	0 %	Inadequate drainage system, frequent and extensive bedsores, unformatted hydrographic network
Low	1-2 %	Significant surface degradation, occasional bedsores, poorly shaped river network
Moderate	2-10 %	Small surface degradation, rare flooding, shallow, small drainage corridors
High	10-30 %	Negligible soil degradations, very well shaped hydrographic network, existence of drainage network
Very High	30 %	Mountainous terrain

Table 5.5. Coding of the physiographic characteristics for the estimation of the reference Curve Number value (CN_{II}) (Savvidou et al., 2018)

Permeability Class	i_{PERM}	Vegetation Class	i_{VEG}	Drainage Capacity Class	i_{SLOPE}
Very High	1	Dense	1	Negligible	1
High	2	Moderate	2	Low	2
Moderate	3	Low	3	Moderate	3
Low	4	Sparse	4	High	4
Very Low	5	Negligible	5	Very High	5

Based on the above characteristic values, the reference Curve Number (CN_{II}) is estimated using the empirical relationship (5.10). According to this, the minimum CN_{II} value is 28, while the maximum is 100. The former refers to the extreme case of areas with very high permeability, dense vegetation and negligible drainage capacity, while the latter is by definition applicable to

areas covered by water bodies (rivers, lakes, etc.), where the entire rainfall is converted into runoff.

$$CN_{II} = 10 + 9 * i_{PERM} + 6 * i_{VEG} + 3 * i_{SLOPE} \quad (5.10)$$

where the three multipliers reflect the relative impacts of the corresponding physiographic characteristics to surface runoff generation.

For a river basin comprising multiple classes of each category, a weighted average CN_{II} can be used, according to the area covered by each individual class. If the area presents considerable variability with respect to CN values, it is recommended to be divided into smaller spatial elements.

An example is presented in Figure 5.2, as it was performed for the study basin of Sarantapotamos by Efstratiadis *et al.* (2014). The resulting reference Curve Number is CN_{II} = 48.

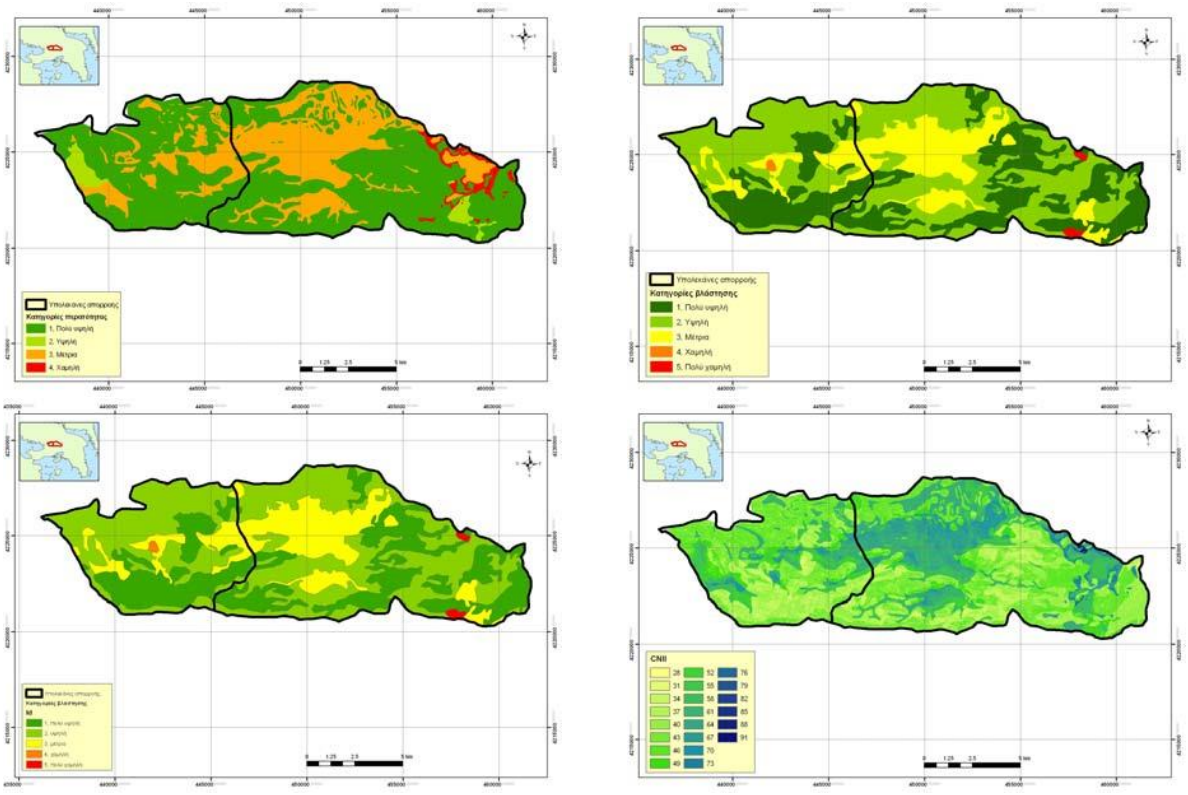

Figure 5.2. Permeability classes (top left), vegetation classes (top right), drainage capacity classes (bottom left), CN classes (bottom right) for the basin of Sarantapotamos (Efstratiadis et al., 2014)

5.3.5 Adjustment to any AMC

In our analyses, we also employ a continuous instead of a discrete classification of antecedent moisture conditions, by introducing a dimensionless parameter, symbolized AMC_{coef}. As shown in eq. (5.11), this parameter takes values between 0 and 1, with 0.5 corresponding to Type II soil conditions, 0.1 corresponding to Type I and 0.9 referring to Type III. Under this premise, the curve number is adapted as follows:

$$CN_{cor} = \begin{cases} CN_{II} - \dfrac{CN_{II} - CN_{I}}{0.4}\left(0.5 - AMC_{coef}\right), AMC_{coef} < 0.5 \\ CN_{III} + \dfrac{CN_{III} - CN_{II}}{0.4}\left(AMC_{coef} - 0.5\right), AMC_{coef} \geq 0.5 \end{cases} \quad (5.11)$$

5.4 Unit Hydrograph

5.4.1 Introduction

A unit hydrograph (UH) of duration *d* is called the hypothetical hydrograph produced by effective rainfall h_0 = 10 mm and intensity $i = h_0/d$. This rainfall is assumed uniform over space and time, thus a constant intensity is considered across the basin. In summary, the unit hydrograph describes the temporal transformation of the effective rainfall into direct runoff at the basin outlet. Apparently, a unique UH corresponds to a specific duration.

The UH method is based on two principles:

- The principle of proportionality: Two effective rainfalls of the same duration but with different intensity produce hydrographs with the same base time and at every time step the ratio between their ordinates (discharge) is equal to the ratio of their intensities.
- The principle of superposition: The total hydrograph produced by individual rainfalls is the hydrograph with ordinates the sum of the ordinates of each individual hydrograph. The start time of each individual hydrograph coincides the start time of each individual effective rainfall.

The UH of a standard duration is a characteristic conceptual property of the basin, which can be theoretically determined on the basis of observed rainfall and runoff data (yet after employing several modeling assumptions). In ungauged basins, synthetic methods are usually applied, thus the resulting UH is called Synthetic Unit Hydrograph (SUH). According to these methods the shape of the UH is based upon the physiographic characteristics of the basin.

5.4.2 The Parametric Synthetic Unit Hydrograph

The Parametric Synthetic Unit Hydrograph (PSUH) was proposed by Efstratiadis *et al.* (2014) and Michailidi (2018) (Figure 5.3). The time to peak, t_p, and base time, t_b, are calculated by:

$$t_p = d/2 + \beta\, t_c \quad (5.12)$$

$$t_b = d + \gamma\, t_c \quad (5.13)$$

where *d* is the unit rainfall duration, t_c is the time of concentration of the basin and β, γ are parameters, with $0 < \beta < 1$ and $\gamma \geq 1$. The two time quantities, t_p and t_b, are then rounded up to be expressed as integer multipliers of *d*.

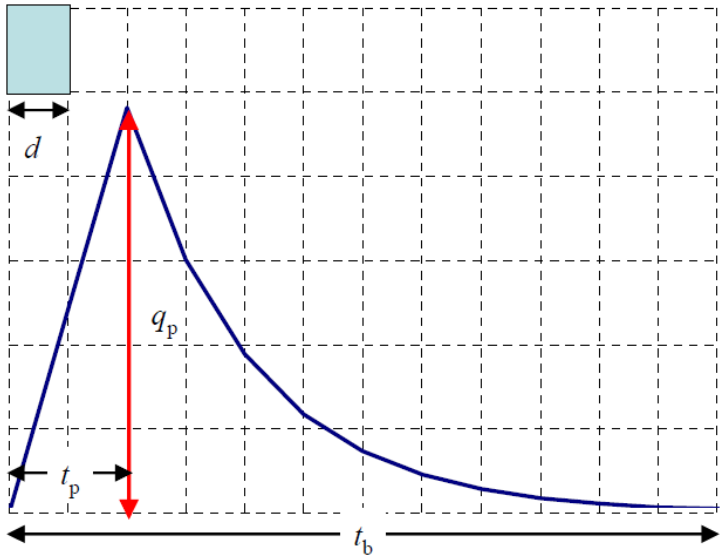

Figure 5.3. Parametric synthetic unit hydrograph (Efstratiadis et al., 2014)

Since t_p, t_b, β, γ are determined, the ordinates of the PSUH can be calculated by:

$$u(t) = q_p \; t/t_p, \quad t \le t_p \tag{5.14}$$

$$u(t) = q_p \exp(-k \; t/t_b), t > t_p \tag{5.15}$$

where q_p is the peak discharge and k is a recession parameter such as for $t = t_b$, the discharge is equal to a conventionally minimum value, q_0. Michailidi (2018) proposed to employ a value equal to 0.001 A, where A is the basin area in km^2. Therefore, the specific minimum discharge at time t_b is assumed to be 0.001 m^3/s/km^2.

In this respect, the analytical expression for k is:

$$k = -\ln(q_0/q_p) \tag{5.16}$$

The procedure for determining the peak discharge, q_p, has no analytical solution. In contrast, it requires a repetitive arithmetic procedure, based on the continuity equation. More specifically, the flood volume calculated by the PSUH should be equal to the total flood volume, $V_0 = h_0 A$, generated by a unit rainfall, where A is the basin area and h_0 = 10 mm.

5.5 Lag-and-route method

An alternative approach for propagating the runoff which is generated over the basin's surface to its outlet, thus determining the resulting flood hydrograph, is to consider that the basin behaves like a linear reservoir. In this modeling scheme, the inflow, *i(t)*, represents the effective rainfall, the outflow, *q(t)*, represents the generated runoff at the basin outlet and the storage component represents the various recession mechanisms across the basin. The procedure is described below and presented in Picture 5.1.

The generated runoff at each time step, *r(t)*, is calculated using eq. (5.17):

$$r(t) = h_e(t) - h_e(t-1) \tag{5.17}$$

where $h_e(t)$ is the accumulated effective rainfall.

At each time step, the storage is given by eq. (5.18):

$$s(t) = s(t-1) + r(t) - q(t) \tag{5.18}$$

where $q(t)$ is the generated runoff, given by eq. (5.19):

$$q(t) = k\, s(t-\tau) \tag{5.19}$$

where k is a recession parameter and τ is a lag time parameter.

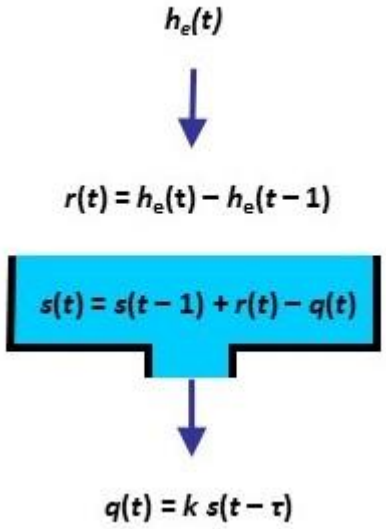

Picture 5.1. The linear reservoir approach

6. Reverse rainfall – runoff procedure

6.1 Model description

In our work we aim to determine the rainfall time series (called *XRain*) at a hypothetical station (called X-station) located in the catchment of Sarantapotamos for approximately 24 hours before the flood. Two different modeling schemes are presented, namely Model A and Model B. As for Model B, two alternative formulations are also presented (B-I and B-II), differing in the way they are calibrated (see paragraph 6.5).

Model A was developed in Microsoft Excel and uses the lag-and-route method for propagating the generated runoff to the basin outlet, while Model B was developed using the Matlab programming environment and propagates the generated runoff to the basin outlet using the parametric unit hydrograph approach.

6.2 Total rainfall

The models make the key assumption that the hypothetical station controls 80% of the rainfall over Sarantapotamos basin, upstream of Gyra Stefanis. The rest 20% is controlled by the rainfall station at Vilia (called *ViliaRain*) (see Figure 4.2). Thus, the areal rainfall over the study area is given by eq. (6.1):

$$h = 0.8\,XRain + 0.2\,ViliaRain \tag{6.1}$$

6.3 Effective rainfall

The effective rainfall, h_e, is extracted using the SCS – CN method, as presented in paragraph 5.3, by setting a reference Curve Number equal to CN_{II} = 48, as estimated by Efstratiadis *et al.* (2014) (see paragraph 5.3.4). Thus, the remaining model parameters are the initial abstraction ratio, a, and the antecedent moisture conditions coefficient, AMC_{coef}. In a reverse rainfall-runoff approach, these should be known a priori. However, since the model is conceptual, its parameters are subject to substantial uncertainties. In order to evaluate the model behavior, we manually assigned random (yet realistic) values to the two quantities at the beginning of each simulation, and then run the calibration scheme with hypothetically known parameters for the SCS – CN module and unknown rainfall depths.

6.4 Simulated Streamflow

6.4.1 Model A

Model A is a lag-and-route model (see paragraph 5.5), thus considers that the basin behaves like a linear reservoir to produce the simulated streamflow at Gyra Stefanis. Similarly to the SCS – CN

models, the two parameters used by the model, e.g. the recession parameter, *k*, and the lag time parameter, *τ*, are chosen randomly at the beginning of each simulation.

6.4.2 Models B-I and B-II

Models B-I and B-II use the Parametric Synthetic Unit Hydrograph of Sarantapotamos basin to reproduce the simulated streamflow at the hydrometric station of Gyra Stefanis. The PSUH used in this study was developed by Michailidi (2018), based on the analysis of observed flood events during the years 2012-2014, which are reported by Efstratiadis *et al.* (2014). The PSUH for half-hour rainfall duration (equal to the time interval of simulation) is plotted in Figure 6.1.

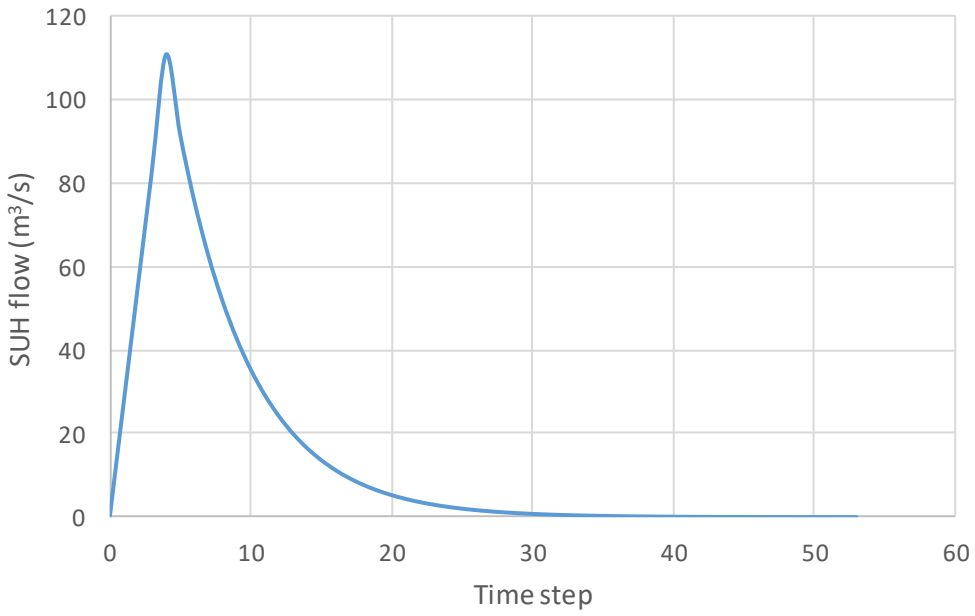

Figure 6.1. Sarantapotamos parametric synthetic unit hydrograph for d = 0.5 h.

6.5 Model calibration

6.5.1 Model A

The simulated streamflow is calibrated against the observed streamflow at Gyra Stefanis by optimizing the point rainfall at X-station and also by taking into consideration two key assumptions:

- Fitting the simulated streamflow to the observed flow data until November 15th 9:00 am (see Figure 4.1).
- Generation of peak flows larger than the flow capacity of the culvert (~100 m^3/s) during the morning hours of November 15th (thus taking advantage of the known overflow of the bridge, which is key qualitative information based on audiovisual evidence).

To quantify these assumptions, functions *error1* and *penalty* are introduced:

- *error1*: equals the sum square of the difference between the simulated streamflow, Q_{sim}, and the observed streamflow, Q_{obs}, for each time step, t_i, using eq. (6.2), thus accommodating the first assumption.

$$error1(t_i) = [Q_{sim}(t_i) - Q_{obs}(t_i)]^2 \quad (6.2)$$

- *penalty*: constrains the peak flow between 110 and 200 m^3/s by creating a penalty if the peak flow does not meet these aforementioned boundaries, thus accommodating the second assumption and at the same time restricting the model from producing an unrealistic peak flow. The function is given by eq. (6.3):

$$penalty = \begin{cases} (Q_{sim,max} - 200)^2, Q_{sim} > 200\ m^3/s \\ (Q_{sim,max} - 110)^2, Q_{sim} < 110\ m^3/s \end{cases} \quad (6.3)$$

The model calibration is then formulated as an optimization procedure, by introducing the objective function *f*, given by eq. (6.4). The optimized solution is the rainfall at X-station, *XRain*, for which function *f* is minimized.

$$f = \lambda_1 * average(error1) + \lambda_2 * penalty \quad (6.4)$$

where λ_1 and λ_2 are weighting coefficients equal to 1 and 0.01, respectively.

The optimization is performed using the Microsoft Excel Evolutionary Solver. The resulting solution is the rainfall at the hypothetical X-station from November 14th 09:00 am to November 15th 09:00 am in 30-min intervals (48 rainfall values).

6.5.2 Model B-I

Model B-I is calibrated using the same assumptions as Model A and therefore, these assumptions are quantified by functions *error1* and *penalty*, as they are presented in paragraph 6.5.1. Function *error2* is also introduced to the optimization procedure, as described below:

- *error2*: equals the sum square of the difference between the simulated streamflow, Q_{sim}, and the observed streamflow, Q_{obs}, for the time steps, t_i, between November 14th 06:00 pm and November 14th 10:30 pm and is given by eq. (6.5). The purpose of *error2* is to ensure the simulation of the small flood event during the evening hours of November 14th.

$$error2(t_i) = [Q_{sim}(t_i) - Q_{obs}(t_i)]^2 \quad (6.5)$$

Taking this into consideration, the objective function *f* is now given by eq. (6.6):

$$f = \lambda_1 * average(error1) + \lambda_2 * penalty + \lambda_3 * average(error2) \quad (6.6)$$

where λ_1, λ_2 and λ_3 are weighting coefficients equal to 1, 0.01 and 10, respectively.

The optimization is performed using the Matlab Genetic Algorithm and the resulting solution is the rainfall at the hypothetical X-station (*XRain*) from November 14th 09:00 am to November 15th 09:00 am, in 30-min intervals (48 rainfall values).

6.5.3 Model B-II

Model B-II uses the same assumptions and calibration functions as Model B-I, but also takes advantage of CCTV footage from the culvert at Gyra Stefanis (Picture 6.1) and makes the following assumptions:

- The flow at November 15th 11:00 am is estimated to be 120 m^3/s.
- The flow at November 15th 01:00 pm is estimated to be 80 m^3/s.

Thus, two extra time steps are added to the *error1* function, corresponding to the time steps described above. The other calibration functions (*penalty* and *error2*) remain the same, as they were presented in paragraphs 6.5.1 and 6.5.3.

Picture 6.1. CCTV footage of the culvert during the flood

The optimization is performed again using the Matlab Genetic Algorithm. However, two extra time steps are added to the rainfall at the hypothetical X-station in order to account for the two aforementioned assumptions, thus the resulting solution is the rainfall at the hypothetical X-station from November 14th 09:00 am to November 15th 10:00 am in 30-min intervals (50 values).

6.6 Probabilistic analysis

A probabilistic analysis is performed on the resulting rainfall at the hypothetical station X. Since idf curves at this specific point do not exist, the return period of each rainfall set was estimated using the idf curve from the station in Mandra. Its analytical expression is presented in eq. (6.7)

$$i = 213.4\ (T^{0.125} - 0.641)/(1 + d/0.124)^{0.622} \quad (6.7)$$

where *i is* the rainfall intensity in mm/h, *d* is the time scale *(*duration) in hours and *T is* the return period (years). The above expression was extracted within the recent implementation of the EU Flood Directive in the River Basin District of Attica, and is available in the web site of the Special Secretariat of Water (http://floods.ypeka.gr).

The analysis is performed for 10 temporal scales presented in Table 6.1:

Table 6.1. Temporal scales for probabilistic analysis

d (h)	0.5	1	2	3	4	5	6	12	18	24

7. Scenario-based approach

7.1 Model A

Five different parameter sets are examined using Model A. Each scenario and the corresponding parameter values are presented in Table 7.1. Within the optimization procedure, at each time step, the rainfall values at *X*-station are constrained between 0 and 30 mm.

Table 7.1. Hydrological scenarios and parameter sets for Model A

Hydrological scenario	S1-A	S2-A	S3-A	S4-A	S5-A
Initial abstraction ratio, a	0.10	0.10	0.05	0.05	0.12
AMC coefficient, AMC_{coef}	0.70	0.30	0.30	0.70	0.40
Recession parameter, k (h^{-1})	0.20	0.20	0.40	0.15	0.30
Lag time, τ (h)	2.0	2.0	2.0	1.0	1.0

The simulated hydrographs, as well as the simulated rainfall at the hypothetical X-station for each scenario, are shown in Figures 7.1 to 7.5. The resulting initial abstraction, h_0, curve number, *CN*, and maximum potential retention, *S*, are presented in Table 7.2 and the results of the probabilistic analysis in terms of estimated return period and simulated rainfall intensity for each scenario are plotted in Figure 7.6 and Figure 7.7, respectively.

Table 7.2. Initial abstraction, curve number and maximum potential retention for each scenario using Model A

Hydrological scenario	S1-A	S2-A	S3-A	S4-A	S5-A
Initial abstraction, h_0 (mm)	26.6	63.8	48.5	17.3	56.7
Curve number, *CN*	58	38	38	58	43
Maximum potential retention, *S* (mm)	265.8	638.0	970.4	347.0	472.3

All scenarios conclude that the storm event at X-station comprised two distinct clusters, one lasting from the morning to the afternoon of November 14th, and a short yet very intense storm cluster occurring in the morning hours of November 15th. Specifically:

Scenario S1-A: The first cluster is from November 14th 9:00 am until November 14th 5:30 pm with a total accumulated rainfall of 40.1 mm and the second is from November 15th 6:00 am until November 15th 9:00 am with a total accumulated rainfall of 54.8 mm. The simulated peak flow is 110 m^3/s (Figure 7.1).

Scenario S2-A: The first cluster is from November 14th 9:00 am until November 14th 6:30 pm with a total accumulated rainfall of 98.1 mm and the second is from November 15th 6:01 am until November 15th 9:00 am with a total accumulated rainfall of 95.4 mm. The simulated peak flow is 135 m^3/s (Figure 7.2).

Scenario S3-A: The first cluster is from November 14th 9:00 am until November 15th 9:00 pm with a total accumulated rainfall of 82.1 mm and the second is from November 15th 6:01 am until

November 15th 9:00 am with a total accumulated rainfall of 88.3 mm. The simulated peak flow is 127 m^3/s (Figure 7.3).

Scenario S4-A: The first cluster is from November 14th 9:00 am until November 15th 6:30 pm with a total accumulated rainfall of 33.7 mm and the second is from November 15th 7:01 am until November 15th 9:00 am with a total accumulated rainfall of 66.8 mm. The simulated peak flow is 113 m^3/s (Figure 7.4).

Scenario S5-A: The first cluster is from November 14th 9:00 am until November 15th 7:30 pm with a total accumulated rainfall of 84.0 mm and the second is from November 15th 7:01 am until November 15th 9:00 am with a total accumulated rainfall of 59.0 mm. The simulated peak flow is 131 m^3/s (Figure 7.5).

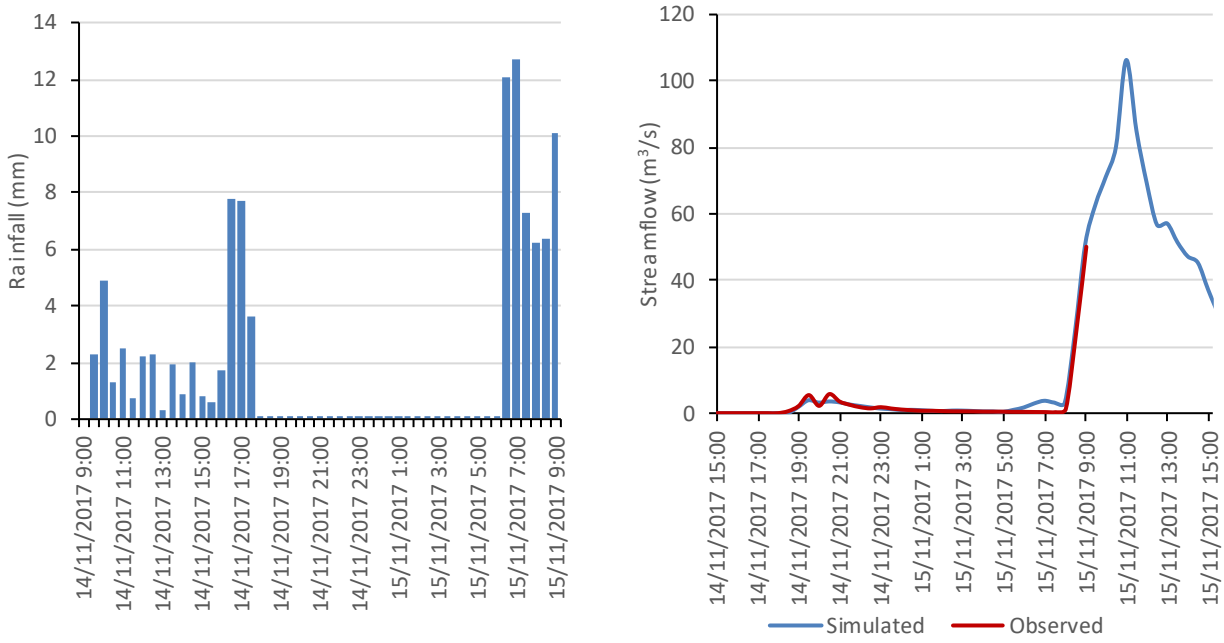

Figure 7.1. Simulated X-Station 30-min rainfall (left) and streamflow at Gyra Stefanis (right) for scenario S1-A

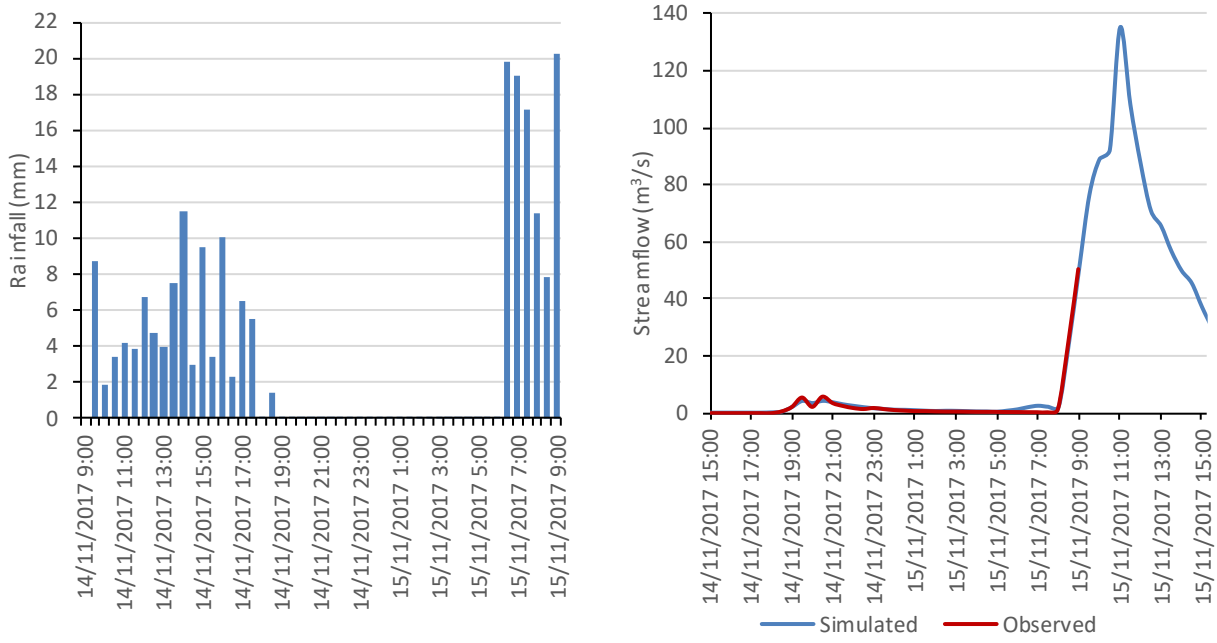

Figure 7.2. Simulated X-Station 30-min rainfall (left) and streamflow at Gyra Stefanis (right) for scenario S2-A

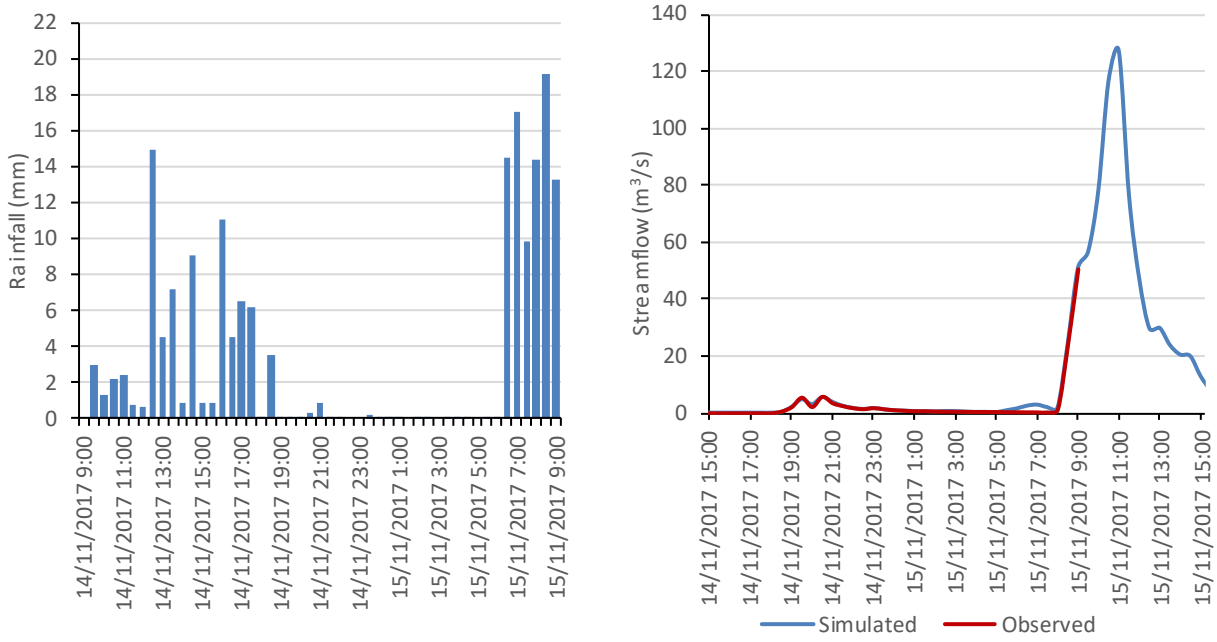

Figure 7.3. Simulated X-Station 30-min rainfall (left) and streamflow at Gyra Stefanis (right) for scenario S3-A

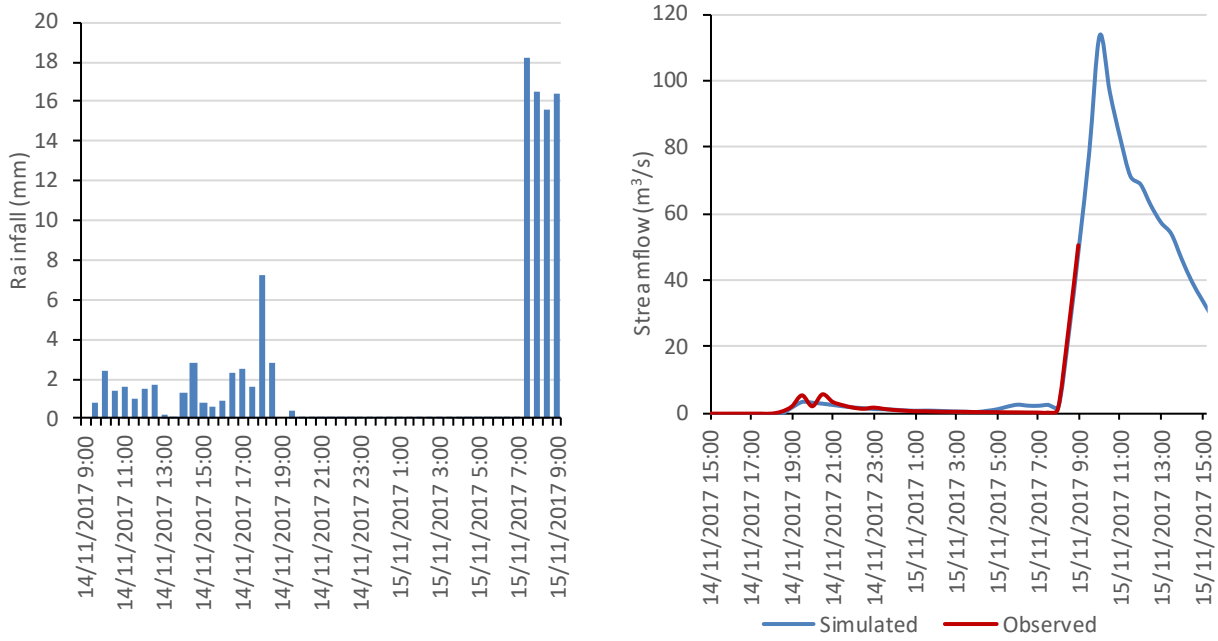

Figure 7.4. Simulated X-Station 30-min rainfall (left) and streamflow at Gyra Stefanis (right) for scenario S4-A

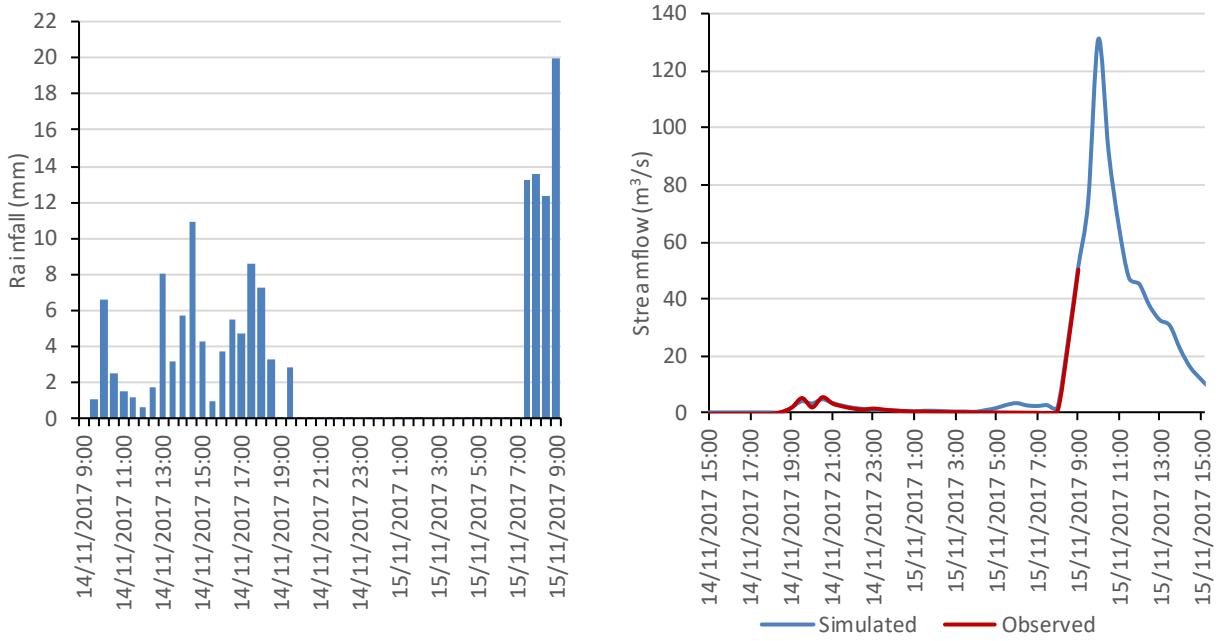

Figure 7.5. Simulated X-Station 30-min rainfall (left) and streamflow at Gyra Stefanis (right) for scenario S5-A

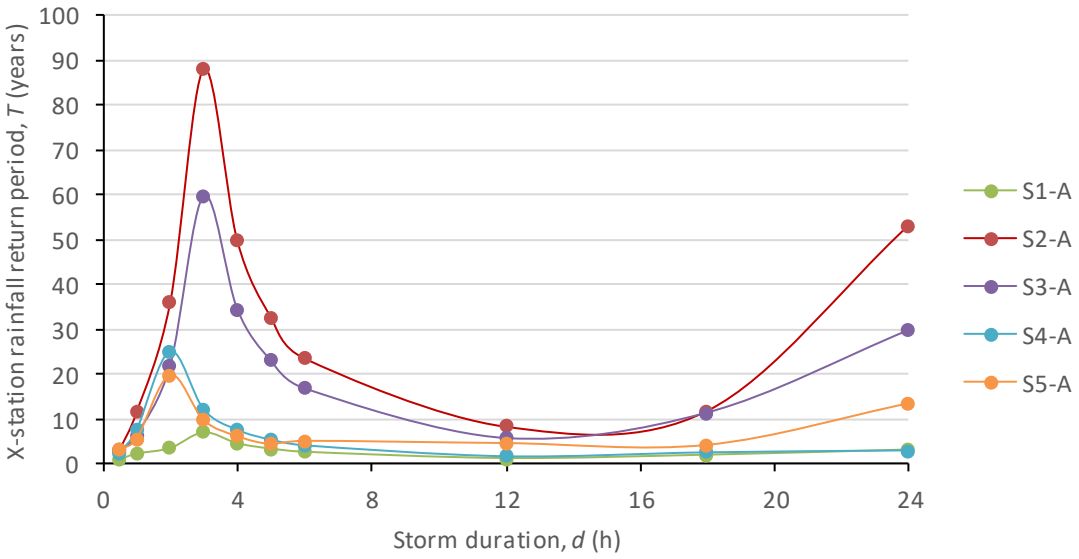

Figure 7.6. Estimated return period vs time scale (duration) for the five hydrological scenarios using Model A

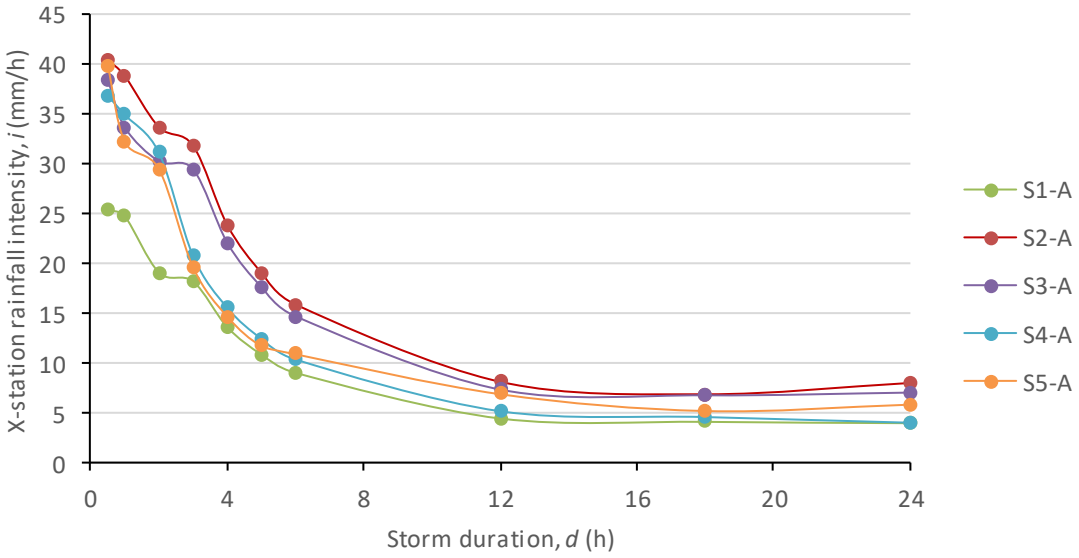

Figure 7.7. X-station simulated rainfall intensity vs time scale (duration) for the five hydrological scenarios using Model A

7.2 Model B-I

Five different parameter sets are examined using Model B-I and the corresponding parameter values for each scenario are presented in Table 7.3. Within the optimization procedure, at each time step, the rainfall values at X-station are constrained between 0 and 100 mm. This

corresponds to a maximum 30-min intensity of 200 mm/h, which is extremely high, so it can practically be considered as unconstrained.

Table 7.3. Hydrological scenarios and parameter sets for Model B-I

Hydrological scenario	S1-B-I	S2-B-I	S3-B-I	S4-B-I	S5-B-I
Initial abstraction ratio, a	0.10	0.05	0.12	0.10	0.05
AMC coefficient, AMC_{coef}	0.30	0.40	0.50	0.60	0.70

The simulated hydrographs, as well as the simulated rainfall at the hypothetical X-station for each scenario, are shown in Figures 7.8 to 7.12. The resulting initial abstraction, h_0, curve number, *CN*, and maximum potential retention, *S*, are presented in Table 7.4 and the results of the probabilistic analysis in terms of estimated return period and simulated rainfall intensity for each scenario are plotted in Figure 7.13 and Figure 7.14, respectively.

Table 7.4. Initial abstraction, curve number and maximum potential retention for each scenario using Model B-II

Hydrological scenario	S1-B-I	S2-B-I	S3-B-I	S4-B-I	S5-B-I
Initial abstraction, h_0 (mm)	63.2	35.7	9.4	32.6	16.7
Curve number, *CN*	38	43	48	53	58
Maximum potential retention, *S* (mm)	632.3	714.7	786.1	325.5	334.5

All scenarios conclude that the storm event at X-station comprised of two distinct clusters, one lasting from the morning to the afternoon of November 14th (which in some cases could be divided in two separate sub-clusters), and a short yet very intense storm cluster occurring in the morning hours of November 15th. More specifically:

Scenario S1-B-I: The first cluster is from November 14th 10:30 am until November 15th 7:00 pm with a total accumulated rainfall of 96.8 mm and the second is from November 15th 7:00 am until November 15th 9:00 am with a total accumulated rainfall of 101.9 mm. The simulated peak flow is 147 m^3/s (Figure *7.8*).

Scenario S2-B-I: The first cluster is from November 14th 2:30 pm until November 15th 7:00 pm with a total accumulated rainfall of 95.3 mm and the second is from November 15th 7:30 am until November 15th 9:00 am with a total accumulated rainfall of 94.5 mm. The simulated peak flow is 114 m^3/s (Figure 7.9).

Scenario S3-B-I: The first cluster is from November 14th 11:30 am until November 15th 12:00 pm with a total accumulated rainfall of 20.4 mm, the second is from November 15th 5:30 pm until November 15th 7:00 pm with a total accumulated rainfall of 14.5 mm and the third is from November 15th 6:30 am until November 15th 9:00 am with a total accumulated rainfall of 106.5 mm. The simulated peak flow is 133 m^3/s (Figure 7.10).

Scenario S4-B-I: The first cluster is from November 14th 4:30 pm until November 15th 7:00 pm with a total accumulated rainfall of 51.5 mm and the second is from November 15th 7:00 am until

November 15th 9:00 am with a total accumulated rainfall of 71.0 mm. The simulated peak flow is 136 m^3/s (Figure 7.11).

Scenario S5-B-I: The first cluster is from November 14th 9:00 am until November 15th 7:30 pm with a total accumulated rainfall of 35.5 mm and the second is from November 15th 6:30 am until November 15th 9:00 am with a total accumulated rainfall of 75.9 mm. The simulated peak flow is 150 m^3/s (Figure 7.12).

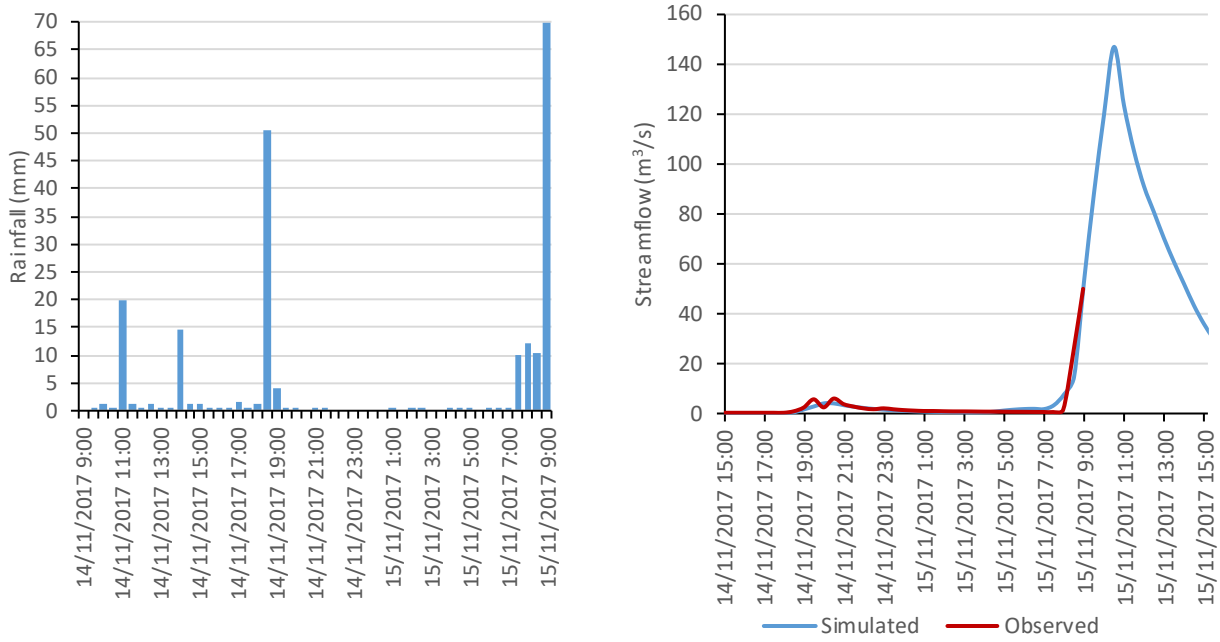

Figure 7.8. Simulated X-Station 30-min rainfall (left) and streamflow at Gyra Stefanis (right) for scenario S1-B-I

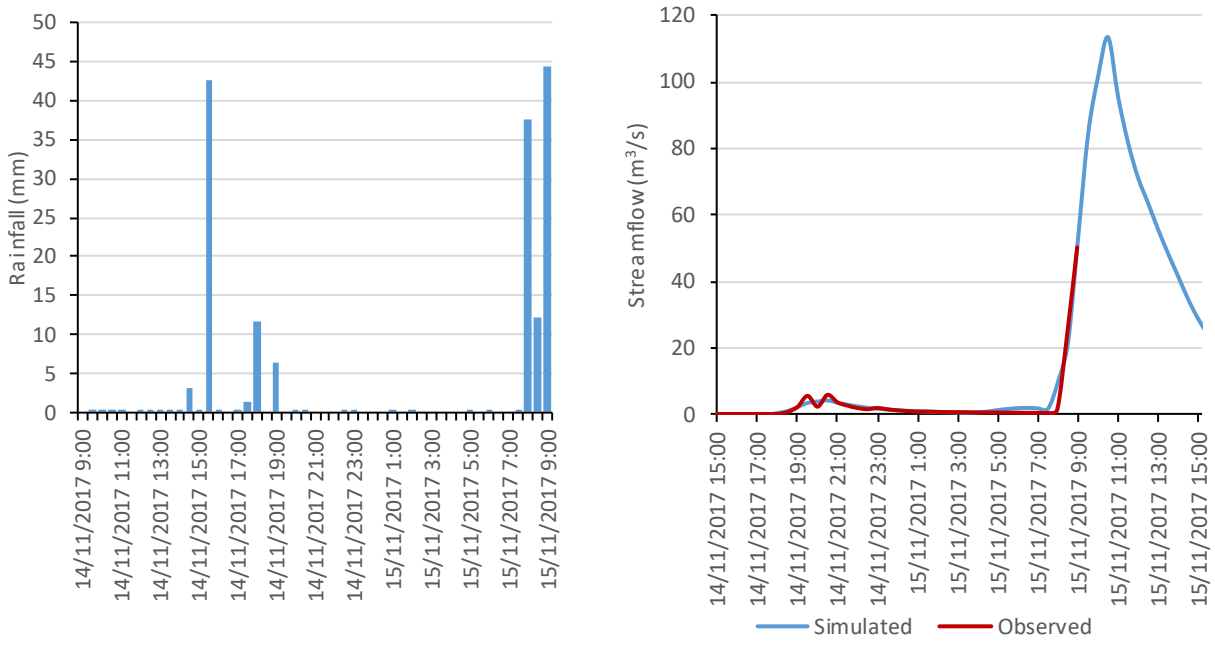

Figure 7.9. Simulated X-Station 30-min rainfall (left) and streamflow at Gyra Stefanis (right) for scenario S2-B-I

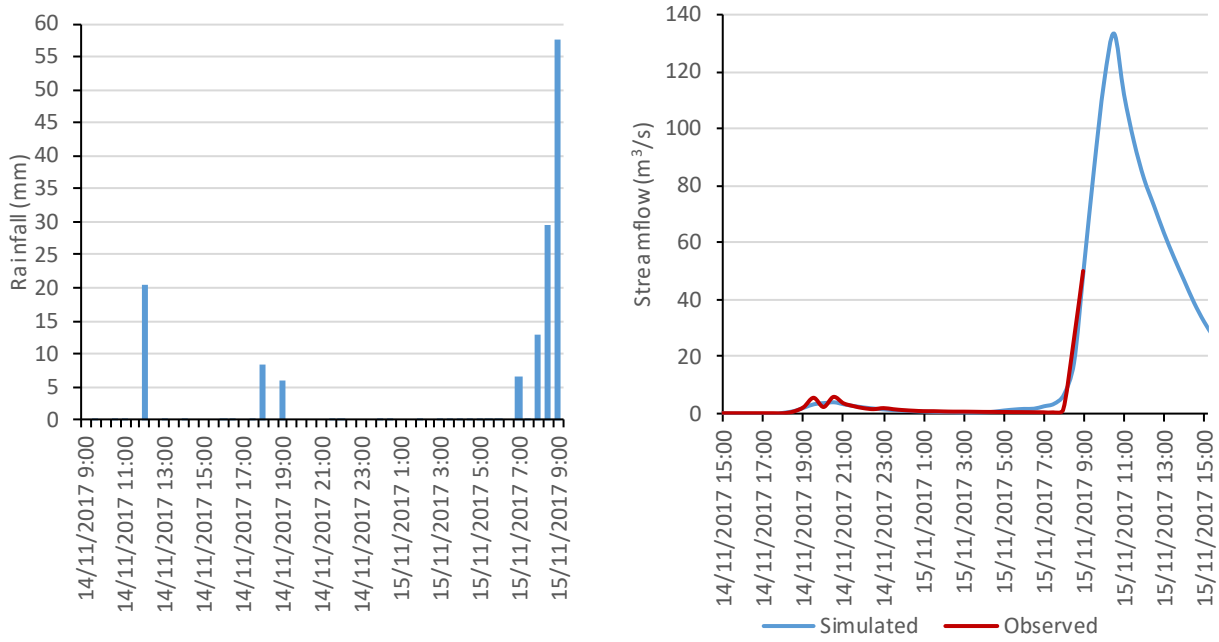

Figure 7.10. Simulated X-Station 30-min rainfall (left) and streamflow at Gyra Stefanis (right) for scenario S3-B-I

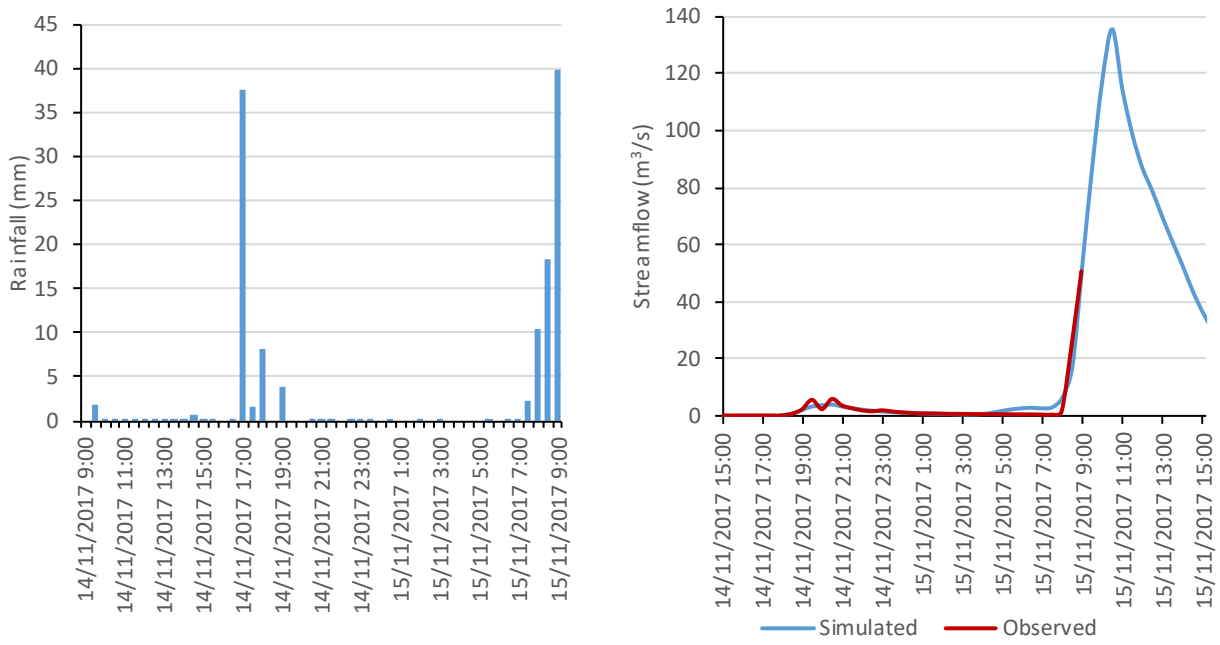

Figure 7.11. Simulated X-Station 30-min rainfall (left) and streamflow at Gyra Stefanis (right) for scenario S4-B-I

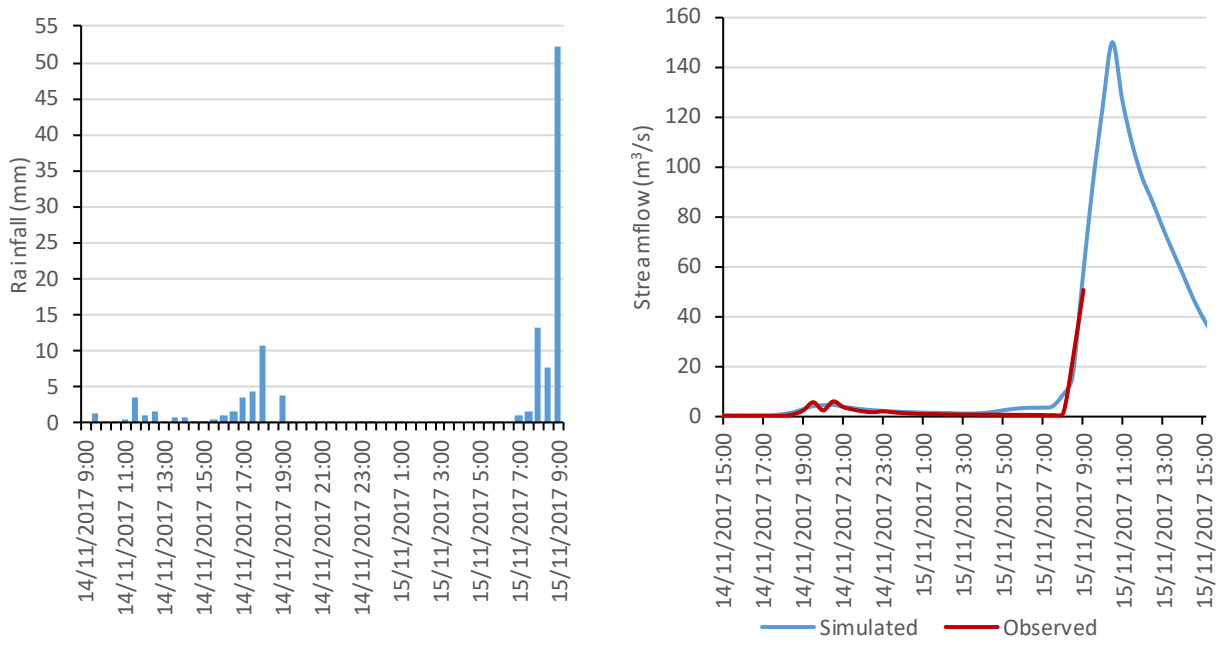

Figure 7.12. Simulated X-Station 30-min rainfall (left) and streamflow at Gyra Stefanis (right) for scenario S5-B-I

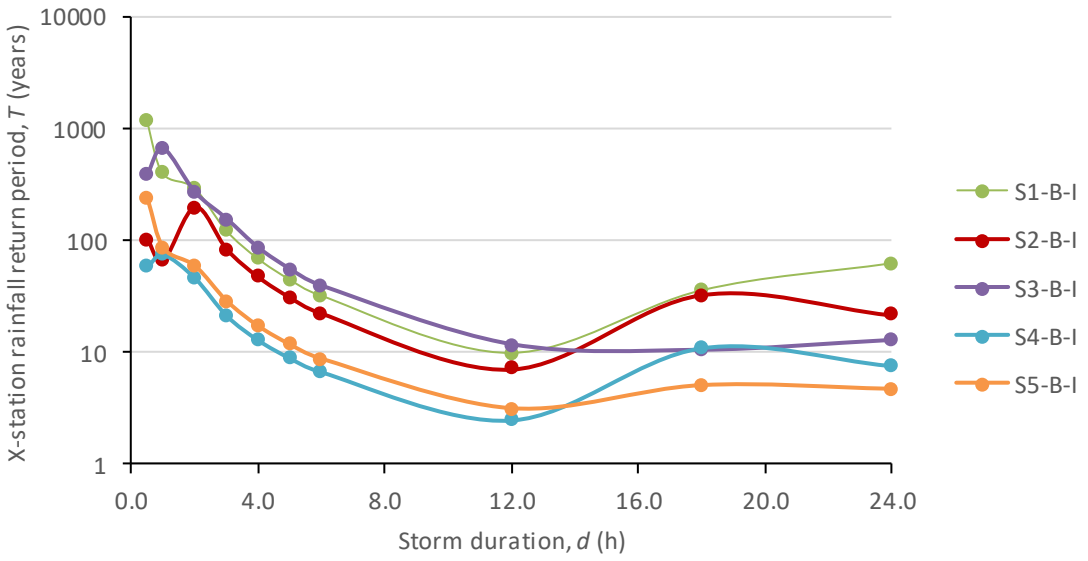

Figure 7.13. Estimated return period vs time scale (duration) for the five hydrological scenarios using Model B-I

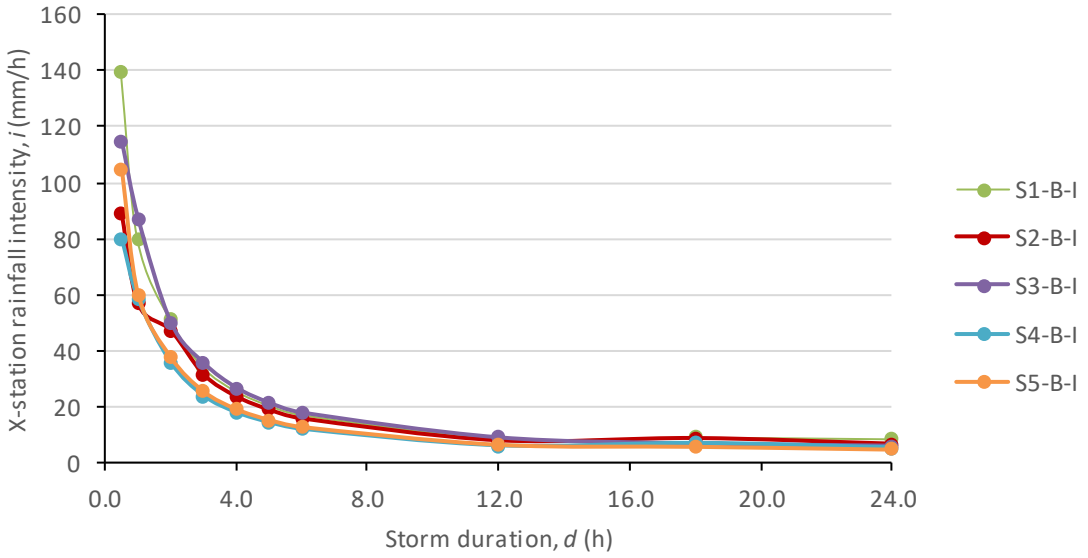

Figure 7.14. X-station simulated rainfall intensity vs time scale (duration) for the five hydrological scenarios using Model B-I

7.3 Model B-II

Five different parameter sets are examined using Model B-II. Each scenario and the corresponding parameter values are presented in Table 7.5. Within the optimization procedure, at each time step, the rainfall values at X-station are constrained between 0 and 100 mm. This

corresponds to a maximum 30-min intensity of 200 mm/h, so it can practically be considered as unconstrained.

Table 7.5. Hydrological scenarios and parameter sets for Model B-II

Hydrological scenario	S1-B-II	S2-B-II	S3-B-II	S4-B-II	S5-B-II
Initial abstraction ratio, a	0.10	0.05	0.12	0.10	0.05
AMC coefficient, AMC_{coef}	0.30	0.40	0.50	0.60	0.70

The simulated rainfall at the hypothetical X-Station, as well as simulated hydrographs for each scenario are shown in Figures 7.15 to 7.19. The resulting initial abstraction, h_0, curve number, *CN*, and maximum potential retention, *S*, are presented in Table 7.6 and the results of the probabilistic analysis in terms of estimated return period and simulated rainfall intensity for each scenario are plotted in Figure 7.20 and Figure 7.21, respectively.

Table 7.6. Initial abstraction, curve number and maximum potential retention for each scenario using Model B-II

Hydrological scenario	S1-B-II	S2-B-II	S3-B-II	S4-B-II	S5-B-II
Initial abstraction, h_0 (mm)	64.3	35.6	9.3	32.4	16.8
Curve number, *CN*	38	43	48	53	58
Maximum potential retention, *S* (mm)	643.1	712.9	773.4	324.0	335.4

All scenarios conclude that the storm event at X-station comprised two distinct clusters, one lasting from the morning to the afternoon of November 14th (which in some cases could be divided in two separate sub-clusters), and a short yet very intense storm cluster occurring in the morning hours of November 15th. Specifically:

Scenario S1-B-II: The first cluster is from November 14th 11:30 am until November 15th 3:00 pm with a total accumulated rainfall of 76.1 mm and the second is from November 15th 7:31 am until November 15th 10:00 am with a total accumulated rainfall of 100.1 mm. The simulated peak flow is 110 m^3/s (Figure 7.15).

Scenario S2-B-II: The first cluster is from November 14th 11:00 am until November 15th 11:30 am with a total accumulated rainfall of 26.1 mm, the second is from November 15th 4:30 pm until November 15th 7:00 pm with a total accumulated rainfall of 35.8 mm and the third is from November 15th 7:00 am until November 15th 10:00 am with a total accumulated rainfall of 109.2 mm. The simulated peak flow is 117 m^3/s (Figure 7.16).

Scenario S3-B-II: The first cluster is from November 14th 2:00 pm until November 15th 2:30 pm with a total accumulated rainfall of 17.1 mm, the second is from November 15th 5:00 pm until November 15th 7:00 pm with a total accumulated rainfall of 16.6 mm and the third is from November 15th 6:30 am until November 15th 10:00 am with a total accumulated rainfall of 110.3 mm. The simulated peak flow is 126 m^3/s (Figure 7.17).

Scenario S4-B-II: The first cluster is from November 14th 9:00 am until November 15th 7:00 pm with a total accumulated rainfall of 53.9 mm and the second is from November 15th 7:00 am until

November 15th 10:00 am with a total accumulated rainfall of 74.0 mm. The simulated peak flow is 139 m^3/s (Figure 7.18).

Scenario S5-B-II: The first cluster is from November 14th 1:30 pm until November 15th 2:30 pm with a total accumulated rainfall of 21.0 mm, the second is from November 15th 5:30 pm until November 15th 7:00 pm with a total accumulated rainfall of 12.0 mm and the third is from November 15th 7:00 am until November 15th 10:00 am with a total accumulated rainfall of 74.9 mm. The simulated peak flow is 133 m^3/s (Figure 7.19).

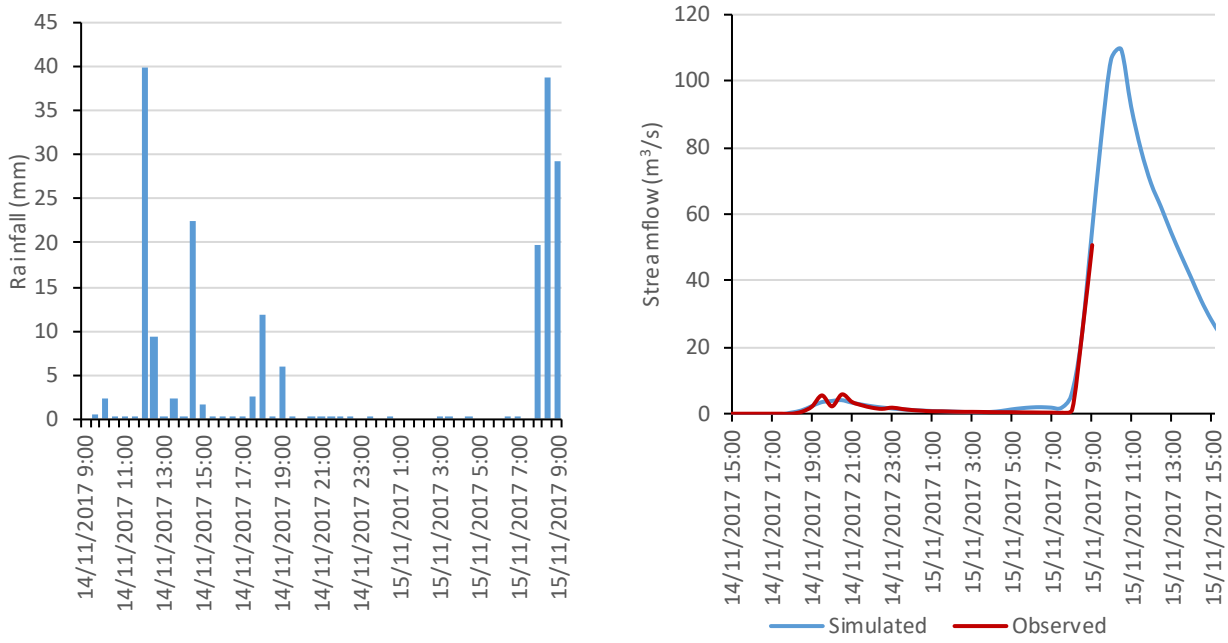

Figure 7.15. Simulated X-Station 30-min rainfall (left) and streamflow at Gyra Stefanis (right) for scenario S1-B-II

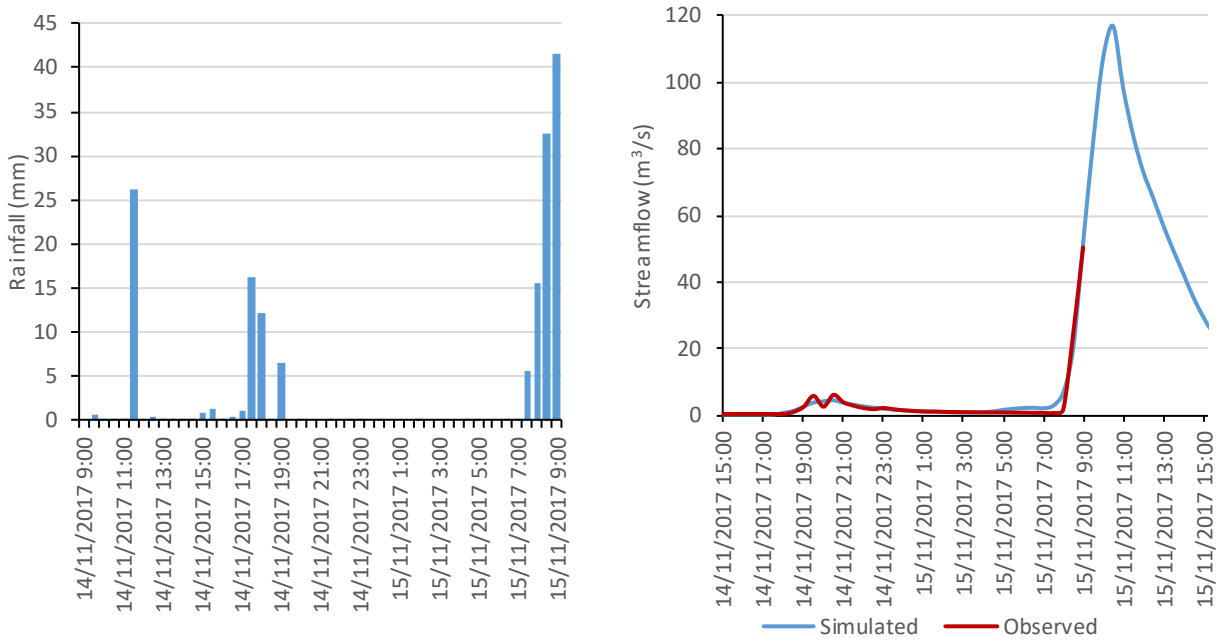

Figure 7.16. Simulated X-Station 30-min rainfall (left) and streamflow at Gyra Stefanis (right) for scenario S2-B-II

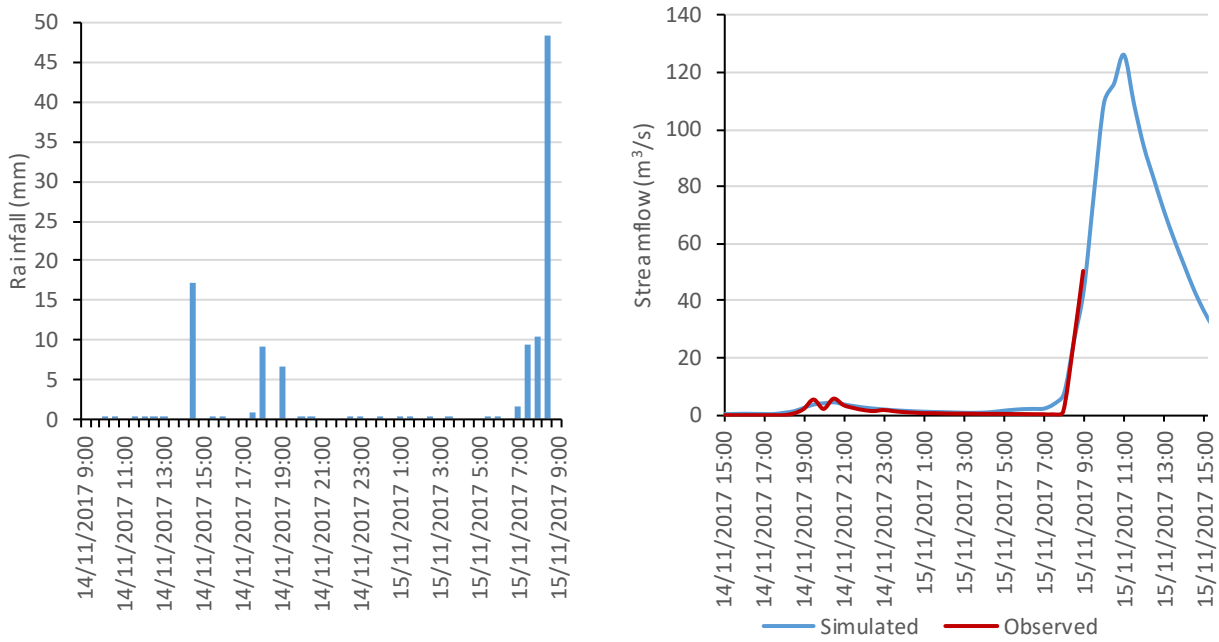

Figure 7.17. Simulated X-Station 30-min rainfall (left) and streamflow at Gyra Stefanis (right) for scenario S3-B-II

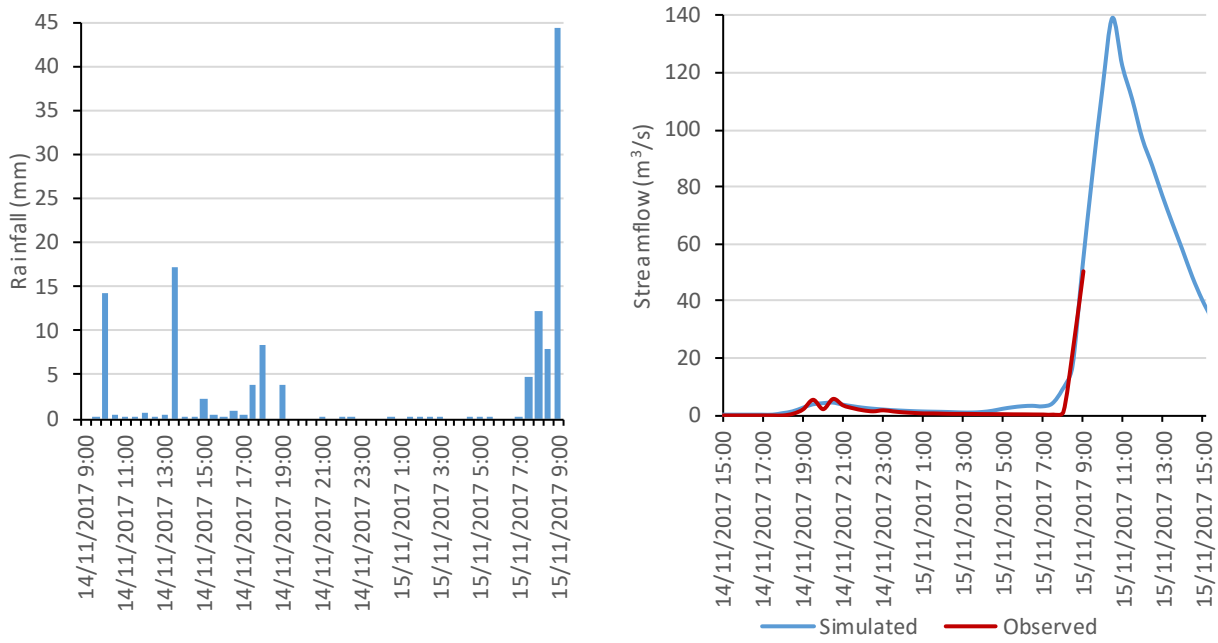

Figure 7.18. Simulated X-Station 30-min rainfall (left) and streamflow at Gyra Stefanis (right) for scenario S4-B-II

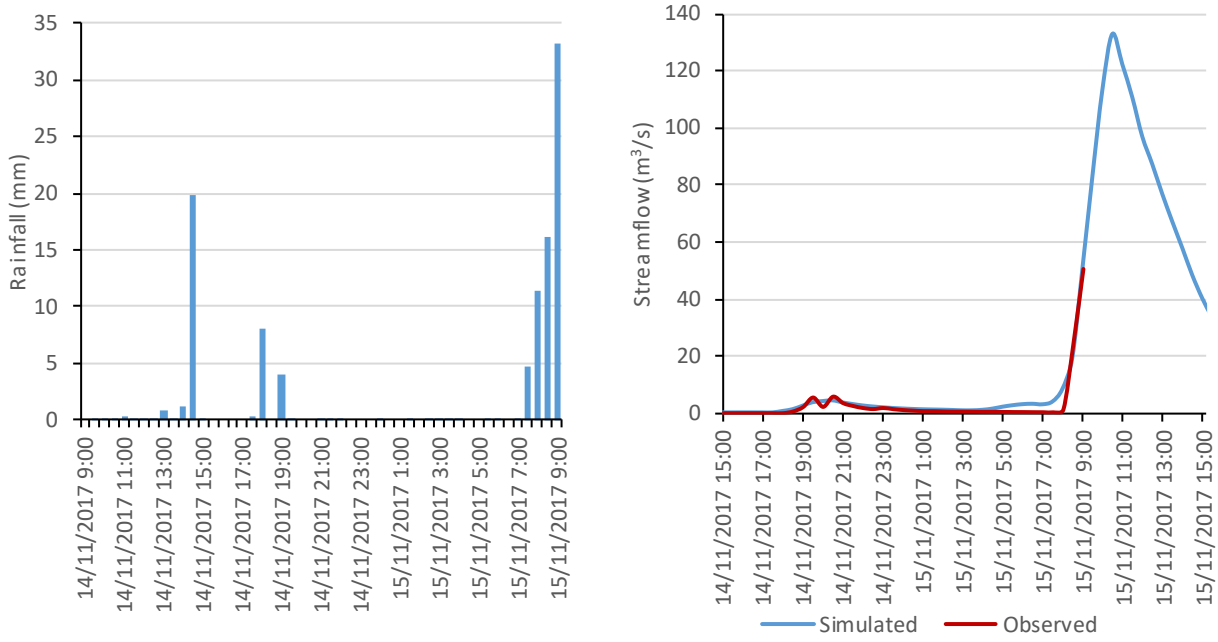

Figure 7.19. Simulated X-Station 30-min rainfall (left) and streamflow at Gyra Stefanis (right) for scenario S5-B-II

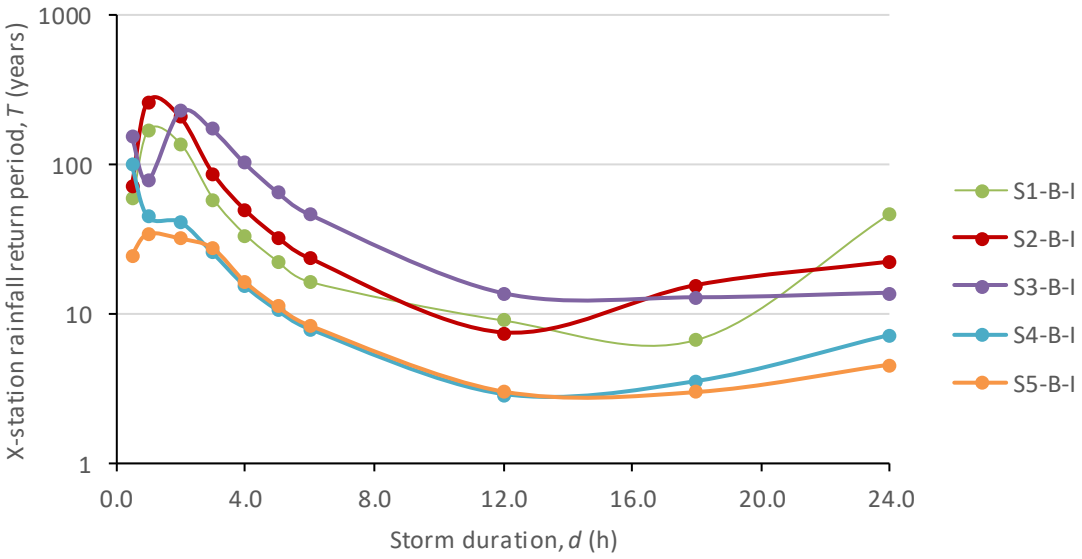

Figure 7.20. Estimated return period vs time scale (duration) for the five hydrological scenarios using model B-II

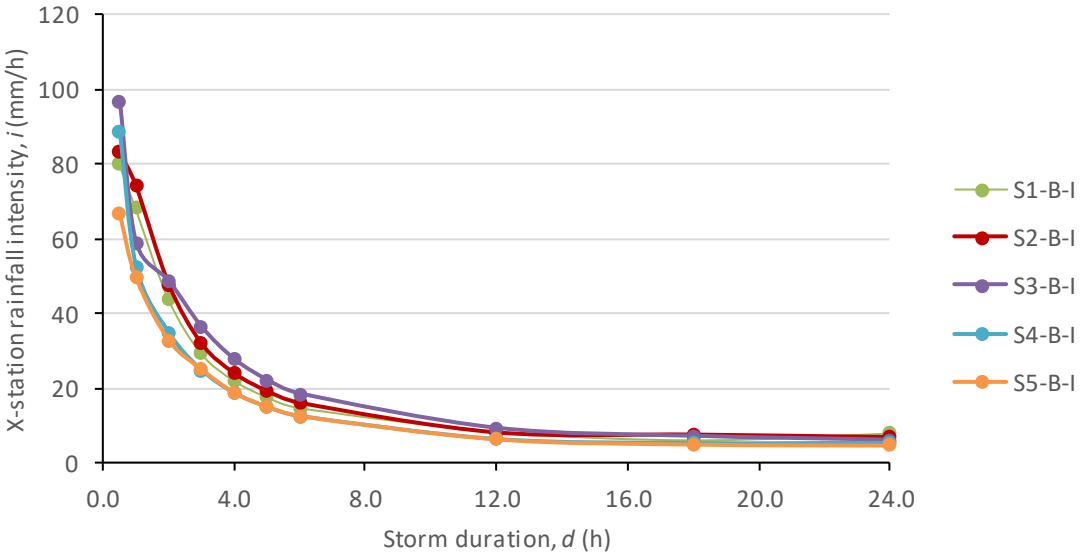

Figure 7.21. X-station simulated rainfall intensity vs time scale (duration) for the five hydrological scenarios using model B-II

7.4 Discussion

The simulated total rainfall and maximum 30-min rainfall at the hypothetical X-station for each of the aforementioned scenarios, as well as the simulated peak flow at Gyra Stefanis are presented in Table 7.7:

Table 7.7. Total and maximum simulated rainfall at X-station and simulated peak flow at Gyra Stefanis for each hydrological scenario

Scenario	Total rainfall (mm)	Maximum rainfall (mm)	Peak flow (m^3/s)
S1-A	94.9	12.7	110
S2-A	193.5	20.2	135
S3-A	170.4	19.2	127
S4-A	100.5	18.2	113
S5-A	143.0	19.9	131
S1-B-I	198.7	69.8	147
S2-B-I	189.8	44.5	114
S3-B-I	141.4	57.5	133
S4-B-I	122.5	39.9	136
S5-B-I	111.4	52.3	150
S1-B-II	176.2	40.0	110
S2-B-II	171.1	41.5	117
S3-B-II	144.0	48.3	126
S4-B-II	127.9	44.4	139
S5-B-II	95.9	33.3	133

The estimated return period and simulated rainfall intensity for each of the aforementioned scenarios are presented in Table 7.8 and Table 7.9:

Table 7.8. Estimated return period vs time scale (duration) for each hydrological scenario

Scenario	Time scale (duration), *d* (h)									
	0.5	1.0	2.0	3.0	4.0	5.0	6.0	12.0	18.0	24.0
	Return period, *T* (years)									
S1-A	1	2	3	7	5	3	3	1	2	3
S2-A	3	12	36	88	50	33	24	8	12	53
S3-A	3	6	22	60	34	23	17	6	11	30
S4-A	2	8	25	12	8	5	4	2	2	3
S5-A	3	5	20	10	6	4	5	5	4	13
S1-B-I	1207	406	298	124	69	45	32	10	36	63
S2-B-I	101	66	198	84	47	31	22	7	33	22
S3-B-I	397	656	268	155	86	55	39	12	10	13
S4-B-I	59	75	46	21	13	9	7	2	11	8
S5-B-I	237	87	60	29	17	12	9	3	5	5
S1-B-II	59	170	135	58	34	22	16	9	7	46
S2-B-II	71	265	207	87	49	32	23	7	15	22
S3-B-II	155	79	229	172	103	66	46	14	13	14
S4-B-II	100	45	42	26	15	11	8	3	4	7
S5-B-II	25	34	32	27	16	11	8	3	3	5

Table 7.9. Simulated rainfall intensity at X-station vs time scale (duration) for each hydrological scenario

Scenario	Time scale (duration), *d* (h)									
	0.5	1.0	2.0	3.0	4.0	5.0	6.0	12.0	18.0	24.0
	Rainfall intensity, *i* (mm/h)									
S1-A	25.4	24.8	19.2	18.3	13.7	11.0	9.1	4.6	4.2	4.1
S2-A	40.4	38.8	33.7	31.8	23.9	19.1	15.9	8.2	6.9	8.1
S3-A	38.4	33.6	30.2	29.4	22.1	17.7	14.8	7.4	6.9	7.1
S4-A	36.9	35.0	31.2	20.8	15.6	12.5	10.4	5.2	4.6	4.0
S5-A	39.9	32.3	29.5	19.7	14.8	11.8	11.0	7.0	5.3	6.0
S1-B-I	139.6	80.0	51.0	34.0	25.5	20.4	17.0	8.5	8.9	8.3
S2-B-I	89.0	56.8	47.2	31.5	23.6	18.9	15.7	7.9	8.7	6.7
S3-B-I	114.9	87.1	50.0	35.5	26.6	21.3	17.7	8.9	6.7	5.9
S4-B-I	79.8	58.2	35.5	23.7	17.8	14.2	11.8	5.9	6.8	5.2
S5-B-I	104.7	59.9	37.4	25.3	19.0	15.2	12.6	6.3	5.6	4.6
S1-B-II	80.0	68.2	44.0	29.3	22.0	17.6	14.7	8.3	6.0	7.8
S2-B-II	83.1	74.1	47.6	31.8	23.8	19.1	15.9	7.9	7.4	6.7
S3-B-II	96.7	58.8	48.5	36.2	27.6	22.1	18.4	9.2	7.1	6.0
S4-B-II	88.9	52.5	34.7	24.7	18.5	14.8	12.3	6.2	5.1	5.1
S5-B-II	66.5	49.5	32.8	25.0	18.7	15.0	12.5	6.2	4.9	4.6

All scenarios ensure perfect fitting to the observed flows of Sarantapotamos until 9:00 am, despite their significant differences in rainfall estimations, in terms of intensities and temporal evolution, as well as peak flow estimations.

Scenarios simulated using Model A result in almost identical estimations of the maximum rainfall at the X-station. However, Model A presents major variability in terms of total rainfall, rainfall evolution and peak flow estimation for small changes of the initial parameters. The same behavior is observed in terms of return period values, although the results are more consistent in terms of rainfall intensities. On the other hand, Scenario S1-A, results in smaller intensities over short durations and thus seems to be far from reality, given that due to the small size of the catchment, its response time is quite short, thus the maximum rainfall at such duration is the most critical.

The scenarios simulated using Models B-I and B-II make similar assumptions, thus these models can be compared to each other. Model B-II results in almost identical maximum rainfall estimations, which is not the case for Model B-I. It seems that Model B-II is more consistent in terms of peak flow estimations, resulting in larger peak flows for larger values of the AMC coefficient. The AMC coefficient also affects the total rainfall estimations for both models. Model B-II is also more consistent in terms of return period estimation and rainfall intensity than Model B-I. This can help understand the importance of the additional information provided by the two extra calibration points in Model B-II.

The conclusion of the aforementioned analysis is that no safe conclusion can be reached. The problem analysis seems to be sensitive to not only the model used, thus the overall approach and available information, but also to the sole parameter of the rainfall-runoff transformation (i.e., the initial abstraction ratio) and the initial conditions, expressed in terms of the AMC coefficient. An uncertainty assessment is consequently attempted through a Monte Carlo analysis presented in Chapter 8.

8. Monte Carlo simulation

8.1 General information

The models presented in the previous chapters depend on a number of parameters as the initial input, which highly affect the simulated quantities. The true nature of these parameters is inherently uncertain and, consequently, the estimation of these parameters is also a quite difficult and highly uncertain procedure. This drawback is usually overcome through the employment of Monte Carlo simulations.

Monte Carlo simulation is a stochastic approach based on computational algorithms that rely on repeated random sampling in order to obtain numerical results. The essential idea that this model has established is using randomness to accommodate for the inherent uncertainty of model parameters, thus probabilistically approaching the solution to a problem and defining its confidence intervals. The modern version of the Markov Chain Monte Carlo method was invented in the late 1940s by Stanislaw Ulam, while he was working on nuclear weapons projects at the Los Alamos National Laboratory. Being secret, the work of von Neumann and Ulam required a code name. A colleague of von Neumann and Ulam, Nicholas Metropolis, suggested using the name “Monte Carlo”, which refers to the Monte Carlo Casino in Monaco where Ulam's uncle would borrow money from relatives to gamble (Moustakis, 2017).

From the modeling schemes presented in this study, Models B-I and B-II require a set of two initial parameters (α and AMC_{coef}) while Model A requires four (α, AMC_{coef}, k and τ). Furthermore, Models B-I and B-II are developed in the Matlab programming environment, thus making the repetitive process of the Montel Carlo simulation more convenient. Both these reasons led to the employment of Monte Carlo simulations against the initial abstraction ratio, α, and the antecedent moisture conditions coefficient, AMC_{coef}, only for Models B-I and B-II.

Furthermore, in the scenarios presented in Chapter 6, the maximum simulated rainfall at X-station was practically unconstrained. However, constraining this value within the optimization procedure forces the model to produce the same precipitation volume over a longer time period. The outcomes of this assumption are examined by employing two Monte Carlo simulations for each of the two models (B-I and B-II), one constraining the maximum rainfall and one with the maximum rainfall practically unconstrained.

8.2 Initial parameters

Efstratiadis *et al.* (2014) have represented a number of flood events in the study basin through the SCS-CN method, and concluded that the initial abstraction ratio, α, varied within a quite large range, as shown in Table 8.1. As the variability of this parameter is significant, within Monte Carlo simulations we employed a Log-Normal distribution for initial sampling, by assigning a mean value of 0.125 and standard deviation of 0.099.

Table 8.1. Initial abstraction ratio of past storm events (Efstratiadis et al., 2014)

Date	a
12/2011	0.019
02/2012	0.030
02/2012	0.029
02/2012	0.130
12/2012	0.045
01/2013	0.199
02/2013	0.190
11/2013	0.058
11/2013	0.218
12/2013	0.259
01/2014	0.280
03/2014	0.047
mean	0.125
st.dev	0.099

Furthermore, the 5-day accumulated point rainfall data at the neighboring stations before the storm event (Table 8.2) indicate that the antecedent moisture conditions were close to Type II. It is reminded that the SCS suggests Type II conditions when the accumulated rainfall of the past five days is between 13 and 38 mm for the dormant season. In this respect, within Monte Carlo simulations we considered that the AMC coefficient (AMC_{coef}) follows a Normal distribution with a mean value of 0.40 and standard deviation of 0.10 (we remind that a value of 0.50 represents the AMC Type II conditions).

Table 8.2. Daily accumulated rainfall observed at the stations in Madra and Vilia

Date	Mandra	Vilia
10/11/2017	-	0.0
11/11/2017	-	0.2
12/11/2017	-	0.4
13/11/2017	17.0	25.4
14/11/2017	11.8	10.2

8.3 Model B-I

8.3.1 Simulation MC1-B-I

MC1-B-I indicates a Monte Carlo simulation using Model B-I. The simulation is performed for 1000 sets of parameters a and AMC_{coef}, randomly chosen from the log-normal and normal distributions, respectively. Within the optimization procedure the simulated rainfall at X-station, at each time step, is constrained between 0 and 100 mm. This corresponds to a maximum 30-

min intensity of 200 mm/h, which is extremely high. From a practical point-of-view, the rainfall can be considered unconstrained.

The average simulated rainfall at X-station and its confidence intervals for 95%, 50% and 5% non-exceedance probability called P95, P50 and P5, respectively, are presented in Figure 8.1, while the average simulated streamflow at Gyra Stefanis and its corresponding confidence intervals can be seen in Figure 8.2. Figures 8.3 to 8.5 are scatter plots of the total simulated rainfall at X-station vs the antecedent moisture conditions coefficient, the initial abstraction and the maximum potential retention, respectively.

Regarding the probabilistic analysis, the average estimated return period with its confidence intervals for 95%, 50% and 5% non-exceedance probability are plotted in Figure 8.6. Similarly, the average rainfall intensity and its confidence intervals are plotted in Figure 8.7.

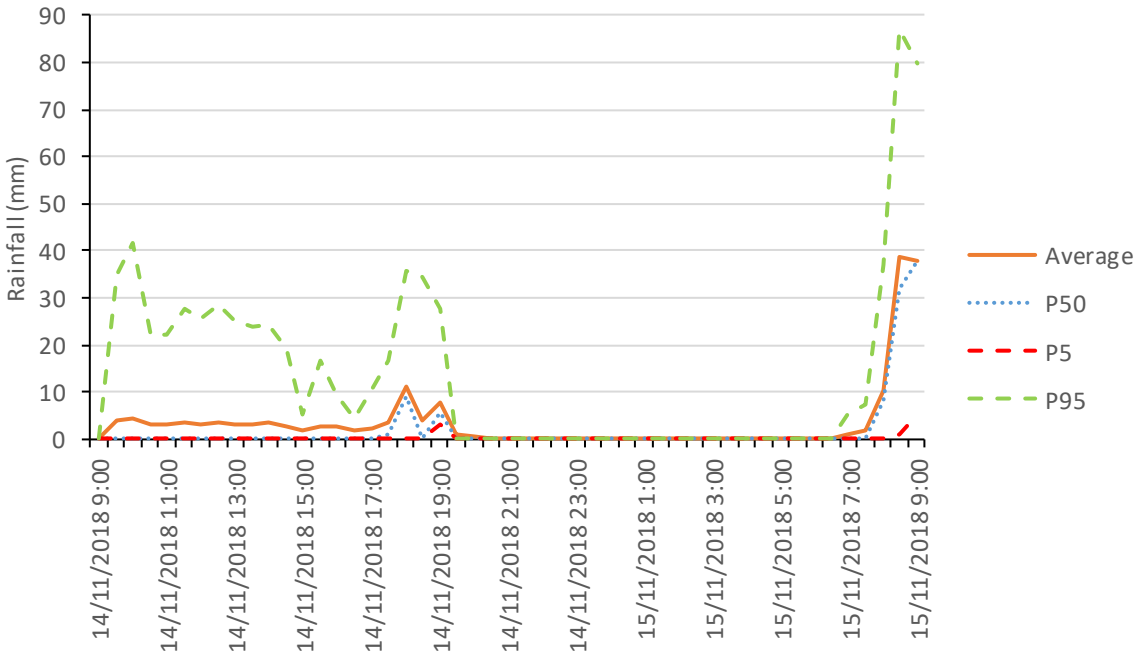

Figure 8.1. Average simulated rainfall at X-station and confidence intervals for 95%, 50% and 5% non-exceedance probability for simulation MC1-B-I

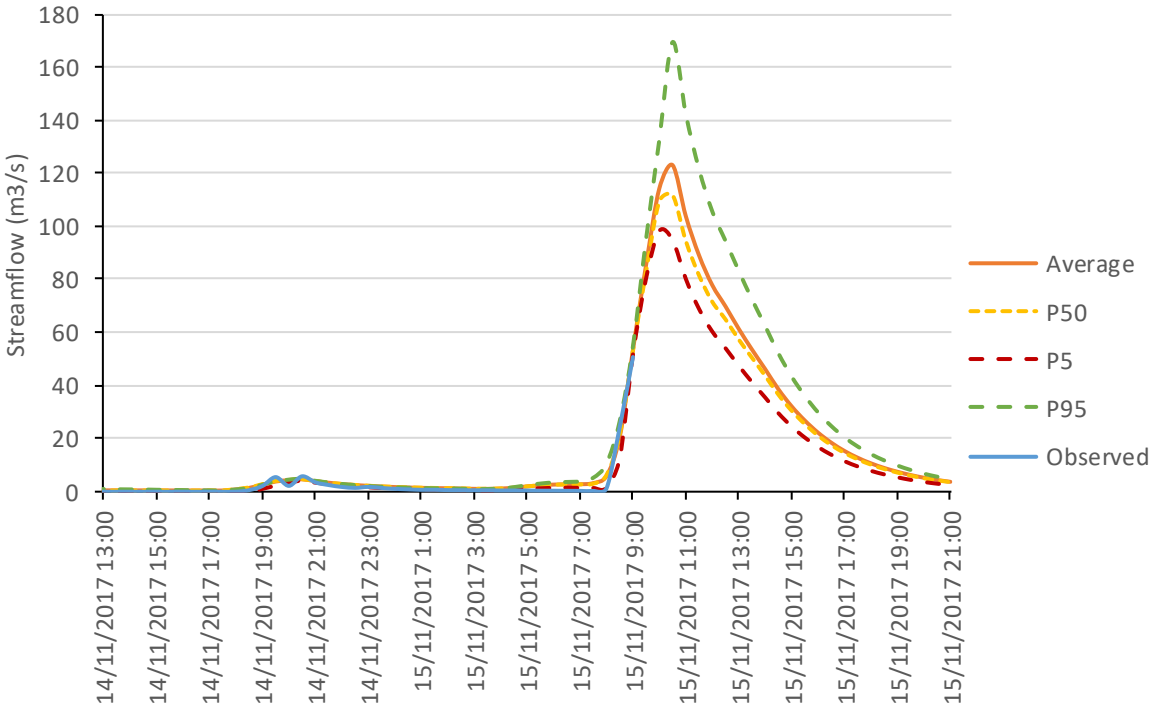

Figure 8.2. Average simulated streamflow at Gyra Stefanis and confidence intervals for 95%, 50% and 5% non-exceedance probability for simulation MC1-B-I

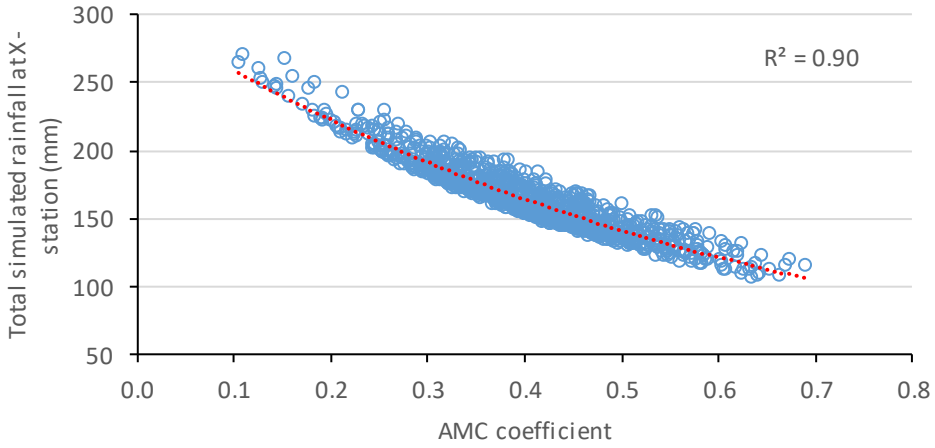

Figure 8.3. Total simulated rainfall at X-station vs antecedent moisture conditions coefficient for simulation MC1-B-I

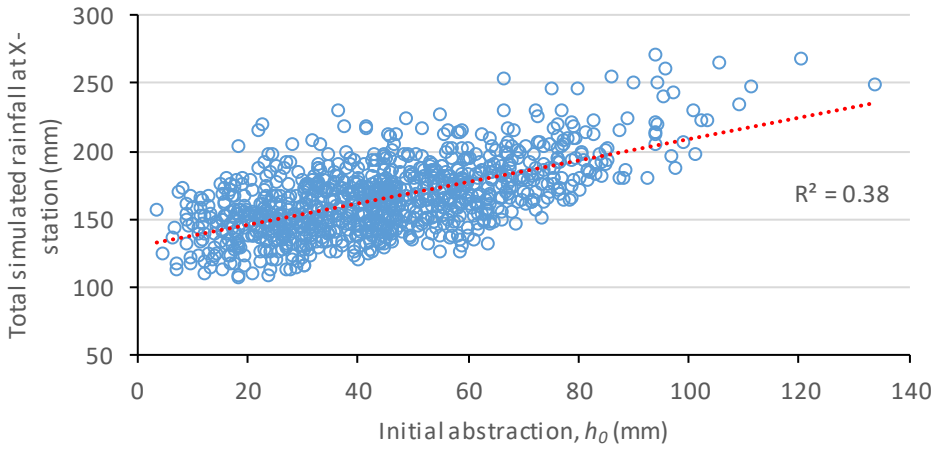

Figure 8.4. Total simulated rainfall at X-station vs initial abstraction for simulation MC1-B-I

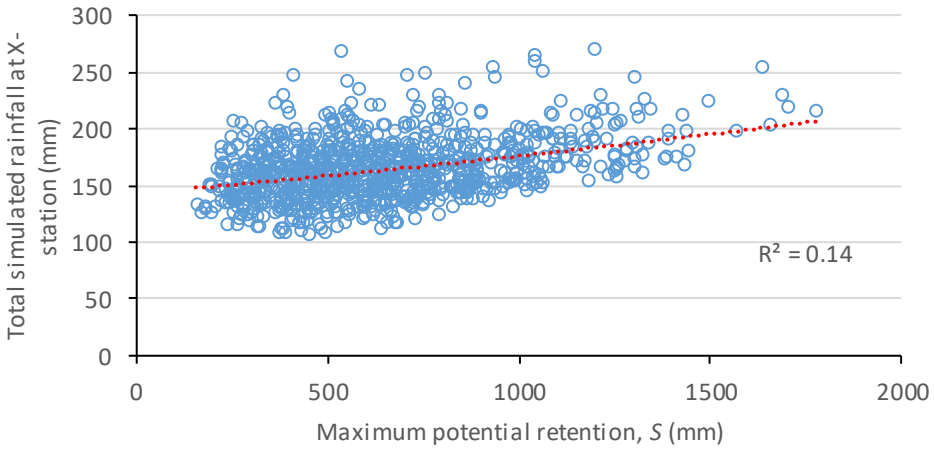

Figure 8.5. Total simulated rainfall at X-station vs maximum potential retention for simulation MC1-B-I

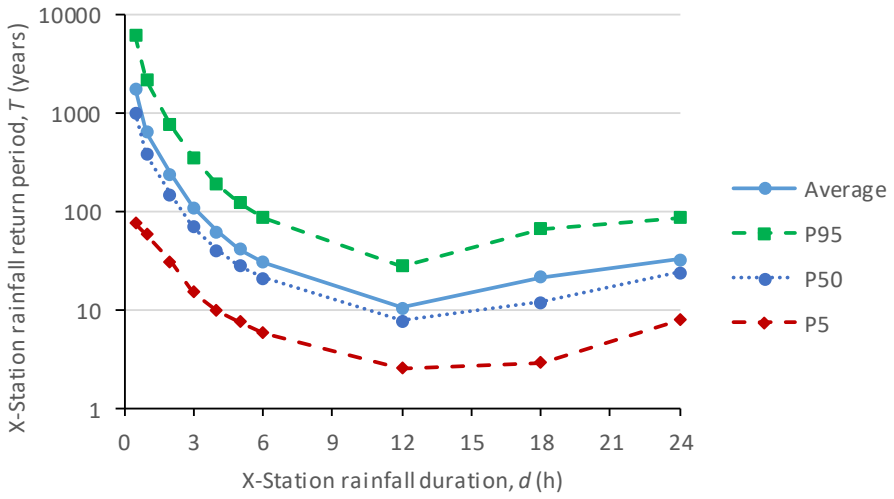

Figure 8.6. Estimated return period and confidence intervals for 95%, 50% and 5% non-exceedance probability vs time scale (duration) for simulation MC1-B-I

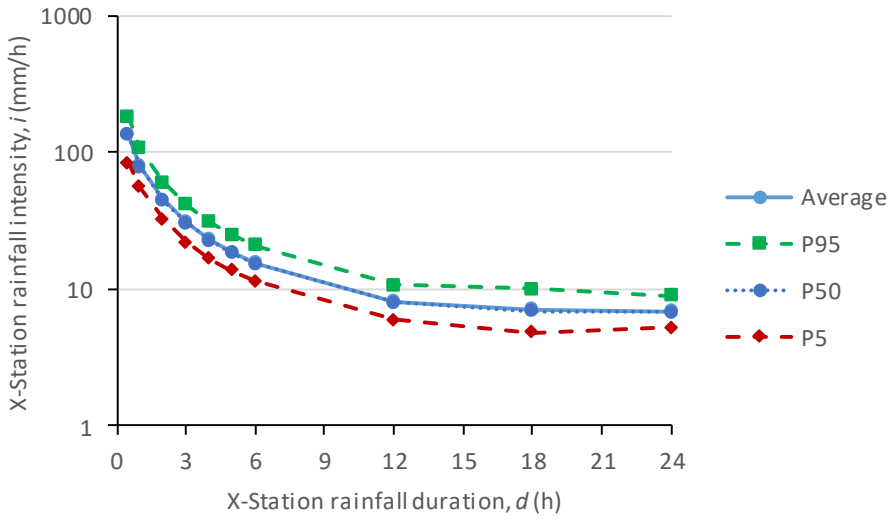

Figure 8.7. X-station simulated rainfall intensity and confidence intervals for 95%, 50% and 5% non-exceedance probability vs time scale (duration) for simulation MC1-B-I

8.3.2 Simulation MC2-B-I

Simulation MC2-B-I is the second Monte Carlo simulation using Model B-I. The simulation is again performed for 1000 iterations but this time, within the optimization procedure, the simulated rainfall depths at X-station are constrained between 0 and 50 mm.

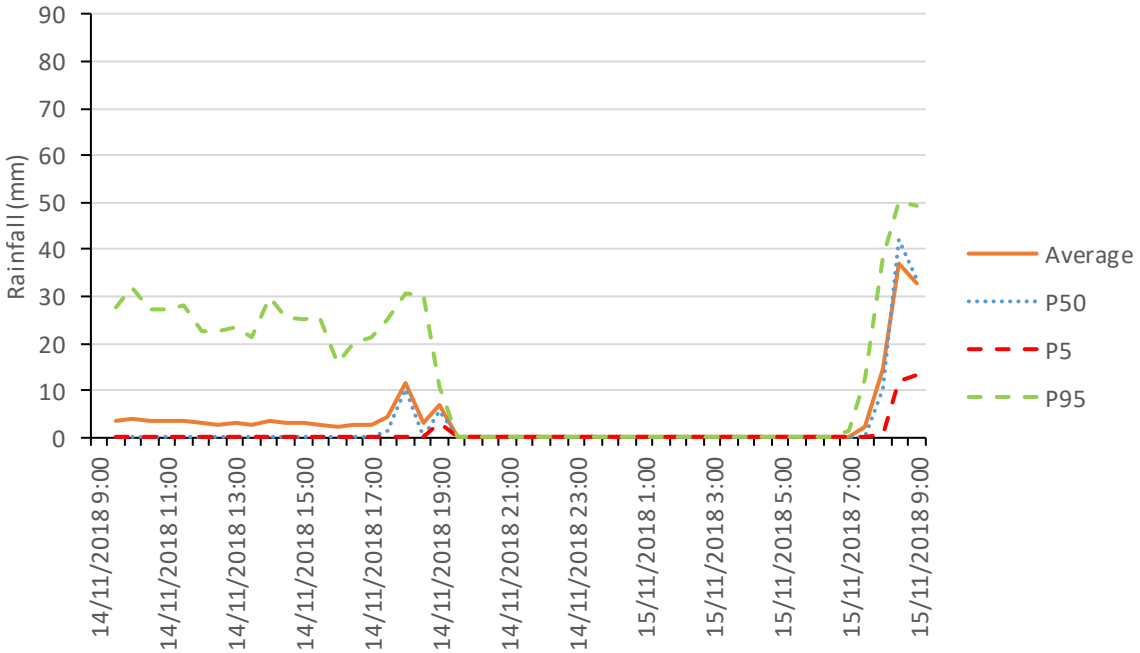

Figure 8.8. Average simulated rainfall at X-station and confidence intervals for 95%, 50% and 5% non-exceedance probability for simulation MC2-B-I

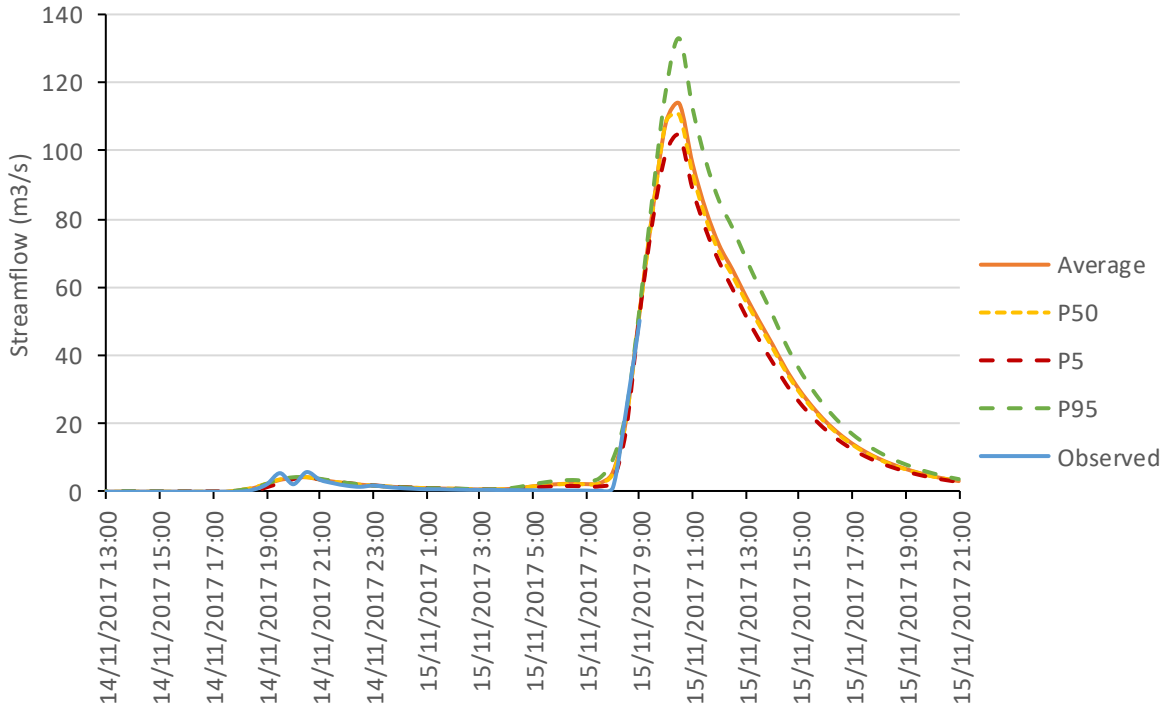

Figure 8.9. Average simulated streamflow at Gyra Stefanis and confidence intervals for 95%, 50% and 5% non-exceedance probability for simulation MC2-B-I

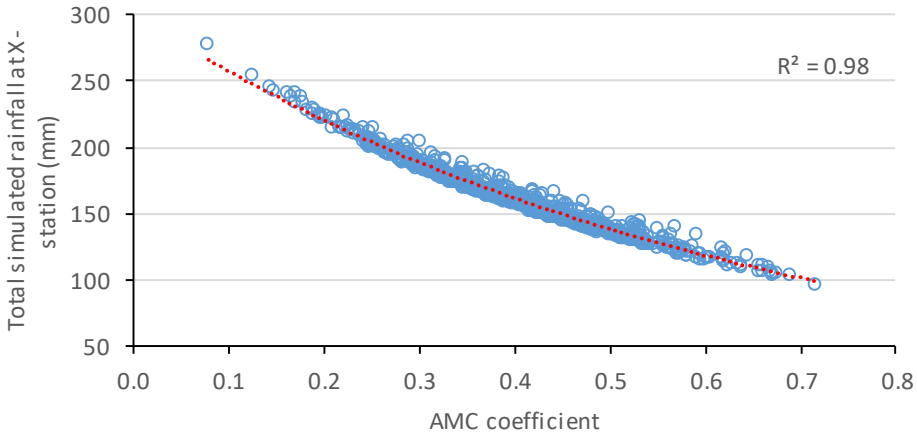

Figure 8.10. Total simulated rainfall at X-station vs antecedent moisture conditions coefficient for simulation MC2-B-I

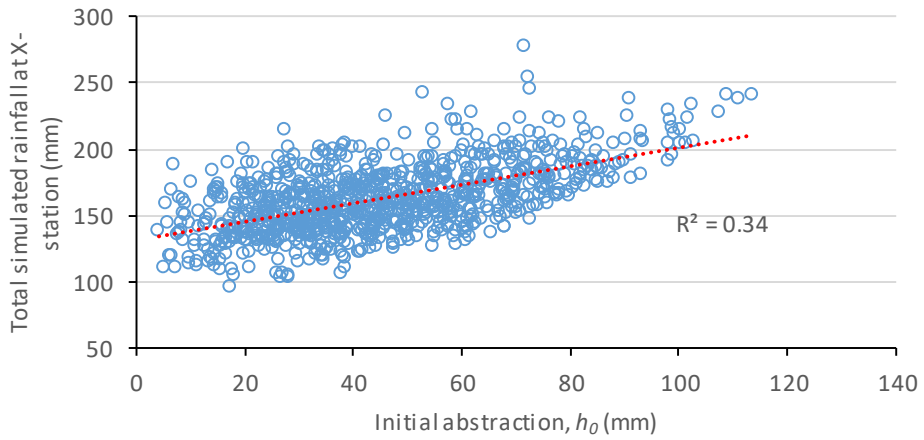

Figure 8.11. Total simulated rainfall at X-station vs initial abstraction for simulation MC2-B-I

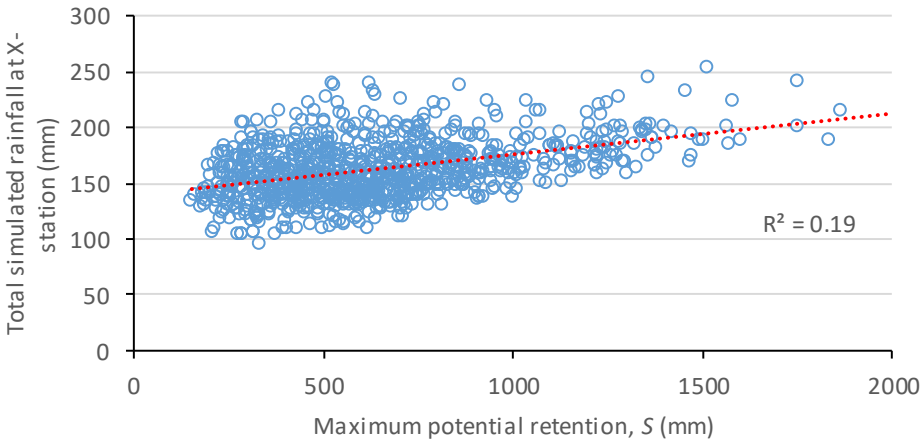

Figure 8.12. Total simulated rainfall at X-station vs maximum potential retention for simulation MC2-B-I

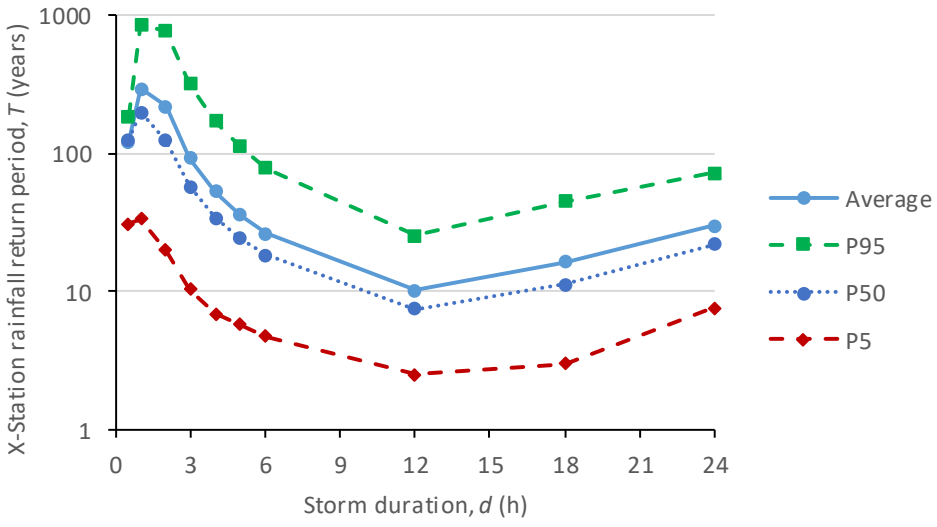

Figure 8.13. Estimated return period and confidence intervals for 95%, 50% and 5% non-exceedance probability vs time scale (duration) for simulation MC2-B-I

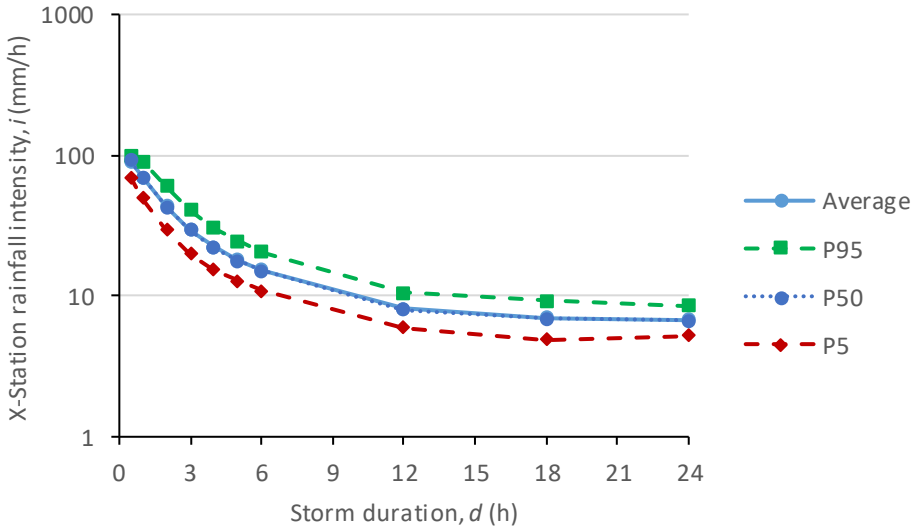

Figure 8.14. X-station simulated rainfall intensity and confidence intervals for 95%, 50% and 5% non-exceedance probability vs time scale (duration) for simulation MC2-B-I

The average simulated rainfall at X-station and its confidence intervals for 95%, 50% and 5% non-exceedance probability called P95, P50 and P5, respectively, are presented in Figure 8.8, while the average simulated streamflow at Gyra Stefanis and its corresponding confidence intervals are shown in Figure 8.9. Figures 8.10 to 8.12 are scatter plots of the total simulated rainfall at station X vs the antecedent moisture conditions coefficient, the initial abstraction and the maximum potential retention, respectively.

The average estimated return period with its confidence intervals for 95%, 50% and 5% non-exceedance probability are plotted in Figure 8.13. Similarly, the average rainfall intensity and its confidence intervals are plotted in Figure 8.14.

8.4 Model B-II

8.4.1 Simulation MC3-B-II

MC3-B-II uses Model B-II. The simulation is performed for 1000 iterations. Within optimization the simulated rainfall depths at X-station, are constrained between 0 and 100 mm. This corresponds to a maximum 30-min intensity of 200 mm/h, which is extremely high. From a practical point-of-view, the rainfall can be considered unconstrained.

The average simulated rainfall at X-station and its confidence intervals for 95%, 50% and 5% non-exceedance probability called P95, P50 and P5, respectively, are presented in Figure 8.15, while the average simulated streamflow at Gyra Stefanis and its corresponding confidence intervals can be seen in Figure 8.16. Figures 8.17 to 8.19 are scatter plots of the total simulated rainfall at

X-station vs the antecedent moisture conditions coefficient and the initial abstraction, respectively.

Regarding the probabilistic analysis, the average estimated return period with its confidence intervals for 95%, 50% and 5% non-exceedance probability are plotted in Figure 8.20. Similarly, the average rainfall intensity and its confidence intervals are plotted in Figure 8.21.

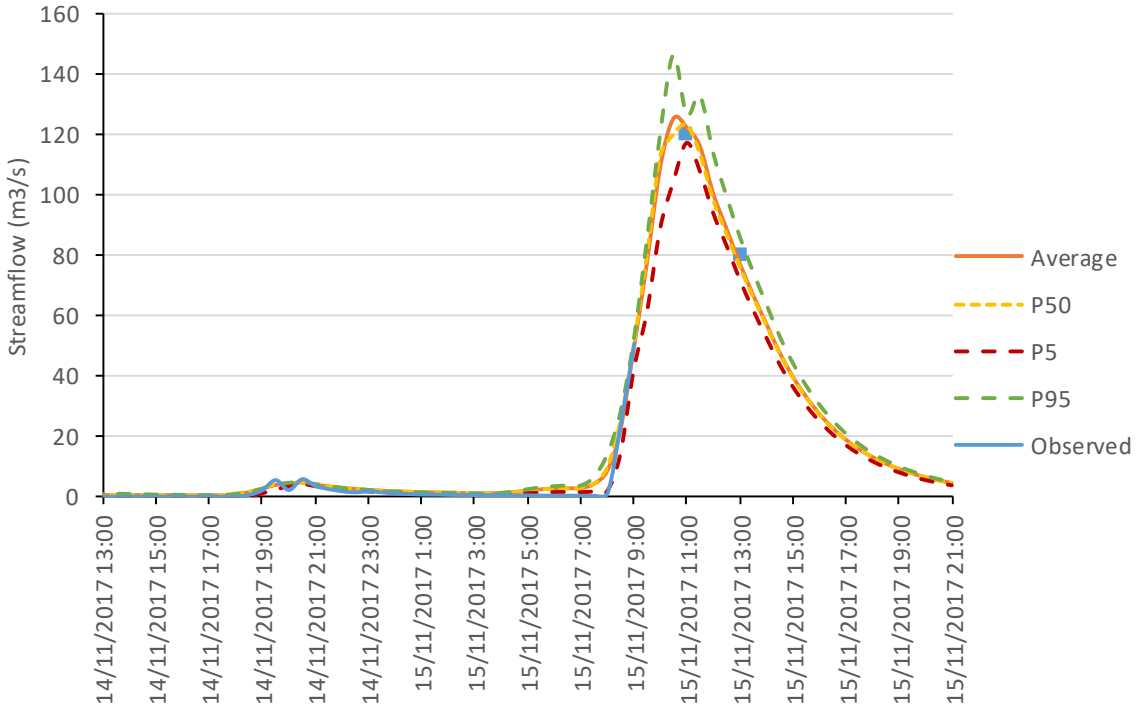

Figure 8.15. Average simulated rainfall at X-station and confidence intervals for 95%, 50% and 5% non-exceedance probability for simulation MC3-B-II

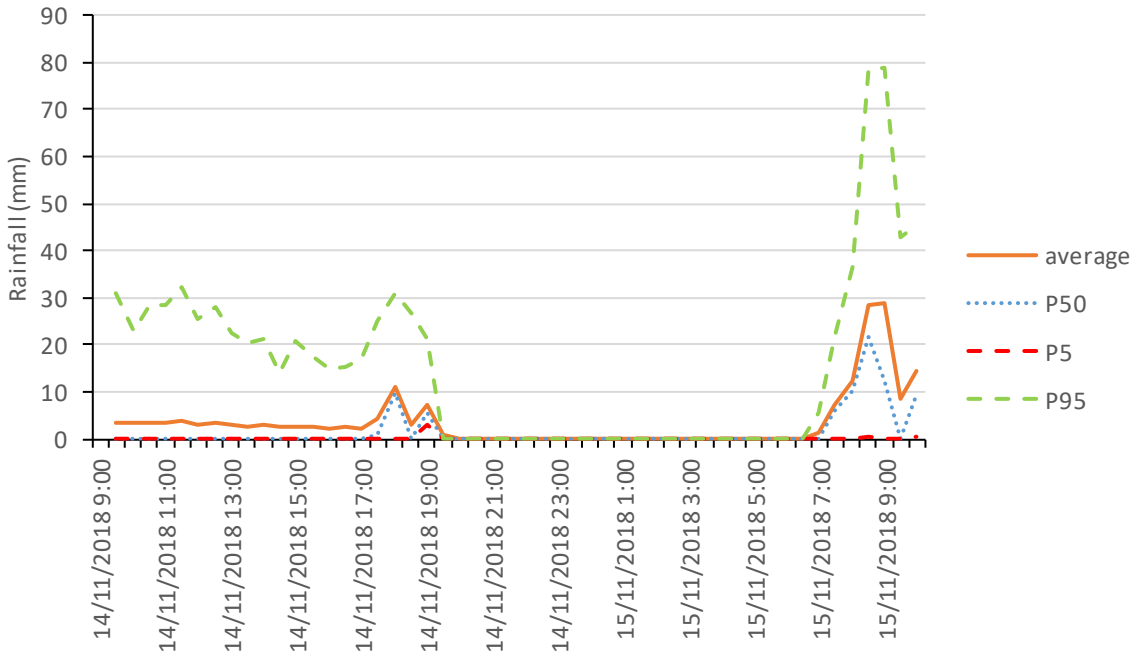

Figure 8.16. Average simulated streamflow at Gyra Stefanis and confidence intervals for 95%, 50% and 5% non-exceedance probability for simulation MC3-B-II

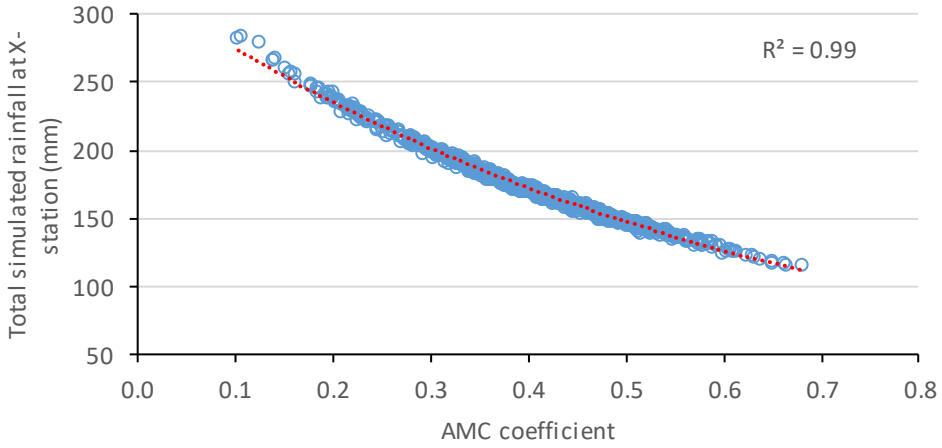

Figure 8.17. Total simulated rainfall at X-station vs antecedent moisture conditions coefficient for simulation MC3-B-II

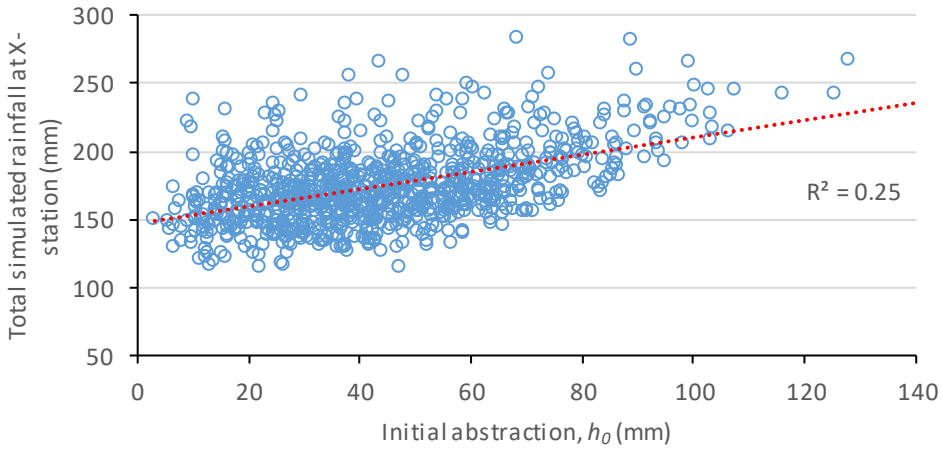

Figure 8.18. Total simulated rainfall at X-station vs initial abstraction for simulation MC3-B-I

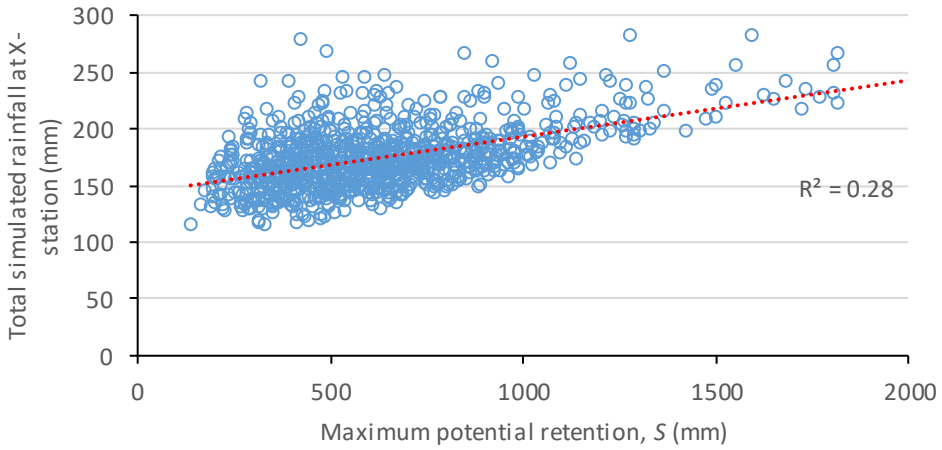

Figure 8.19. Total simulated rainfall at X-station vs maximum potential retention for simulation MC3-B-I

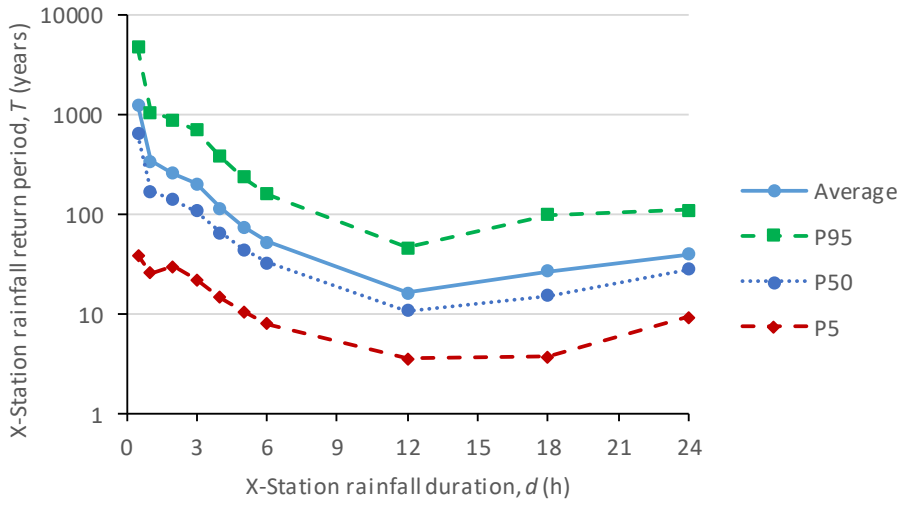

Figure 8.20. Estimated return period and confidence intervals for 95%, 50% and 5% non-exceedance probability vs time scale (duration) for simulation MC3-B-II

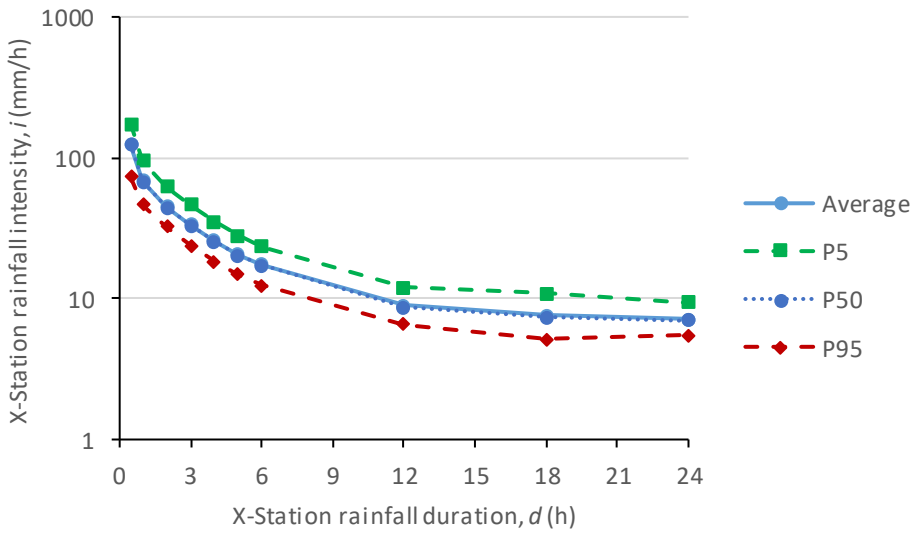

Figure 8.21. X-station simulated rainfall intensity and confidence intervals for 95%, 50% and 5% non-exceedance probability vs time scale (duration) for simulation MC3-B-II

8.4.2 Simulation MC4-B-II

Simulation MC4-B-II is the second Monte Carlo simulation using Model B-II. The simulation is again performed for 1000 iterations but this time, within the optimization procedure, the rainfall at X-station, at each time step, is constrained between 0 and 50 mm.

The average simulated rainfall at X-station and its confidence intervals for 95%, 50% and 5% non-exceedance probability are presented in Figure 8.22, while the average simulated streamflow at Gyra Stefanis and its corresponding confidence intervals are shown in Figure 8.23. Figures 8.10 to 8.12 are scatter plots of the total simulated rainfall at X-station vs the antecedent moisture conditions coefficient, the initial abstraction and the maximum potential retention, respectively.

The average estimated return period with its confidence intervals for 95%, 50% and 5% non-exceedance probability called P95, P50 and P5, respectively, are plotted in Figure 8.27. Similarly, the average rainfall intensity and its confidence intervals are plotted in Figure 8.28.

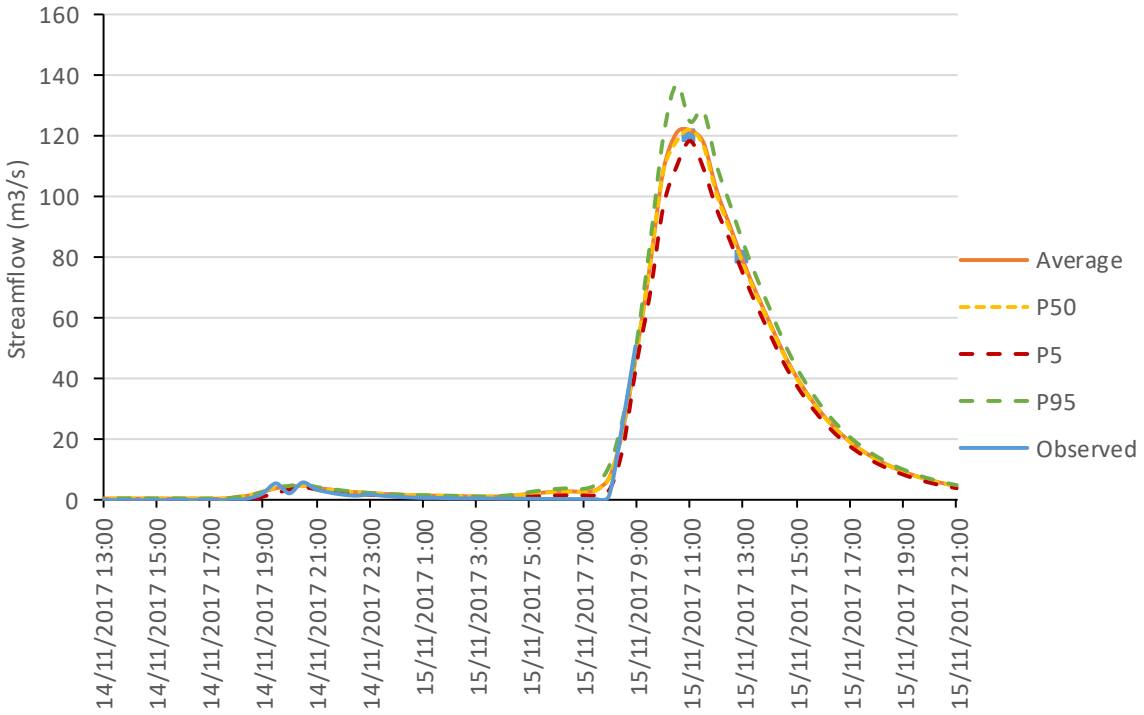

Figure 8.22. Average simulated rainfall at X-station and confidence intervals for 95%, 50% and 5% non-exceedance probability for simulation MC4-B-II

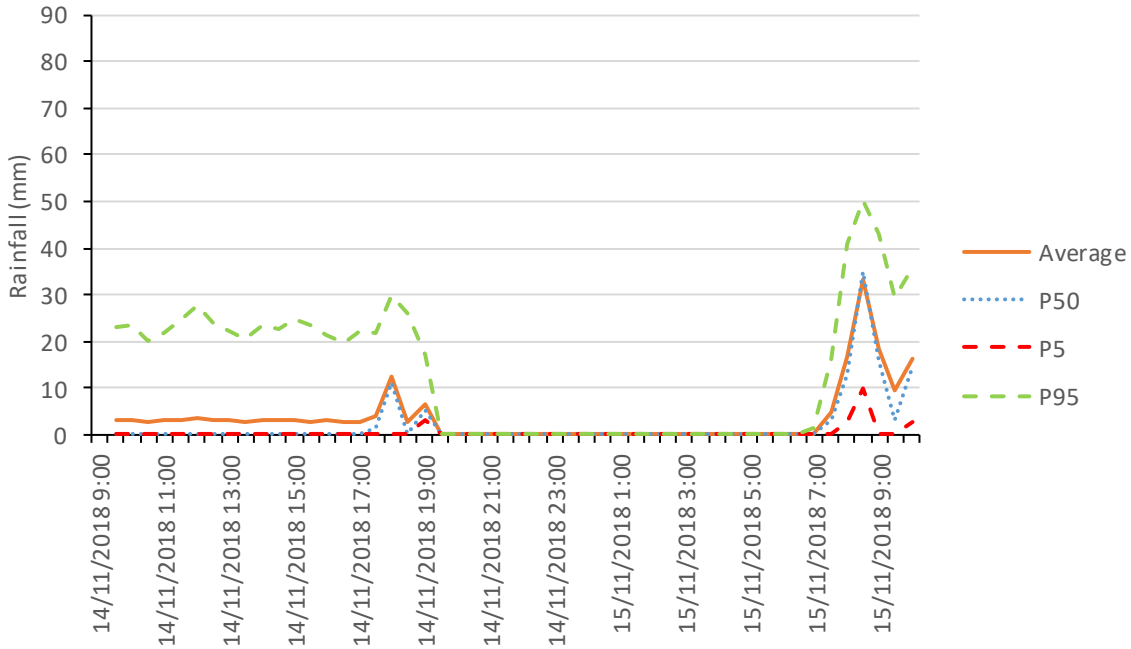

Figure 8.23. Average simulated streamflow at Gyra Stefanis and confidence intervals for 95%, 50% and 5% non-exceedance probability for simulation MC4-B-II

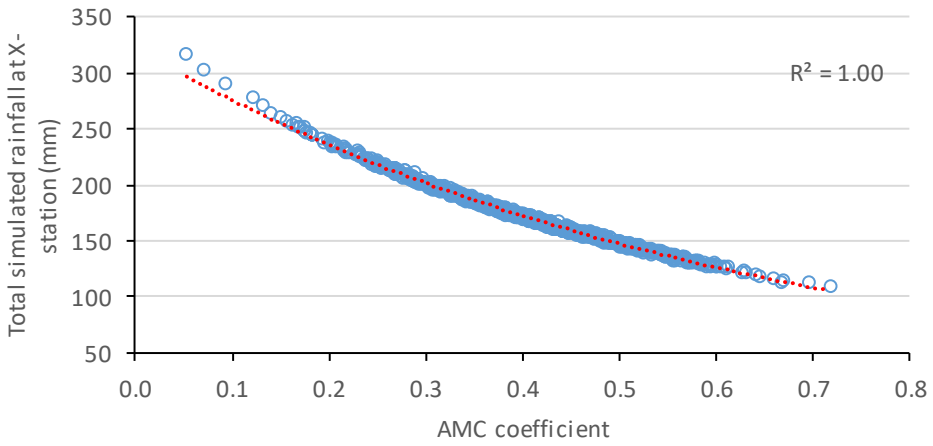

Figure 8.24. Total simulated rainfall at X-station vs antecedent moisture conditions coefficient for simulation MC4-B-II

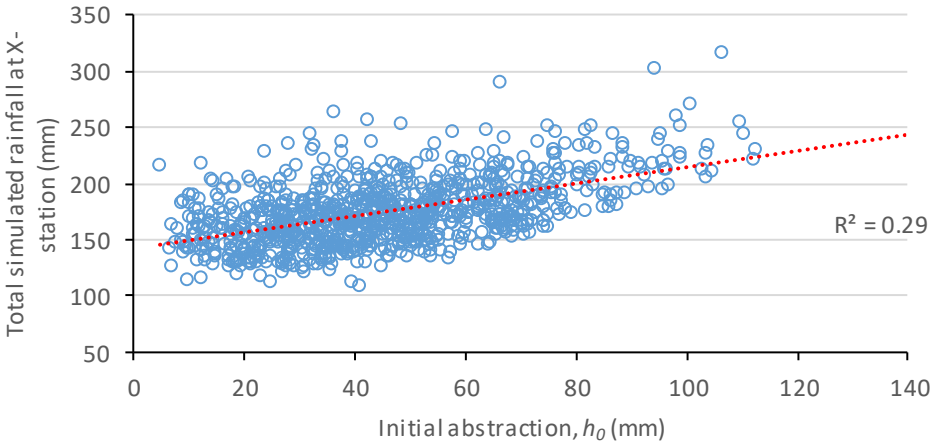

Figure 8.25. Total simulated rainfall at X-station vs initial abstraction for simulation MC4-B-II

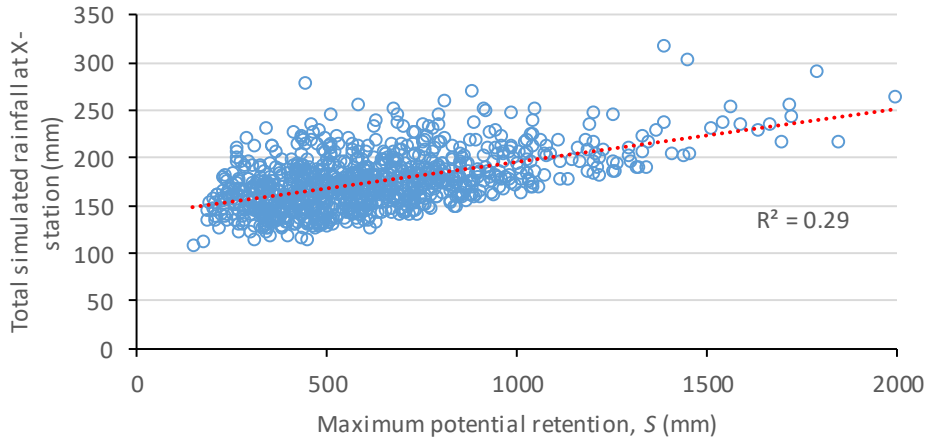

Figure 8.26. Total simulated rainfall at X-station vs maximum potential retention for simulation MC4-B-II

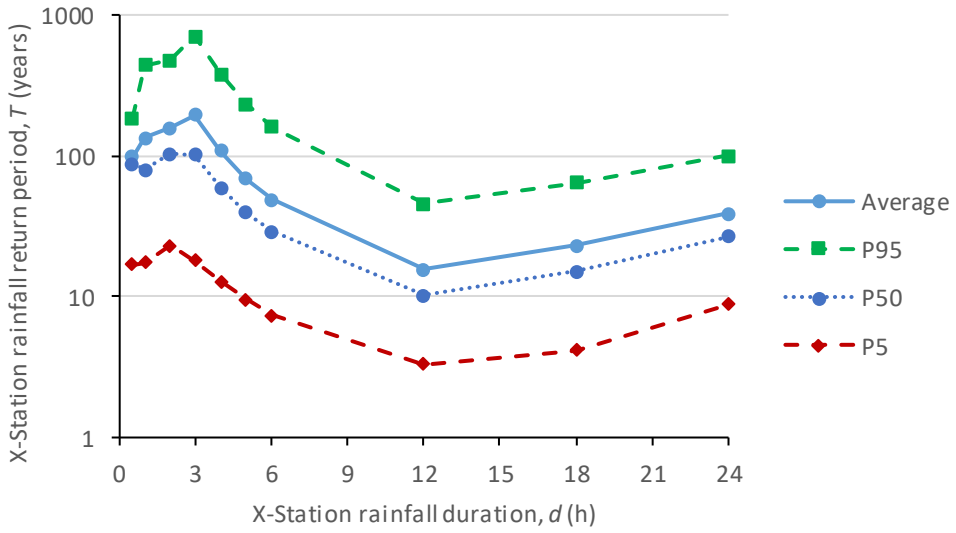

Figure 8.27. Estimated return period and confidence intervals for 95%, 50% and 5% non-exceedance probability vs time scale (duration) for simulation MC4-B-II

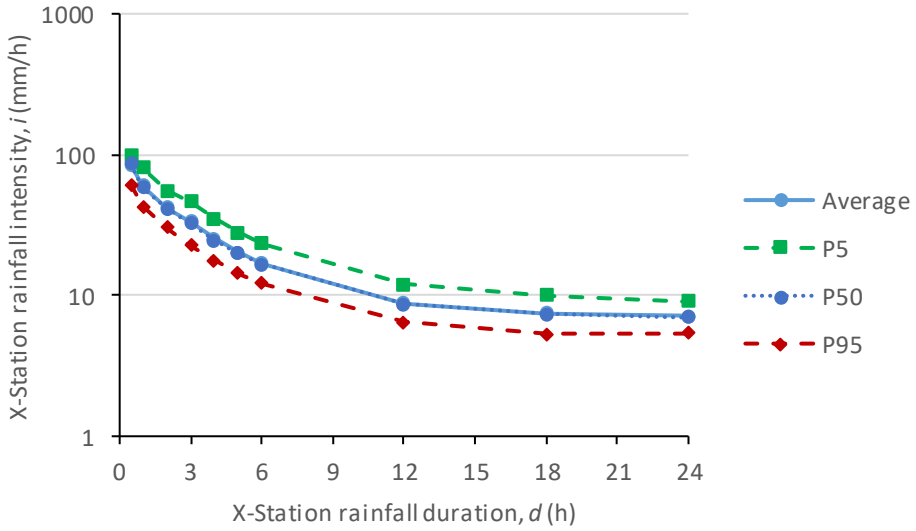

Figure 8.28. X-station simulated rainfall intensity and confidence intervals for 95%, 50% and 5% non-exceedance probability vs time scale (duration) for simulation MC4-B-II

8.5 Discussion

The average and standard deviation of the simulated total and maximum 30-min rainfall at X-station, as well as the simulated peak flow at Gyra Stefanis for each Monte Carlo simulation, are presented in Table 8.3. The statistical characteristics of the estimated return period and simulated rainfall intensity for each of the Monte Carlo simulations are presented in Table 8.4 and Table 8.5.

All simulations result in two rainfall clusters, one during the morning and afternoon hours of November 14th and a short yet very intense one during the morning hours of November 15th. The confidence intervals of the simulated rainfall patterns indicate that there is a large range of rainfall patterns, in terms of intensity and temporal evolution, which could ensure perfect fitting to the observed flows of Sarantapotamos until 9:00 am. These confidence intervals seem unaffected by the additional information carried by the extra calibration points of Model B-II. However, by constraining the rainfall within the optimization procedure, they can be noticeably reduced, especially for the rainfall cluster during the morning hours of November 14th, which caused the flash flood.

Table 8.3. Statistical characteristics of total and maximum simulated rainfall at X-station and peak flow at Gyra Stefanis for each simulation

Simulation	Total simulated rainfall at X-station (mm)		Maximum simulated rainfall at X-station (mm)		Simulated peak flow at Gyra Stefanis (m^3/s)	
	Average	St. deviation	Average	St. deviation	Average	St. deviation
MC1-B-I	165.4	26.8	67.4	15.2	126.5	21.8
MC2-B-I	162.6	25.8	45.1	5.1	114.3	8.1
MC3-B-II	174.9	27.6	62.2	15.4	132.3	8.9
MC4-B-II	175.0	28.8	42.5	6.4	126.8	4.8

Table 8.4. Statistical characteristics of estimated return period vs time scale (duration) for each Monte Carlo simulation

Simulation		Time scale (duration), *d* (h)									
		0.5	1.0	2.0	3.0	4.0	5.0	6.0	12.0	18.0	24.0
		Return period, *T* (years)									
MC1-B-I	Average	1805	649	244	112	63	42	31	11	22	33
	St. deviation	2023	878	292	135	71	49	36	10	31	32
	Minimum	9	10	9	5	3	3	2	2	2	4
	Maximum	11038	14693	2968	1564	799	794	607	150	387	303
MC2-B-I	Average	122	297	219	93	53	36	26	10	16	30
	St. deviation	55	289	291	112	59	37	26	9	16	27
	Minimum	9	7	6	4	3	2	2	1	1	3
	Maximum	186	1464	2940	1092	563	344	233	118	175	354
MC3-B-II	Average	1263	340	261	203	116	74	53	16	27	40
	St. deviation	1650	628	385	312	172	103	72	18	35	40
	Minimum	5	4	5	5	3	2	2	2	1	3
	Maximum	11035	9333	4082	2911	1779	1056	717	203	357	377
MC4-B-II	Average	98	135	159	196	108	69	49	15	23	39
	St. deviation	59	160	179	308	159	97	66	17	28	43
	Minimum	5	6	7	5	3	2	2	1	2	3
	Maximum	186	1448	1514	3483	1734	1030	681	198	389	561

Table 8.5. Statistical characteristics of simulated rainfall intensity at X-station vs time scale (duration) for each Monte Carlo simulation

Simulation		Time scale (duration), *d* (h)									
		0.5	1.0	2.0	3.0	4.0	5.0	6.0	12.0	18.0	24.0
		Rainfall intensity, *i* (mm/h)									
MC1-B-I	Average	134.8	79.7	45.4	30.9	23.3	18.8	15.8	8.2	7.2	6.9
	St. deviation	30.5	15.6	8.4	5.8	4.3	3.4	2.9	1.4	1.7	1.1
	Minimum	52.1	37.5	24.9	16.6	12.7	10.2	8.5	5.2	4.0	4.5
	Maximum	200.0	145.0	75.7	53.5	40.2	35.1	29.9	15.2	14.1	11.3
MC2-B-I	Average	90.1	70.3	43.7	29.5	22.3	18.1	15.2	8.1	7.0	6.8
	St. deviation	10.1	13.1	9.2	6.0	4.4	3.5	2.9	1.5	1.4	1.1
	Minimum	52.4	34.9	22.5	15.6	12.3	9.8	8.2	4.7	3.4	4.0
	Maximum	100.0	100.0	75.6	50.4	37.8	30.2	25.2	14.5	12.2	11.6
MC3-B-II	Average	84.9	60.2	42.2	33.4	25.2	20.3	17.0	8.8	7.5	7.2
	St. deviation	12.8	11.7	7.6	7.2	5.3	4.2	3.5	1.7	1.5	1.2
	Minimum	45.8	32.6	23.5	16.7	12.5	10.0	8.3	4.8	4.2	4.1
	Maximum	100.0	99.8	67.7	61.1	45.8	36.7	30.6	16.0	14.1	11.7
MC4-B-II	Average	84.9	60.2	42.2	33.4	25.2	20.3	17.0	8.8	7.5	7.1
	St. deviation	12.8	11.7	7.6	7.2	5.3	4.2	3.5	1.7	1.5	1.2
	Minimum	45.8	32.6	23.5	16.7	12.5	10.0	8.3	4.8	4.2	4.1
	Maximum	100.0	99.8	67.7	61.1	45.8	36.7	30.6	16.0	14.1	12.6

The same outcomes can be extracted for simulated streamflow. Simulation MC1-B-I, which embeds the least information, results in the largest confidence intervals. Adding the additional information to Model B-II can significantly reduce the uncertainty of the peak flow estimation and by also constraining the maximum simulated rainfall, it can be reduced further. By also comparing the average streamflow values with the median (50% non-exceedance probability) for simulation MC1-B-I, we notice that 50% of the peak flow estimations is lower than the average. The difference between the two values is gradually reduced by adding extra information to the optimization procedure.

The results of the probabilistic analysis are not different. In terms of return period estimations, all simulations result in large confidence intervals and the values vary significantly. However, comparisons in terms of rainfall intensities, allow for more safe conclusions. All simulations result in almost identical simulated rainfall intensities, with large intensities over short durations. Another noticeable result is that constraining the simulated maximum rainfall within the optimization procedure can significantly affect the estimated return periods, but not the simulated rainfall intensities, which present a more stable behavior. This is due to the sensitivity of idf curves, providing significantly different return period estimations for small changes of rainfall intensity.

9. Justification based on other sources of information

9.1 X-Band weather radar

The X-POL weather radar is a radar unit using a double polarization Doppler system with a wave length of 3.2 cm (X-Band). The system range can be selected up to 150 km, the resolution up to 30 m and the maximum antenna rotation speed up to 25 degrees per second. The parameters measured with this system are, among others, the horizontal and vertical polarization reflectance, the Doppler velocity, the spectral range and differential phase shift. This radar system can estimate the precipitation distribution characteristics in a high resolution, with distinction between the liquid and solid phase of the water (http://www.meteo.noa.gr).

A similar radar unit was operated by the National Observatory of Athens during the storm event and provided rainfall estimations in 10-min intervals over the wider area of Western Attica (Kalogiros, personal communication). Using GIS tools, we estimated the areal rainfall over the Sarantapotamos basin at 10-min intervals and then aggregated to obtain the 30-min time series. This data was used as input for calibrating Model B-I against the observed flood event, assuming two free parameters, i.e. the initial abstraction ratio, a, and the antecedent moisture conditions coefficient, AMC_{coef}. The resulting hydrograph is presented in Figure 9.1 and the optimized values for the initial parameters are a = 0.4 and AMC_{coef} = 0.94. It is worth noting that, although the observed flows of Sarantapotamos are adequately simulated, the resulting values of the initial parameters match their upper boundaries and this scenario seems far from reality. Similar attempts, using the rest of the models of this study, lead to the same conclusion.

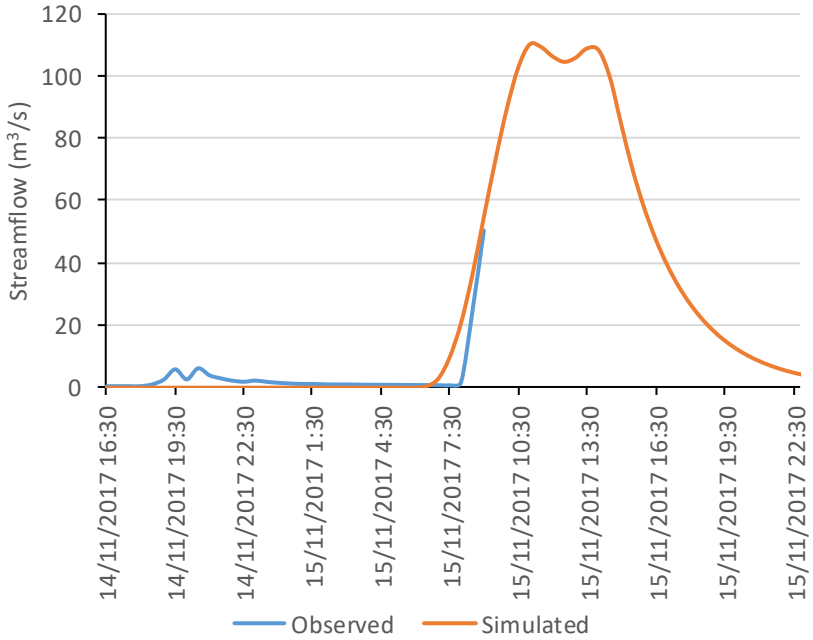

Figure 9.1. Simulated hydrograph using the average rainfall estimated by the X-POL radar (Model B-I)

This average areal rainfall estimated by the radar is also compared to the average rainfall over the entire study area, estimated by each of the Monte Carlo simulations of Chapter 8 and presented in Figure 9.2 and Figure 9.3, respectively. It should be noted that the radar estimations are an order of magnitude lower that the average Monte Carlo simulations. Taking this into account, the radar estimations are only used as proxy information, as an indicator of the temporal evolution of the storm, and not as an estimator of the actual rainfall.

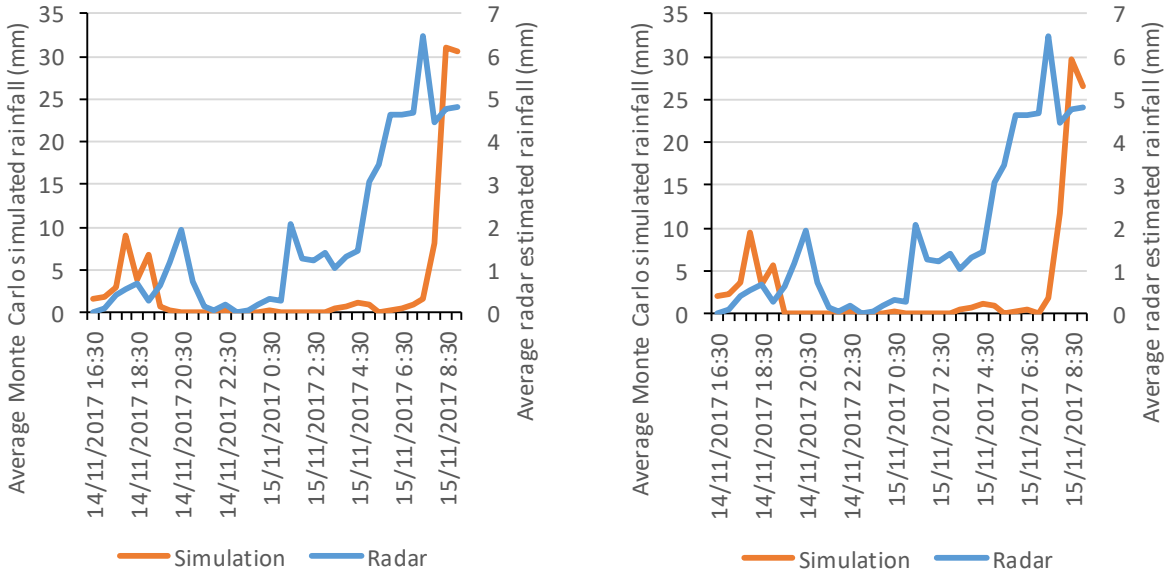

Figure 9.2. Average areal rainfall estimated by the X-POL radar vs average simulated areal rainfall for simulation MC1-B-I (left) and MC2-B-I (right)

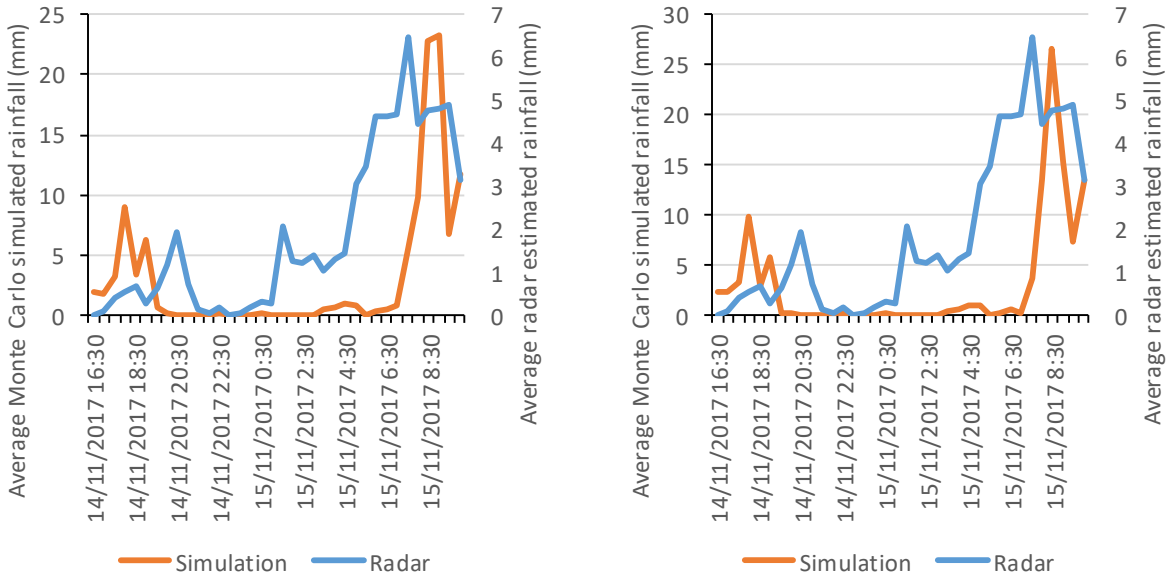

Figure 9.3. Average areal rainfall estimated by the X-POL radar vs average simulated areal rainfall for simulation MC3-B-II (left) and MC4-B-II (right)

9.2 Past flood events

As stated before, the Monte Carlo simulations presented in Chapter 8 resulted in two distinct rainfall clusters, one during the morning and afternoon hours of November 14th and one during the morning hours of November 15th. The second cluster is shorter and more intense and resulted in the examined flash flood, thus the average simulated rainfall intensity over the study basin is plotted against the average simulated peak flow at Gyra Stefanis for each Monte Carlo simulation. These plots are compared to the trend line formed by the average rainfall intensity and peak flow reported by Efstratiadis *et al.* (2014). These reports are from storm events occurred during years 2012-2014 and are plotted in Figure 9.4. This comparison is again used as an indicator that the outcomes of Monte Carlo simulation follow the observed hydrological behavior of the basin. Thus, the simulation results seem plausible.

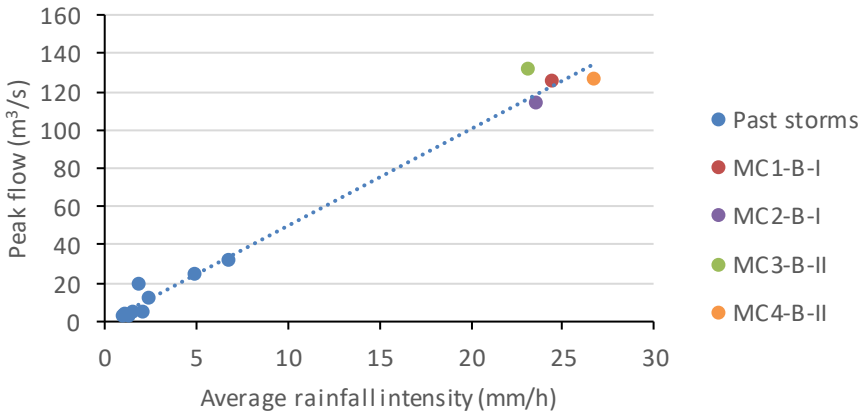

Figure 9.4. Peak flow at Gyra Stefanis vs average rainfall intensity for past flood events and Monte Carlo simulations

10. Summary, conclusions and suggestions for future research

10.1 Summary

The purpose of this research is the investigation of the storm event responsible for the flash flood in Western Attica on November 15th, 2017. The point rainfall observations at the three meteorological stations in the wider area were not significant enough to justify such a severe flooding, due to the unusual storm pattern, as it was recorded by an X-band meteorological radar.

Valuable information was found in the neighboring catchment of Sarantapotamos, provided by a hydrometric station at Gyra Stefanis and a meteorological station in Vilia. This information, is used in an attempt to estimate the rainfall over the basin of Sarantapotamos through a reverse rainfall-runoff modeling approach. This approach employs the SCS-CN method and also takes advantage of qualitative information of the streamflow during the flood.

Several hydrological scenarios are tested through various modeling schemes, revealing major uncertainty due to the lack of information. In order to better assess this uncertainty, we employ Monte Carlo simulations against the model's initial parameters. These parameters are sampled from suitable distributions by taking advantage of the hydrological regime of the basin and the soil conditions days before the event.

Based on the outcomes of Monte Carlo simulations, we provided probabilistic estimations of the total rainfall over the study area, its temporal evolution, and the peak flow of Sarantapotamos at Gyra Stefanis. We also employed risk evaluations, by estimating the maximum intensities and associated return periods of the storm event across several time scales. We then compared these results to additional sources of information.

The conclusions of the aforementioned analysis, as well as suggestions for further improving this research, are presented below.

10.2 Conclusions

- The reverse rainfall-runoff procedure highly depends on the sole parameter of the rainfall-runoff transformation (i.e., the initial abstraction ratio) and its initial condition, expressed in terms of the originally introduced AMC coefficient. Our investigations showed that little changes in these parameters can result in significantly different simulation results.
- The results are also quite sensitive to the model structure. Depending on which of the proposed models is used, the analysis leads to different quantitative estimations, but within a common pattern. In particular, all Monte Carlo scenarios agree that the rainfall comprised two distinct clusters, i.e. one during the evening hours of November 14th and a second, more intense cluster during the morning hours of November 15th, causing the flash flood. This is also supported by reports of the local residents.

- The value of data, even in terms of approximate information, is indisputable. Although almost all reproduced rainfall scenarios ensured perfect fitting to the observed flows of Sarantapotamos, any means of additional information added to the reverse calibration problem helped significantly, reducing the uncertainty. A bright example of this are the two additional calibration points in Model B-II, which shorten the confidence intervals of both rainfall and peak flow estimations. A summary of key results is presented in Table 10.1, with their confidence intervals for 95%, 50% and 5% non-exceedance probability called P95, P50 and P5, respectively.

Table 10.1. Peak flow estimations with confidence intervals for each Monte Carlo simulation

		MC1-B-I	MC2-B-I	MC3-B-II	MC4-B-II
Peak flow (m^3/s)	Average	126.5	114.3	132.3	126.8
	St. dev.	21.8	8.1	8.9	4.8
	P95	169.7	133.2	146.3	136.9
	P50	113.1	110.4	130.5	125.0
	P5	107.9	108.7	120.7	121.5
Total rainfall at X-station (mm)	Average	165.4	162.6	174.9	175.0
	St. dev.	26.8	25.8	27.6	28.8
	P95	214.2	205.8	228.6	227.5
	P50	163.9	160.1	171.4	172.4
	P5	126.3	124.9	135.9	133.6

- The Monte Carlo simulation is a method that allows for quantifying uncertainty, using empirical measures of variability (e.g., confidence intervals). It also allows for accounting for a priori information about the anticipated statistical behavior of a model, expressed in terms of a priori distributions for parameter sampling.
- The simulated rainfall patterns resulted in significantly varying estimations of the return period of maximum rainfall intensities across scales, which makes it difficult to extract safe conclusions about the extremeness of this event. This is due to the mathematical structure of the idf curves, which are substantially sensitive against frequency (return period) for small changes of rainfall intensity. As shown in Table 10.2, the confidence intervals of rainfall probability, expressed in terms of return period, may differ one or two orders of magnitude. In our opinion, the use of return period as an easy means to communicate with common people and stakeholders should be done very carefully, in order to prohibit misleading conclusions about the risk of hydrometeorological hazards.

Table 10.2. Estimated return period and simulated rainfall intensity at X-station with their confidence intervals vs time scale (duration) for each Monte Carlo simulation

		Time scale, *d* (h)				Time scale, *d* (h)			
		0.5	1	3	24	0.5	1	3	24
		Return period, *T* (years)				Rainfall intensity, *i* (mm/h)			
MC1-B-I	Average	1805	649	112	33	134.8	79.7	30.9	6.9
	St. dev.	2023	878	135	32	30.5	15.6	5.8	1.1
	P95	6270	2177	359	88	182.9	106.8	41.5	8.9
	P50	1017	386	70	24	135.6	79.3	30.4	6.8
	P5	77	59	15	8	84.3	55.5	21.9	5.3
MC2-B-I	Average	122	297	93	30	90.1	70.3	29.5	6.8
	St. dev.	55	289	112	27	10.1	13.1	6.0	1.1
	P95	186	863	320	72	100.0	91.4	40.6	8.6
	P50	125	199	58	22	92.8	70.2	29.2	6.7
	P5	31	34	10	8	69.9	49.3	20.0	5.2
MC3-B-II	Average	1263	340	203	40	124.4	69.3	33.8	7.2
	St. dev.	1650	628	312	40	30.8	15.3	6.9	1.2
	P95	4731	1058	703	111	73.2	46.5	23.9	5.5
	P50	648	171	108	28	125.4	68.3	33.1	7.0
	P5	39	26	22	9	174.9	94.6	46.7	9.3
MC4-B-II	Average	98	135	196	39	84.9	60.2	33.4	7.1
	St. dev.	59	160	308	43	12.8	11.7	7.2	1.2
	P95	186	444	712	100	100.0	81.3	46.8	9.1
	P50	88	80	101	27	86.6	58.9	32.7	7.0
	P5	17	18	18	9	61.2	42.8	22.8	5.4

- Despite the large uncertainty that accompanies this analysis, the overall outcomes seem plausible, if compared to the known hydrological behavior of the basin and the rainfall evolution, as it was estimated by the meteorological radar.
- The catchment of Sarantapotamos has similar geomorphological characteristics with the two small catchments upstream of Mandra and thus, by making the assumption that the same conditions apply to all the aforementioned basins, the same results could be expanded to the two catchments under study. This is supported by the fact that all simulations lead to large rainfall intensities over short duration and such rainfall estimations could be responsible for the flash flood, given that due to the small size of the catchment, its response time is quite short, thus the maximum rainfall at such duration is the most critical.

10.3 Suggestions for future research

The driving force of this study was to study the nature of the storm that caused the severe flood in Western Attica in November, 2017. This flood had a huge social impact and was the main conversation topic throughout the country for a long time, due to its unusual characteristics and devastating results. This sparked the author's interest to study this event, a motive that was supported by the challenge presented due to the limited data availability. In an attempt to resolve the mystery around this unusual storm, several reverse rainfall-runoff approaches were tested that still have room for improvement. To this extend, we present below some ideas for future research:

- The proposed methodology is based on the assumption that the station in Vilia controls 20% of the rainfall over the study area. This ratio could be further investigated.
- The rainfall observations of the meteorological radar present valuable information that is not fully exploited in this study.
- There are satellite observations available that could provide further information about the storm pattern.
- Further investigation of qualitative information provided by audiovisual material can further improve the uncertainty assessment.
- Application of a PSUH that is optimized against its parameters for this case study.
- Application of the recently proposed (Michailidi, 2018) dynamic PSUH.
- Further investigation of the methods through which this analysis could be expanded to the two catchments upstream of Mandra.

11. Literature

Apostolidis, I., V. Perleros, V. Tsatiris, and G. Vassilopoulos, *Report on the flood of November 15th 2017 at Mandra and Nea Peramos, Attica*, December 2017; http://www.geotee-anste.gr

Baltas, E. A., N. A. Dervos, and M. A. Mimikou, *Technical Note: Determination of the SCS initial abstraction ratio in an experimental watershed in Greece*, Hydrol. Earth Syst. Sci., 11, 1825-1829, doi:10.5194/hess-11-1825-2007, 2007

Banasik, K., A. Rutkowska, and S. Kohnová, *Retention and curve number variability in a small agricultural catchment: The probabilistic approach*, Water, 6, 1118-1133, 2014.

Berthet, L., Andréassian, V., Perrin, C., and Javelle, P.: *How crucial is it to account for the antecedent moisture conditions in flood forecasting? Comparison of event-based and continuous approaches on 178 catchments*, Hydrol. Earth Syst. Sci., 13, 819-831, https://doi.org/10.5194/hess-13-819-2009, 2009.

Chow V. T., Maidment D., and Mays L., *Applied Hydrology*, McGraw-Hill, Inc., 1988.

Efstratiadis A., A. Koukouvinos, E. Michailidi, E. Galiouna, K. Tzouka, A. D. Koussis, N. Mamassis, and D. Koutsoyiannis, *Description of regional approaches for the estimation of characteristic hydrological quantities*, DEUCALION – Assessment of flood flows in Greece under conditions of hydroclimatic variability: Development of physically-established conceptual-probabilistic framework and computational tools, Department of Water Resources and Environmental Engineering, 146 pages, September 2014.

Efstratiadis A., D. Koutsoyiannis, and S.M. Papalexiou, *Description of methodology for intense rainfall analysis*, DEUCALION – Assessment of flood flows in Greece under conditions of hydroclimatic variability: Development of physically-established conceptual-probabilistic framework and computational tools, Department of Water Resources and Environmental Engineering – National Technical University of Athens, 55 pages, November 2012.

Efstratiadis A., D. Koutsoyiannis, N. Mamassis, P. Dimitriadis, and A. Maheras, *Literature review of flood hydrology and related tools*, DEUCALION – Assessment of flood flows in Greece under conditions of hydroclimatic variability: Development of physically-established conceptual-probabilistic framework and computational tools, Department of Water Resources and Environmental Engineering, 115 pages, October 2012.

Efstratiadis, A., A. D. Koussis, D. Koutsoyiannis, and N. Mamassis, *Flood design recipes vs. reality: can predictions for ungauged basins be trusted?*, Natural Hazards and Earth System Sciences Discussions, 1, 7387–7416, doi:10.5194/nhessd-1-7387-2013, 2013

European Commission, *Directive 2007/60/EC of the European Parliament and of the Council of 23 October 2007 on the assessment and management of flood risks*, Official Journal of the European Union, EN, 6.11.2017, L 288/27

Kalogiros J., A. Retalis, D. Katsanos, M. Anagnostou, and E. Nikolopoulos, National Observatory of Athens press release on 20-11-2017; http://www.noa.gr

Koukouvinos A., *Geographical data and procesing*, DEUCALION – Assessment of flood flows in Greece under conditions of hydroclimatic variability: Development of physically-established conceptual-probabilistic framework and computational tools, Department of Water Resources and Environmental Engineering – National Technical University of Athens, 36 pages, March 2012.

Koussis A. D., S. Lykoudis, and G. Karavokiros, *Description of monitoring system for data transmittal and procesing*, DEUCALION – Assessment of flood flows in Greece under conditions of hydroclimatic variability: Development of physically-established conceptual-probabilistic framework and computational tools, Department of Water Resources and Environmental Engineering – National Technical University of Athens, 77 pages, March 2012.

Koutsoyiannis D. and N. Mamassis, *Hydrological investigation of intense rainfall and sediment yield in Thriasio*, Assessment of sediment generation in Thriasio, 21 pages, School of Civil Engineering – National Technical University of Athens, Athens, 2001.

Koutsoyiannis D. and Th. Xanthopoulos, *Engineering Hydrology*, Edition 3, 418 pages, National Technical University of Athens, Athens, 1999.

Koutsoyiannis D., N. Mamassis, A. Efstratiadis, N. Zarkadoulas, and Y. Markonis, *Floods in Greece*, Changes of Flood Risk in Europe, edited by Z. W. Kundzewicz, Chapter 12, 238–256, IAHS Press, Wallingford – International Association of Hydrological Sciences, 2012.

Koutsoyiannis, D., D. Kozonis, and A. Manetas, *A mathematical framework for studying rainfall intensity-duration-frequency relationships*, Journal of Hydrology, 206(1-2), 118-135, 1998.

Koutsoyiannis, D., *Design of Urban Sewer Networks*, Edition 4, 180 pages, National Technical University of Athens, Athens, 2011.

Lekkas, E., N. Voulgaris, and S. Lozios, *Flash Flood in West Attica (Mandra, Nea Peramos) November 15, 2017*; Newsletter of Environmental, Disaster and Crisis Management Strategies, Issue No 5, Athens, November 2017

Markopoulos-Sarikas G., C. Ntigkakis, P. Dimitriadis, G. Papadonikolaki, A. Efstratiadis, A. Stamou, and D. Koutsoyiannis, How probable was the flood inundation in Mandra? A preliminary urban flood inundation analysis, European Geosciences Union General Assembly 2018, Geophysical Research Abstracts, Vol. 20, Vienna, EGU2018-17527-1, European Geosciences Union, 2018.

Michailidi E., *Flood risk assessment in gauged and ungauged basins in a multidimensional context*, PhD thesis, Universita Degli Studi di Brescia, March 2018.

Michailidi E., *Investigation of flood simulation for design in ephemeral basins - Application to Sarantapotamos basin*, Diploma thesis, 140 pages, Department of Water Resources and Environmental Engineering – National Technical University of Athens, December 2013.

Montgomery, D. R., and W. E. Dietrich, *Runoff generation in a steep, soil-mantled landscape*, Water Resour. Res., 38(9), 1168, doi:10.1029/2001WR000822, 2002.

Moustakis Y., *Pseudo-continuous stochastic simulation framework for flood flows estimation*, Diploma thesis, 215 pages, Department of Water Resources and Environmental Engineering – National Technical University of Athens, July 2017.

Ntigkakis C., G. Markopoulos-Sarikas, P. Dimitriadis, T. Iliopoulou, A. Efstratiadis, A. Koukouvinos, A. D. Koussis, K. Mazi, D. Katsanos, and D. Koutsoyiannis, *Hydrological investigation of the catastrophic flood event in Mandra, Western Attica*, European Geosciences Union General Assembly 2018, Geophysical Research Abstracts, Vol. 20, Vienna, EGU2018-17591-1, European Geosciences Union, 2018.

Papaioannou, G., A. Efstratiadis, L. Vasiliades, A. Loukas, S.M. Papalexiou, A. Koukouvinos, I. Tsoukalas, and P. Kossieris, *An operational method for Floods Directive implementation in ungauged urban areas*, Hydrology, 5(2), 24, doi:10.3390/hydrology5020024, 2018.

Ponce V.M., and R. H. Hawkins, *Runoff Curve Number: has it reached maturity?*, Journal of Hydrologic Engineering, 1(1), 11–19, 1996.

Savvidou E., A. Efstratiadis, A. D. Koussis, A. Koukouvinos, and D. Skarlatos, *The curve number concept as a driver for delineating hydrological response units*, Water, 10 (2), 194, doi:10.3390/w10020194, 2018.

Soil Conservation Service (SCS), *National Engineering Handbook*, Section 4, Hydrology (NEH-4), U.S. Department of Agriculture, Washington, DC, 1972.

Soulis, K.X., and J.D. Valiantzas, *SCS-CN Parameter determination using rainfall-runoff data in heterogeneous watersheds - The two-CN system approach*, Hydrology and Earth System Sciences, 16, 1001–1015, 2012.

Velásquez, N., Hoyos, C. D., Vélez, J. I., and Zapata, E.: *Reconstructing the Salgar 2015 Flash Flood Using Radar Retrievals and a Conceptual Modeling Framework: A Basis for a Better Flood Generating Mechanisms Discrimination*, Hydrol. Earth Syst. Sci. Discuss., https://doi.org/10.5194/hess-2018-452, in review, 2018.

World Meteorological Organisation, *International Glossary of Hydrology*, No. 385, 2012

Zarkadoulas A., *Development of a hydrometeorological forecasting model for the ephemeral basin of Sarantapotamos*, Diploma thesis, 210 pages, Department of Water Resources and Environmental Engineering – National Technical University of Athens, July 2014.

11.1 Web Pages

http://floods.ypeka.gr (last visit 20/09/2018)

http://www.meteo.noa.gr (last visit 30/09/2018)

http://www.meteo.noa.gr/GR/iersd_radar_gr.htm (last visit 30/09/2018)

http://www.noa.gr (last visit 30/09/2018)

https://www.tovima.gr/2017/11/15/society/oi-ydatinoi-efialtes-tis-mandras-ksanazwntanepsan-me-nekroys-traymaties-kai-swreia-eythynwn/ (last visit 24/10/2018)

https://www.newsit.gr/ellada/etsi-pnigike-mandra-pos-egine-triti-megalyteri-katastrofi-apo-plimmyres-stin-attiki/2293548/ (last visit 24/10/2018)

http://www.geotee-anste.gr (last visit 24/10/2018)

Appendix A: Matlab code

Appendix A1: Model B-I

Main script

```
clear;
clc;

% contains ViliaRain, Qobs, UH
load('Data_UH.mat')

% number of rainfall variables
var_num = 48;
% number of Monte Carlo iterations
iter_num = 1000;

% rainfall ratio controlled by the station in Vilia
vilia = 0.2;

% Curve Number for Type I, II and III
CNII = 48; % known from past studies
CNI = 4.2*CNII / (10-0.058*CNII);
CNIII = 23*CNII / (10+0.13*CNII);

% pre-allocating the Monte Carlo arrays
sim_length = size(ViliaRain,1); % =97
UH_length = size(UH,1); % =54
Qsim1 = zeros(sim_length+UH_length-2 , iter_num);
I1 = zeros(10,iter_num);
h1 = zeros(10,iter_num);
T1 = zeros(10,iter_num);
fval1 = zeros(1,iter_num);
h01 = zeros(1,iter_num);
CN1 = zeros(1,iter_num);
S1 = zeros(1,iter_num);
a1 = zeros(1,iter_num);
AMC1 = zeros(1,iter_num);
XRain1 = zeros(var_num,iter_num);

% initial abstraction ratio of events studied in the past
A = [0.019 0.030 0.029 0.130 0.045 0.199 0.190 0.058 0.218 0.259 0.280
0.047];
% forming the Log-Normal distribution
A = log(A);
mu = mean(A);
sigma = std(A);

parfor i=1:iter_num

    % picking the random initial abstraction ratio
    flag = 1;
    while flag == 1
```

```
        a = norminv(rand(),mu,sigma);
        a = exp(a);
        if (a<0.4) && (a>0)
            flag = 0;
        end
    end

    % picking the random AMC coefficient
    flag = 1;
    while flag == 1
        AMC = norminv(rand(),0.4,0.1); % AMC coefficient
        if AMC>0
            flag = 0;
        end
    end

    % correcting the Curve Number
    if AMC<0.5
        CN = CNII-(CNII-CNI)/0.4*(0.5-AMC); %corrected CN
    else
        CN = (CNIII-CNII)/0.4*(AMC-0.5)+CNII;
    end

    % upper and lower bounds for the rainfall variables
    lb = zeros(1,var_num);
    ub = 100*ones(1,var_num);

    fun = @(XRain)wrapper_uh(XRain, ViliaRain, Qobs, a, UH, CN, vilia);
    [XRain,fval] = ga(fun, var_num, [], [], [], [], lb, ub);

    % ga returns a line vector while the code works with a column vector
    XRain = XRain(:);

    % re-calling the model_uh function using the optimized XRain, in order
    % to keep the resulting Qsim, S and h0
    [Qsim, S, h0] = model_uh(XRain, ViliaRain, Qobs, a, UH, CN, vilia);

    % probabilistic analysis:
    % I = rainfall intensity
    % h = rainfall depth
    % T = return period
    [I, h, T] = idf(XRain);


    % arrays ending in __1 contain the results of each Monte Carlo
    % iteration
    Qsim1(:,i) = Qsim;
    XRain1(:,i) = XRain;
    I1(:,i) = I;
    h1(:,i) = h;
    T1(:,i) = T;
    fval1(:,i) = fval;
    h01(:,i) = h0;
    CN1 (:,i) = CN;
    S1(:,i) = S;
```

```
    a1(:,i) = a;
    AMC1(:,i) = AMC;
end

% writing the results in Microsoft Excel spreadsheets for further analysis
fval1 = fval1';
xlswrite('results.xlsx',fval1,'Qsim','A3');
AMC1 = AMC1';
xlswrite('results.xlsx',AMC1,'Qsim','B3');
a1 = a1';
xlswrite('results.xlsx',a1,'Qsim','C3');
CN1 = CN1';
xlswrite('results.xlsx',CN1,'Qsim','D3');
h01 = h01';
xlswrite('results.xlsx',h01,'Qsim','E3');
S1 = S1';
xlswrite('results.xlsx',S1,'Qsim','F3');
Qsim1=Qsim1';
xlswrite('results.xlsx',Qsim1,'Qsim','I3');
XRain1=XRain1';
xlswrite('results.xlsx',XRain1,'XRain','J5');
T1 = T1';
xlswrite('results.xlsx',T1,'T','H7');
h1 = h1';
xlswrite('results.xlsx',h1,'h','H7');
I1 = I1';
xlswrite('results.xlsx',I1,'I','H7');
```

Wrapper function

```
function [ fval ] = wrapper_uh( XRain, ViliaRain, Qobs, a, UH, CN, vilia )
% takes as inputs the time series of the simulated rainfall at X-station,
% the observed rainfall at Vilia, the observed streamflow at Gyra Stefanis,
% the initial parameters and the unit hydrograph. Calls the model_uh, which
% simulated the streamflow at Gyra Stefanis, and calculates the value of
% the objective function f
%
% Qobs = observed streamflow at Gyra Stefanis
% XRain = simulated rainfall at X-station
% ViliaRain = observed rainfall at Vilia
% a = initial abstraction ration
% UH = parametric synthetic unit hydrograph
% CN = curve number
% vilia = rainfall ration controlled by the station in Vilia

% simulated streamflow
Qsim = model_uh(XRain, ViliaRain, Qobs, a, UH, CN, vilia);

% pre-allocating arrays
error_length = size(Qobs,1);
error1 = zeros (error_length,1);

% calibration function error1
for i=1:error_length
    error1(i,1) = (Qsim(i,1) - Qobs(i,1))^2;
```

```
end

Qsim_max = max(Qsim);

% upper and lower bounds of peak flow
UB = 200;
LB = 110;

% calibration function penalty
if Qsim_max > UB
    penalty_UB = 0.01 * (Qsim_max - UB)^2;
else
    penalty_UB = 0;
end
if Qsim_max < LB
    penalty_LB = 0.01 * (Qsim_max - LB)^2;
else
    penalty_LB = 0;
end

% calibration function error2
error2 = 10*mean(error1(37:46));

fval = mean(error1) + penalty_LB + penalty_UB + error2;
end
```

Model Function

```
function [ Qsim, S, h0 ] = model_uh(XRain, ViliaRain, Qobs, a, UH, CN, vilia)
% takes as inputs the time series of the simulated rainfall at X-station,
% the observed rainfall at Vilia, the observed streamflow at Gyra Stefanis,
% the initial parameters and the unit hydrograph and simulates the
% streamflow at Gyra Stefanis. The outputs are the simulated streamflow, the
% maximum potential retention and the initial abstraction ratio
%
% Qobs = observed streamflow at Gyra Stefanis
% XRain = simulated rainfall at X-station
% ViliaRain = observed rainfall at Vilia
% a = initial abstraction ration
% UH = parametric synthetic unit hydrograph
% CN = curve number
% vilia = rainfall ration controlled by the station in Vilia

sim_length = size(ViliaRain,1); % =97
UH_length = size(UH,1); % =54

% pre-allocating arrays
BasinRain = zeros (sim_length,1);
H = zeros (sim_length,1);
He = zeros (sim_length,1);
he = zeros (sim_length,1);
A = zeros(sim_length+UH_length-2 , sim_length);

% ga uses a line vector while the code works with a column vector
```

```
XRain = XRain(:);

% BasinRain = total rainfall time series
for i = 1:sim_length
    if i <= 19 % 14/11/2017 0:00 until 14/11/2017 9:00
        BasinRain(i,1) = vilia * ViliaRain(i,1);
    elseif i > 67 % 15/11/2017 9:30 and later
        BasinRain(i,1) = vilia * ViliaRain(i,1);
    else
        BasinRain(i,1) = vilia * ViliaRain(i,1) + (1-vilia) * XRain(i-19,1);
    end
end

% maximum potential retention for 20% initial abstraction ratio
S20 = 254*(100/CN-1);
% total rainfall depth
h_tot = sum(BasinRain,1);
% total effective rainfall depth
h_en = (h_tot-0.2*S20)^2 / (h_tot+0.8*S20);
% maximum potential retention (Sa)
S = (2*a*h_tot+(1-a)*h_en-sqrt(h_en*(h_en*(1-a)^2+4*a*h_tot))) / (2*a^2);
% initial abstraction
h0 = a*S;

for i = 1:sim_length
    % total accumulated rainfall
    if i == 1
        H(i,1) = BasinRain(i,1);
    else
        H(i,1) = BasinRain(i,1)+H(i-1,1);
    end

    % effective accumulated rainfall
    if H(i,1) > h0
        He(i,1) = (H(i,1)-h0)^2 / (H(i,1)-h0+S);
    else
        He(i,1) = 0;
    end

    % effective rainfall
    if i == 1
        he(i,1) = 0;
    else
        he(i,1) = He(i,1) - He(i-1,1);
    end

    % Array A calculates the simulated streamflow using the parametric
    % synthetic hydrograph. The sum of each row of array A is the simulated
    % streamflow at each time step
    if i==1
        A(1,1)=0;
    else
        for j=2:UH_length
            A(i+j-2,i) = he(i)/10*UH(j);
        end
    end
```

```
end
Qsim = sum(A,2);
end
```

Appendix A2: Model B-II

Main script

```
clear;
clc;

% contains ViliaRain, Qobs, UH
load('Data_UH.mat')

%additional calibration points
Qobs(71)=120;
Qobs(75)=80;

% number of rainfall variables
var_num = 50;
% number of Monte Carlo iterations
iter_num = 1000;

% rainfall ratio controlled by the station in Vilia
vilia = 0.2;

% Curve Number for Type I, II and III
CNII = 48; % known from past studies
CNI = 4.2*CNII / (10-0.058*CNII);
CNIII = 23*CNII / (10+0.13*CNII);

% pre-allocating the Monte Carlo arrays
sim_length = size(ViliaRain,1); % =97
UH_length = size(UH,1); % =54
Qsim1 = zeros(sim_length+UH_length-2 , iter_num);
I1 = zeros(10,iter_num);
h1 = zeros(10,iter_num);
T1 = zeros(10,iter_num);
fval1 = zeros(1,iter_num);
h01 = zeros(1,iter_num);
CN1 = zeros(1,iter_num);
S1 = zeros(1,iter_num);
a1 = zeros(1,iter_num);
AMC1 = zeros(1,iter_num);
XRain1 = zeros(var_num,iter_num);

% initial abstraction ratio of events studied in the past
A = [0.019 0.030 0.029 0.130 0.045 0.199 0.190 0.058 0.218 0.259 0.280
0.047];
% forming the Log-Normal distribution
A = log(A);
mu = mean(A);
sigma = std(A);
```

```
parfor i=1:iter_num

    % picking the random initial abstraction ratio
    flag = 1;
    while flag == 1
        a = norminv(rand(),mu,sigma);
        a = exp(a);
        if (a<0.4) && (a>0)
            flag = 0;
        end
    end

    % picking the random AMC coefficient
    flag = 1;
    while flag == 1
        AMC = norminv(rand(),0.4,0.1); %AMC coefficient
        if AMC>0
            flag = 0;
        end
    end

    % correcting the Curve Number
    if AMC<0.5
        CN = CNII-(CNII-CNI)/0.4*(0.5-AMC); %corrected CN
    else
        CN = (CNIII-CNII)/0.4*(AMC-0.5)+CNII;
    end

    % upper and lower bounds for the rainfall variables
    lb = zeros(1,var_num);
    ub = 100*ones(1,var_num);

    fun = @(XRain)wrapper_uh(XRain, ViliaRain, Qobs, a, UH, CN, vilia);
    [XRain,fval] = ga(fun, var_num, [], [], [], [], lb, ub);

    % ga returns a line vector while the code works with a column vector
    XRain = XRain(:);

    % re-calling the model_uh function using the optimized XRain, in order
    % to keep the resulting Qsim, S and h0
    [Qsim, S, h0] = model_uh(XRain, ViliaRain, Qobs, a, UH, CN, vilia);

    % probabilistic analysis:
    % I = rainfall intensity
    % h = rainfall depth
    % T = return period
    [I, h, T] = idf(XRain);

    % arrays ending in __1 contain the results of each Monte Carlo
    % iteration
    Qsim1(:,i) = Qsim;
    XRain1(:,i) = XRain;
    I1(:,i) = I;
    h1(:,i) = h;
    T1(:,i) = T;
```

```
    fval1(:,i) = fval;
    h01(:,i) = h0;
    CN1 (:,i) = CN;
    S1(:,i) = S;
    a1(:,i) = a;
    AMC1(:,i) = AMC;
end

% writing the results in Microsoft Excel spreadsheets for further analysis
fval1 = fval1';
xlswrite('results.xlsx',fval1,'Qsim','A3');
AMC1 = AMC1';
xlswrite('results.xlsx',AMC1,'Qsim','B3');
a1 = a1';
xlswrite('results.xlsx',a1,'Qsim','C3');
CN1 = CN1';
xlswrite('results.xlsx',CN1,'Qsim','D3');
h01 = h01';
xlswrite('results.xlsx',h01,'Qsim','E3');
S1 = S1';
xlswrite('results.xlsx',S1,'Qsim','F3');
Qsim1=Qsim1';
xlswrite('results.xlsx',Qsim1,'Qsim','I3');
XRain1=XRain1';
xlswrite('results.xlsx',XRain1,'XRain','J5');
T1 = T1';
xlswrite('results.xlsx',T1,'T','H7');
h1 = h1';
xlswrite('results.xlsx',h1,'h','H7');
I1 = I1';
xlswrite('results.xlsx',I1,'I','H7');
```

Wrapper function

```
function [ fval ] = wrapper_uh( XRain, ViliaRain, Qobs, a, UH, CN, vilia)
% takes as inputs the time series of the simulated rainfall at X-station,
% the observed rainfall at Vilia, the observed streamflow at Gyra Stefanis,
% the initial parameters and the unit hydrograph. Calls the model_uh, which
% simulated the streamflow at Gyra Stefanis, and calculates the value of
% the objective function f
%
% Qobs = observed streamflow at Gyra Stefanis
% XRain = simulated rainfall at X-station
% ViliaRain = observed rainfall at Vilia
% a = initial abstraction ration
% UH = parametric synthetic unit hydrograph
% CN = curve number
% vilia = rainfall ration controlled by the station in Vilia

% simulated streamflow
Qsim = model_uh(XRain, ViliaRain, Qobs, a, UH, CN, vilia);

% pre-allocating arrays
error_length = size(Qobs,1);
error1 = zeros (error_length,1);
```

```
% calibration function error1
for i=1:error_length
    error1(i,1) = (Qsim(i,1) - Qobs(i,1))^2;
end
for i=68:70
    error1(i,1) = 0;
end
for i=72:74
    error1(i,1) = 0;
end

Qsim_max = max(Qsim);

% upper and lower bounds of peak flow
UB = 200;
LB = 110;

% calibration function penalty
if Qsim_max > UB
    penalty_UB = 0.01 * (Qsim_max - UB)^2;
else
    penalty_UB = 0;
end

if Qsim_max < LB
    penalty_LB = 0.01 * (Qsim_max - LB)^2;
else
    penalty_LB = 0;
end

% calibration function error2
error2 = 10*mean(error1(37:46));

fval = mean(error1) + penalty_LB + penalty_UB + error2;
end
```

Model Function

```
function [ Qsim, S, h0 ] = model_uh(XRain, ViliaRain, Qobs, a, UH, CN, vilia)
% takes as inputs the time series of the simulated rainfall at X-station,
% the observed rainfall at Vilia, the observed streamflow at Gyra Stefanis,
% the initial parameters and the unit hydrograph and simulates the
% streamflow at Gyra Stefanis. The outputs are the simulated streamflow, the
% maximum potential retention and the initial abstraction ratio
%
% Qobs = observed streamflow at Gyra Stefanis
% XRain = simulated rainfall at X-station
% ViliaRain = observed rainfall at Vilia
% a = initial abstraction ration
% UH = parametric synthetic unit hydrograph
% CN = curve number
% vilia = rainfall ration controlled by the station in Vilia
```

```
sim_length = size(ViliaRain,1); % =97
UH_length = size(UH,1); % =54

% pre-allocating arrays
BasinRain = zeros (sim_length,1);
H = zeros (sim_length,1);
He = zeros (sim_length,1);
he = zeros (sim_length,1);
A = zeros(sim_length+UH_length-2 , sim_length);

% ga uses a line vector while the code works with a column vector
XRain = XRain(:);

% BasinRain = total rainfall time series
for i = 1:sim_length
    if i <= 19 % 14/11/2017 0:00 until 14/11/2017 09:00
        BasinRain(i,1) = vilia * ViliaRain(i,1);
    elseif i > 69 % 15/11/2017 10:30 and later
        BasinRain(i,1) = vilia * ViliaRain(i,1);
    else
        BasinRain(i,1) = vilia * ViliaRain(i,1) + (1-vilia) * XRain(i-19,1);
    end
end

% maximum potential retention for 20% initial abstraction ratio
S20 = 254*(100/CN-1);
% total rainfall depth
h_tot = sum(BasinRain,1);
% total effective rainfall depth
h_en = (h_tot-0.2*S20)^2 / (h_tot+0.8*S20);
% maximum potential retention (Sa)
S = (2*a*h_tot+(1-a)*h_en-sqrt(h_en*(h_en*(1-a)^2+4*a*h_tot))) / (2*a^2); %
Sa
% initial abstraction
h0 = a*S;

for i = 1:sim_length
    % total accumulated rainfall
    if i == 1
        H(i,1) = BasinRain(i,1);
    else
        H(i,1) = BasinRain(i,1)+H(i-1,1);
    end

    % effective accumulated rainfall
    if H(i,1) > h0
        He(i,1) = (H(i,1)-h0)^2 / (H(i,1)-h0+S);
    else
        He(i,1) = 0;
    end

    % effective rainfall
    if i == 1
        he(i,1) = 0;
    else
```

```
        he(i,1) = He(i,1) - He(i-1,1);
    end

    % Array A calculates the simulated streamflow using the parametric
    % synthetic hydrograph. The sum of each row of array A is the simulated
    % streamflow at each time step
    if i==1
        A(1,1)=0;
    else
        for j=2:UH_length
            A(i+j-2,i) = he(i)/10*UH(j);
        end
    end
end
Qsim = sum(A,2);
end
```

Appendix A3: Probabilistic analysis

```
function [ I, h, T ] = idf( Rain )
% Performs the probabilistic analysis. Takes the rainfall depth as input
% and returns the simulated rainfall intensity, rainfall depth and
% estimated return period as outputs for various time scales
%
% I = rainfall intensity
% h = rainfall depth
% T = return period

% idf curve parameters
k = 0.125;
l = 213.4;
psi = 0.641;
theta = 0.124;
ete = 0.622;

%vertical index
v_index = zeros(size(Rain,1),1);
j=0.5;
for i=1:size(Rain,1)
    v_index(i,1) = j;
    j = j+0.5;
end

% time scale (duration)
d = [0.5 1 2 3 4 5 6 12 18 24];

A = zeros(size(Rain,1),size(d,2));
A(:,1)=Rain;

for i=1:size(Rain,1)
    for j=2:size(d,2)
        if v_index(i) == d(j)
            for w=i:size(Rain,1)
                a = w-v_index(i)/0.5+1;
                A(w,j) = sum(A(a:w,1));
```

```
            end
        end
    end
end

h = max(A,[],1);

for j=1:size(d,2)
    I(j) = h(j)/d(j);
    T(j) = (I(j)*(1+d(j)/theta)^(ete)/l+psi)^(1/k);
end

I = I(:);
h = h(:);
T = T(:);
End
```